


**ADDIS ABABA UNIVERSITY**  
**SCHOOL OF GRADUATE STUDIES**  
**FACULTY OF SCIENCE**  
**DEPARTMENT OF GEOLOGY AND GEOPHYSICS**

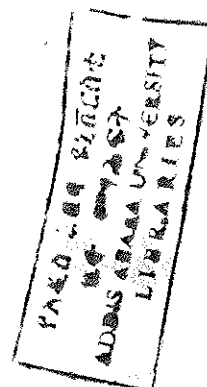
**GEOPHYSICAL STUDIES**  
**IN THE ALUTO GEOTHERMAL AREA**

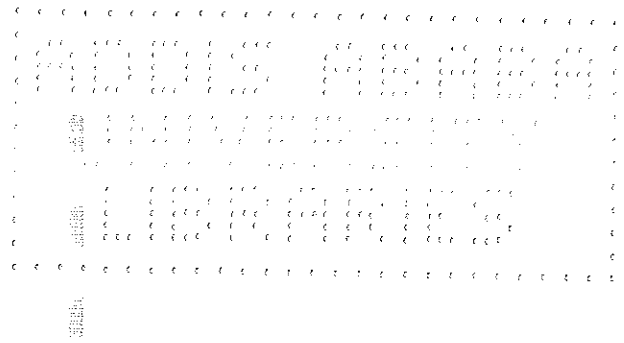
By

 Tibebu Ayele

Addis Ababa

June 2001





Expect the Lord; do manfully: and let thy heart

take courage; and wait thou for the LORD."

Psalm 26:14

**LET THIS THESIS BE DEVOTED TO**

**MY BELOVED PARENTS:**

**ATO AYELE HAILEMARIAM**

**AND**

**W/O TAFESECH ESHETE.**

## ABSTRACT

This geophysical investigation comprises gravity and electrical resistivity methods that add new information to the geology and tectonic setting of the study area. The results show major structures, major lithologic layers, intrusive bodies and thermally affected zones from the mantle-crust boundary to the surface.

The radially averaged power spectrum result of the Bouguer gravity marks the crust-mantle boundary at an average depth of 27 km. The crust above this contact is classified in to three major gravi-stratigraphic units, each unit consisting of a statistical ensemble of gravity anomaly sources generating comparable gravity field intensities. Geologically, the first deep-seated gravi-stratigraphic unit of relatively high-density is about 15 to 17 km thickness and is interpreted as the Basement Complex (?) It is expected to be highly perforated, partially melted and assimilated with magmatic and basaltic intrusions. On top of this Precambrian Basement a 5 to 7km thick Tertiary basaltic sequence is found and this is overlaid by recent siliceous volcanic products and recent rift sediments. The regional residual maps show the most tectonically active spreading zones at a depth greater than 10 km. The band pass filter applied to the Bouguer map shows intrusions that make a gravity contrast of 18 to 20 mgal with the host rock. These intrusions are situated under Shala caldera and under Aluto volcanic complex. They are interpreted as magmatic intrusions or magma chambers. The tops of these magmatic intrusions are below a depth of 7 km. The major intrusion beneath Aluto is bifurcates at this depth and show twin positive gravity anomalies at SSW of Adami-Tulu town

and at north of lake Langano bay. Major fractures and faulted zones (?) at about 2 to 3 km depth are mapped. The presence of these structures is crucial if at all there is ground water flow and hydrothermal fluid circulation at this depth. The mapped intrusions are considered to be the geothermal heat sources for the study area.

In the electrical resistivity interpretation, the apparent resistivity maps, the psuedosections and the geoelectric sections could delineate thermally affected regions, hydrothermally-altered zones and structurally weak zones. The Aluto volcanic rocks up to a depth 200 m show high resistivity values reaching to 3000 Ohmmeter. A very conductive region shows itself below this resistivity zone. The VES interpretations confirm the existence of a fractured and very conductive zone at the location of La-3 and La-6 geothermal wells. This zone is considered as the major up flow zone (T/Mariam, 1996; ELC, 1986). The apparent resistivity maps also show the increase in the conductivity of the subsurface with depth and the relative lateral resistivity distribution of the subsurface.

Based on the joint analysis of the resistivity and the gravi-stratigraphic units at an estimated depth of 0.5 to 2.5 km about six geothermal wells are anticipated. Besides, additional geophysical methods are proposed to further reinforce the anticipated wells and further confirm the outcome of this study.

---

<sup>1</sup> Gravi-stratigraphic layer is coined here to mean various layers of the Earth's crust with respect to their density contrast.

## ACKNOWLEDGMENTS

I honor **Lord** for what **He** did to me.

Principally, I would like to thank and greatly acknowledge the **Ethiopian Institute of Geological Survey** and the Geophysics Department Head (EIGS) **Ato Berihanu Bekele** for the authorization I obtained to acquire the appropriate gravity and electrical resistivity data for my study, allow me to refer to proper material and consent me to exercise software and computers.

My sincere gratitude and acknowledgments goes to: **Ato Befekadu Oluma**, my co-advisor, for the abundant material, moral and the apt supervision and for his friendly approach; **Dr. Tigistu Haile**, who was dispensed to me to verify the final version of my thesis, for the critical commentary and remarks he made on my thesis (his invariable encouragements, material and moral support has help out me incredibly in the advance of my thesis); **Dr. Tilahun Mammo** and **Dr. Laikemariam Asfaw** for the valuable material borrowed me and for the fee discussion we made on the results of my study; **Dr. Bekele Abebe**, the department head of Geology and Geophysics (AAU) as well as my co-advisor, for reading the geological part of my thesis.

It is difficult to envisage how achievable it could be to turn out this study without the free software and computer access I got from the **Aquatech PLC** and the **Nazareth school**. I have

special recognition to these organizations and to the directress of Nazareth school, **Miss Maria Goretti**, for her even encouragements and support she offered me. I am very much grateful to all the Geophysists in the **EIGS** specially, for my dear friends **Ato Beniyam Wondirad** and **Ato Senay Mekuria** for their readiness to assist me in the fabrication of my maps diagrams and train me to use application software.

I consider myself fortunate to find unusually cooperative, affectionate and competent Geophysist such as **Ato WoldeGeorgis Asfaha** and **Ato Ayele Teklu**. More than anyone, they have shared me their exclusive materials, their tremendous knowledge and skill in the data processing and interpretation procedures. I would like to offer my earnest love and gratitude to them and to professionals such as, **Dr. Meseret TekleMariam**, **Dr. Tamiru Alemayehu** and **Dr. Tesfaye Korme**, who gave me valuable and important software and resources. I can't find unique vocabulary to express my gratitude to **Dr. Tenalem Ayalew** for his tender assistance and openhandedness to borrow me incredibly vital resources from which I benefited a lot.

My acknowledgment goes to my brothers **Ato Dressie Dubale**, **Ato Getachew Abebe**, my mother **W/O Yeshareg Assfaw**, my dear spouse **W/O Aster Dubale** and my sponsor **Ato Abey Taffese** for the monetary and ethical support they granted me. I would like to bid my profound and loving credit for all my family members and my compassionate friends such as **Ato Solomon Belihue** and **Ato Kifle Telga** for the steady encouragement and comfort they bestowed me during the tough trail I passed to complete this thesis.

## TABLE OF CONTENTS

	page
<u>ABSTRACT</u>	EV
<u>ACKNOWLEDGMENTS</u>	VI
<u>TABLE OF CONTENTS</u>	VIII
<u>FIGURES AND TABLES</u>	X
CHAPTER I .....	1
GENERAL INTRODUCTION.....	1
1.1 RELEVANCE OF THE STUDY.....	1
1.2 LOCATION OF THE STUDY AREA.....	1
1.3 OBJECTIVES OF THE STUDY.....	3
1.4 GENERAL OVERVIEW OF THE STUDY.....	3
1.5 GEOLOGY OF THE STUDY AREA.....	4
1.6 OTHER RELATED STUDIES.....	9
CHAPTER II.....	11
GEOPHYSICAL METHODS .....	11
2.1 THE GRAVITY METHOD.....	11
2.1.1 Fundamental Principles .....	11
2.1.2 Theoretical Gravity of the Earth.....	12
2.1.3 The Gravitational Potential and the Geoid .....	23
2.1.4 Gravity Corrections .....	30
2.1.5 Gravity Anomalies.....	34
2.1.6 Determination of Density .....	35
2.2. THE RESISTIVITY METHOD .....	36
2.2.2. Fundamental Principles .....	37
2.2.2. General Equation for the Electrical Potential .....	39
2.2.3. A Point Electrode at the Surface of a Layered Ground .....	45
2.2.4. Current Distribution in a Horizontally Stratified Earth .....	49
2.2.5 The Effects of Temperature and Porosity on Resistivity .....	51

CHAPTER III.....	52
DATA ACQUISITION, PROCESSING AND PRESENTATION .....	52
3.1 THE GRAVITY METHOD .....	52
3.1.1. Field Procedures and Data Acquisition .....	52
3.1.2 Gravity Data Processing and Presentation.....	53
3.1.3 Homogenization and Anomaly Conversion of the gravity data .....	62
3.2 THE RESISTIVITY METHOD .....	65
3.2.1 Field Procedures and Data Acquisition .....	65
3.2.2 Resistivity Data Processing and Presentation.....	68
3.3. GEOPHYSICAL DATA INVERSION AND THE PROBLEM OF EQUIVALENCY .....	69
3.4 EVALUATION OF ERRORS.....	70
CHAPTER IV.....	74
RESULT AND INTERPRETATIONS.....	74
4.1 RESULTS AND INTERPRETATION OF GRAVITY DATA .....	74
4.1.1 Qualitative Interpretations of the Gravity anomaly maps.....	74
4.1.2 Quantitative Interpretation of the Gravity Survey .....	88
4.2. RESULTS AND INTERPRETATION OF RESISTIVITY SOUNDING .....	96
4.2.1 Qualitative Interpretation of the Resistivity Data .....	96
4.2.2 Quantitative Interpretation of the Resistivity Data .....	101
4.3 COMBINED INTERPRETATION AND ZONAL CLASSIFICATION .....	108
CHAPTER V .....	111
DISCUSSION, SUMMERY AND RECOMMENDATIONS .....	111
5.1 SUMMERY OF RESULTS.....	111
5.2 THE ORIGINALITY OF THE STUDY AND NEW RESULTS.....	112
5.3 LIMITATIONS OF THE SURVEY.....	112
5.3 RECOMMENDATION.....	113
5.3.1 Recommendation to Further Strengthen the Results of this Study .....	113
5.3.2 Recommendation to test wells.....	114
REFERENCES .....	116
DECLARATION .....	125

## FIGURES AND TABLES

	FIGURES	Page
Figure 1.1	Location Map Of Aluto And Its Environs	2
Figure 1.2	Geological map of Aluto	8
Figure 2.1	Geometry for calculating the contribution of rotational distortion to the gravitational acceleration	15
Figure 2.2	Electric field lines and equipotential surfaces around a single electrode at the surface around a single electrode at the surface of a uniform space	42
Figure 2.3	Two current and two potential electrodes on the surface of homogenous isotropic ground	43
Figure 2.4	The Schlumberger array	44
Figure 2.5	Euipotential surfaces between a source and a sink of current	50
Figure 3.1	Gravity data location	56
Figure 3.2	Data and profile location for gravity data of Aluto	57
Figure 3.3	Data and profile location for resistivity data of Aluto	69
Figure 3.4	Gravity profiles to check the selected Bouguer density	74
Figure 3.5	Wave number decomposition of the Bouguer anomaly	75
Figure 4.1	Complete Bouguer anomaly map of Aluto and its environs.	77
Figure 4.2	Radially averaged power spectrum of the Bouguer gravity anomaly for Aluto and its environs	77
Figure 4.3	Residual Bouguer anomaly map of Aluto and its environs found by applying a high pass filter with cutoff wave number of 0.0225cycl/km	80
Figure 4.4	Region gravity anomaly map of Aluto and its environs after a low pass filter with cutoff wave number of 0.015cycl/km is applied	80
Figure 4.5	Regional gravity anomaly map of Aluto and its environs after a	80

	lowpass filter with cutoff wavenumber of 0.0225cycl/km is applied	
Figure 4.6	The deepest gravi-stratigraphic layer found after applying a band pass filter with cutoff wave numbers of 0.008cycl/km and 0.0225cycl/km	80
Figure 4.7	gravi-stratigraphic layer found after applying a band pass filter with cutoff wave numbers 0.0225cycl/km and 0.128cycl/km	80
Figure 4.8	Free air anomaly map of Aluto superposed on the elevation contour	83
Figure 4.9	Complete Bouguer anomaly map of Aluto	84
Figure 4.10	Radially averaged power spectrum of Aluto for C.B.A	85
Figure 4.11	Regional gravity anomaly map of Aluto geothermal are after a second degree polynomial surface trend is removed from the C.B.A map	87
Figure 4.12	Regional gravity anomaly map of Aluto geothermal area after a low pass filter with cutoff wave number of 0.0325cycl/km is applied	87
Figure 4.13	Regional gravity anomaly map of Aluto after a low pass filter with cutoff wave number of 0.08cycl/km is applied	87
Figure 4.14	Regional gravity anomaly map of Aluto geothermal area after a low pass filter with cutoff wave number of 0.09cycl/km is applied	87
Figure 4.15	The deepest gravi-stratigraphic layer filtered out by a band pass filter with boundary cutoff wave numbers 0.0225cycl/km and 0.0325cycl/km	89
Figure 4.16	A gravi-stratigraphic layer found by applying a band pass filter with boundary cut of wave numbers 0.0325cycl/km and 0.168cycl/km	89
Figure 4.17	The first vertical derivative map of the Bouguer anomaly of Aluto	89
Figure 4.18	The second vertical derivative map of the Bouguer anomaly of Aluto	89
Figure 4.19	A gravity stratigraphic layer filtered out by using a band pass filter with boundary cutoff wave number of 0.168cycl/km and 0.0463cycl/km	89
Figure 4.20	Gravity model along profile B-B'	94

Figure 4.21	Gravity model along profile C-C'	95
Figure 4.22	Gravity model along profile E-E'	96
Figure 4.23	Gravity model along profile F-F	97
Figure 4.24	Apparent resistivity map of Aluto geothermal area $AB / 2 = 10 \text{ m}$	100
Figure 4.25	Apparent resistivity map of Aluto geothermal area $AB/2 = 100\text{m}$	100
Figure 4.26	Apparent resistivity map of Aluto geothermal area $AB/2 = 1000\text{m}$	102
Figure 4.27	Apparent resistivity map of Aluto geothermal area $AB/2 = 2150\text{m}$	102
Figure 4.28a	Apparent resistivity profile plots along A-A'	104
Figure 4.28b	Apparent resistivity psuedosection of profile A-A'	104
Figure 4.28c	Geoelectric section along profile A-A'	104
Figure 4.29a	Apparent resistivity profile plots along B-B'	105
Figure 4.29b	Apparent resistivity psuedosection of profile B-B'	105
Figure 4.29c	Geoelectric section along profile B-B'	105
Figure 4.30a	Apparent resistivity profile plots along C-C'	108
Figure 4.30b	Apparent resistivity psuedosection of profile C-C'	108
Figure 4.30c	Geoelectric section along profile C-C'	108
Figure 4.31a	Apparent resistivity profile plots along D-D'	109
Figure 4.31b	Apparent resistivity psuedosection of profile D-D'	109
Figure 4.31c	Geoelectric section along profile D-D'	109
Figure 4.32	Zonal classification of gravity and resistivity anomaly	112
Figure 5.1	Site for future geothermal wells	117

	<b>TABLES</b>	<b>page</b>
Table 1.1	Summery of the survey	3
Table 4.1	Summery of results from the radially averaged power spectrum plots	90

## **CHAPTER I**

### **GENERAL INTRODUCTION**

#### **1.1 RELEVANCE OF THE STUDY**

As fossil fuels are getting scarce, the hunt for new sources of energy turns out to be indispensable. For countries like Ethiopia utilizing the naturally accessible energies such as geothermal energy can put in a lot for countrywide development. The Ethiopian Rift is branded for this sort of energy. However, almost nothing is consumed of this great potential. For an improved extraction of this energy, the information from every achievable scientific source regarding the location and extent of the heat source must be scrutinized together with the structural, lithological and hydrological conditions. Thus, this geophysical study is intended to offer useful information on the subsurface conditions that attribute to the geothermal energy of the study area. It also furnishes initials for deep and obscured structural settings that are associated with plate tectonics.

#### **1.2 LOCATION OF THE STUDY AREA**

The study area, Aluto, is sited in the central part of the Main Ethiopian Rift (Fig 1.1). It is about 200 km south of Addis Ababa close to the eastern margin of the MER and is found inside the Wonji Fault Belt. It rises about 700m from the surrounding rift floor and has a maximum elevation of 2328 m above sea level. Its exact location is at about 7° 45' N, 38° 48' E. It covers an area of about 110 km<sup>2</sup> between lake Langano and lake Ziway and is 6 km by 9 km elongated in the NW and SE direction.



### 1.3 OBJECTIVES OF THE STUDY

The main objectives of this M. Sc. research are:

- A. To identify major lithologic units and their thickness;
- B. To map structures and intrusive bodies at various depths;
- C. To map conductive zones at various depths;
- D. To determine the depth to the magma chamber in the study area;
- E. To prepare 2-D geoelectric and gravity model for the study area;

### 1.4 GENERAL OVERVIEW OF THE STUDY

The following table gives a general view on the survey.

**Table 1.1.** Summary of the survey

Data and type of survey	Area coverage (Approximately)	Instrument used	Number of data points	Remark
Land gravimetric survey	10,000km <sup>2</sup>	Model G 303 LaCosta -Romberg	992	Random data* Minimum sampling interval=500m
Resistivity Sounding	250km <sup>2</sup>	IPR-10	84 (VES)	Line data** Minimum sampling interval=500m

\*Data that is not taken on a square grid.

\*\*Data that is taken on a line or along a profile

The thesis is organized in five chapters. The first chapter is a general introduction dealing with the purpose of the study, the location and geological setting of the study area. The second chapter is about the theoretical background of the geophysical methods employed. The third chapter deals with data acquisition, processing and interpretation. The fourth chapter is devoted to results found in the study. The fifth chapter addresses the conclusions, discussion and recommendations. Lastly, catalog of reference materials are listed.

## **1.5 GEOLOGY OF THE STUDY AREA**

### **Geology of the Main Ethiopian Rift (MER)**

The deepest lithologic unit of the crust in the central part of MER is little known. However, the general succession of the strata in the horn of Africa consists of a Precambrian sequence mainly of metamorphic, Mesozoic sedimentary sequence, Tertiary flood basalts and silicic lava flows with pyroclastic sediments interstratified overlain by Quaternary sediments and alkali silicic lava flows (Mohr, 1971). These sequences and one of the aged rock, the Crystalline Basement/Basement Complex/ Precambrian rock/ outcrops in some parts of the Rift margin and Horsts such as: the Gurage Mountain (Woldegebriel et al., 1999) and southern part of MER (Yemane et al., 1999).

A number of geologists, such as: Kazmin & Berhe, (1978), Woldegebriel et al., (1992), Boccaletti et al., (1995), Abebe et al., (1998), Morley, (1999) etc. have studied the evolution and development of the Ethiopian Rift and have arrived at two main hypotheses. The evolution of the Ethiopian Rift has been proposed as: pure Extension (Mohr, 1983; Ebinger

et al., 1993) with dextral component of displacements (Chorowicz et al., 1994), and left lateral component of displacement along the rift axis during Quaternary (Boccaletti et al., 1992, 1994, 1998; Abebe et al., 1998)

Rifting in this part of the world started during the early Tertiary jointly with regional crustal uplift forming the Afro-Arabian dome until the end of the Eocen. Mantle plums must have caused this doming (Morley, 1999). The Bouguer anomaly map of Ethiopia (after Purcell, 1981) suggests that this mantle pluming caused abnormally low-density mantle material that contributes to the regionally negative Bouguer anomaly all over Ethiopia. According to Morley, (1999) the generation of basaltic melts is also caused by mantle heating by rising mantle plumes.

“ ... the opening of the Ethiopian Rift is related to the uprising of at least two mantle plums, presently located beneath the central Gregory Rift in Kenya and beneath the Afar depression. The older Kenyan plum gave rise to the Eocene-Oligocene magmatism of Southern Ethiopia (Yemane et al., 1999), which successively migrated southward as a consequence of northward movements of the African plate. The Afar plume is believed to be younger and responsible for the bulk of the magmatism in the central Ethiopia and Afar region.” Morley, (1999). From Oligocene to the earliest Miocene following the uplift of the Afro-Arabian dome, basaltic magma eruptions occurred through fissures in tensional zones (Mohr, 1962a, 1971b). The rift faulting following the capacious trap volcanics split the crust into three distinct segments: the Arabian Plate, the African Plate and the Somalian Plate (Mohr, 1971b) The central part of this rift system is called the MER and it was during the last uplift that it was formed to its present form (Mohr, 1971b). Mohr, (1967) and Baker et al., (1972)

believe that subsequent volcanic activity of the rift has been largely confined to the active Wonji Fault Belt (WFB) running parallel to the rift axes. The WFB is described (Gouin, 1979; Mohr, 1983; Alula et al., 1992) as a zone of both fissural and central volcanism from the lower Pleistocene to the present. This volcano-tectonic axis (WFB) named by Mohr (1960) is 5 to 15km in width along the current axis of crustal extension (Mohr 1967; Di Paola 1972). Sediments of lacustrine origin cover some areas of the rift with varying thickness and some fluvial and colluvial deposits also found about the lakes region. These are the only non-volcanic formations (Jean, J., et al., 1997).

The MER extends in a NE / NNE to SE / SSW direction from the southern Afar Rift 9° 30' N to Konso highland 5° 15' N in southern Ethiopia forming three segments: Fantale-Nazareth, Nazareth-Awasa and Awasa-Konso (Woldegebriel 1999). It consists of three caldera related basins (Ziway-Langano- Abiyata- Shala- Awassa) connected by WFB (Woldegebriel, et al., 1990) and Bilate river drainage basins. The general stratigraphy of the MER, with chronological order from the older to the younger, can be constructed briefly as follows (after Tenalem, 1998): The Nazareth group and Dino formation undifferentiated, the Afar group, Chilalo volcanics, Balchi rhyolite, basalts and associated flows of the rift, central rift volcanic complexes (Aluto volcanics, Gadamotta rhyolite, Corbetti volcano, Bora-Bericho and Fike) and volcano-sedimentary rocks and lacustrine sediments.

### **Geology of the Aluto Volcanic Complex**

The study area Aluto (Fig 1.2) is found in the central part of the MER and is the product of recent volcanism. It is a silicic volcanic mountain, which is reported to be older than both Corbetti and Shala. Its structural and volcanic evolution is controlled by the influence of the

WFB (WoldeGebriel et al., 1992; Gianelli and Teklemariam, 1993; ELC, 1986).

The Aluto volcanic succession appears to have been erupted at frequent intervals during the late Quaternary. This fact can partly be proved by the late Pleistocene and Holocene lake deposits of the Bulbula plain containing pyroclastic and fluvial-reworked Aluto pumices (Street et al, 1979). These volcanic products consist of a complex sequence of alternating pyroclastic, pumice falls and tuff breccias with very viscous lava flows of late Pleistocene to Holocene (UN, 1973). All these products have a peralkali-rhyolitic composition. In general according to (ELC, 1986) the age of Aluto volcanic products age ranges from  $155,000 \pm 8000$  to 2000 years ( $^{14}\text{C}$  method;). Hochstein et al., (1983) suggested a minimum age of 140,000 years and Teklemariam et al., (1996) approximately 155,000 years for the Aluto-Langano geothermal system. From the well results and investigation made by Teklemariam, (1996) the oldest rock unit discovered in the area is the Tertiary ignimbrite. The Bofa basalt formation overlies the Tertiary ignimbrite. Its thickness is about 800-1000m that is assumed to be basalt from fissural eruption (Boccaletti et al., 1999). Lacustrine sediments cover the Bofa basalt. These sediments (Pleistocene-Holocene) are predominately fine grained vitric tuffs, sandstone and pumiceous rhyolitic gravels. The Awariftu ignimbrite 0.094Ma in the North of Aluto Complex is a pumiceous ash-flow deposit. This unit overlies the Pleistocene lacustrine sediments of the Lakes region. The uppermost units are different peralkali-rhyolitic obsidian flows and pumice layers.

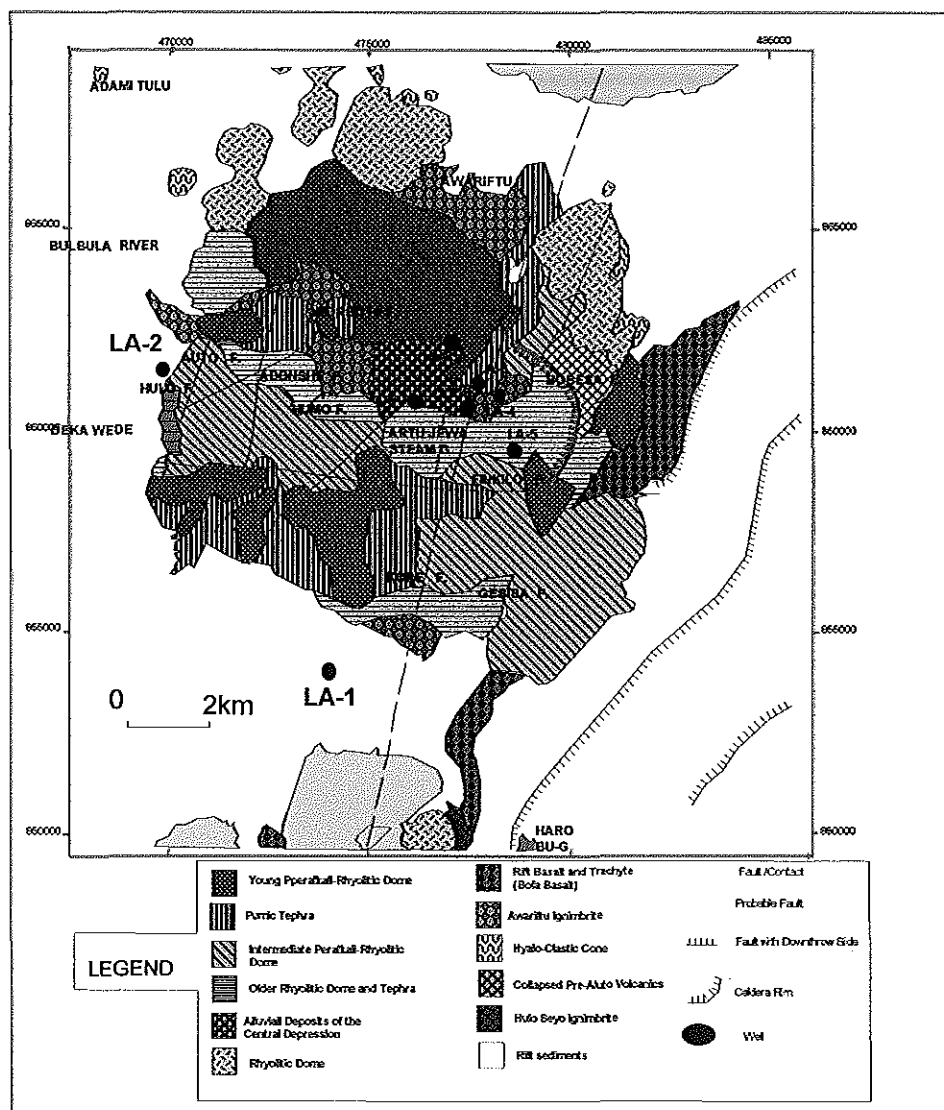


Fig. 1.2 Geological map of Aluto area.

## **1.6 OTHER RELATED STUDIES**

### **United States Development Program (UNDP, 1973)**

In the report, Aluto is considered to be one of the major geothermal prospective areas. The general hydrological, geothermal and geological conditions are described. Accordingly, the Ethiopian Rift in general, is described as a zone of regionally high heat flow with temperature gradient up to ten times the world average of 30 °C / km may exist and that heat source is believed to be shallow magma. Many of the basalts of the central and southern Afar and the Main Ethiopian Rift erupted to the surface through narrow fissures penetrating the comparatively thin crust. Most such dikes and sills are small in volume and are unlikely to maintain a hydrothermal system for long. Other anomalies are due to upward transference of heat in the rift convecting hot water. Most hot springs and fumaroles in the rift area associated with silicic volcanic centers and a deep heat source such as a cooling intrusion is proposed beneath the springs. In general, local anomalies of heat from direct volcanic associations are due to heat flow from shallow magma. These are closely related to spreading zones. The location of many hot springs and other hydrothermal manifestations are controlled by very young and commonly superficial faults and fault intersections. These systems that regionally, fault zones remain open for long periods only at points of interplay of opposite tectonic stress and moreover, cross faulting facilitates formations of shallow magma chamber.

### **EIGS(1983)**

From the report of the Ethiopian Institute of Geological Survey, the electrical resistivity and the Dipole - Dipole results could identify about three layers with the top layer being

highly resistive with resistivity values ranging up to 2000  $\Omega\cdot m$ . A second conductive layer whose resistivity reaching up to 12  $\Omega\cdot m$  is interpreted as lake sediments and pyroclastic products; while, the last resistive layer is interpreted as the response from the Tertiary ignimbrite. The study concluded that a geothermal fluid is assumed to come through the resistive basement producing low resistivity closures in the lake sediments by heating and saturating them and producing surface geothermal manifestations. Up on this, the results of the dipole-dipole survey indicated that a geothermal fluid has invaded a vast area from lake Ziway in the north to lake Shala in the south and from Adami-Tulu in the west extending to Bobesa fumaroles in the east.

#### **Electroconsult (ELC, 1986).**

In the feasibility study of the Aluto-Langano geothermal field the assumption on the fluid flow pattern and natural recharge conditions are summarized as follows.

The location of La-3 and La-6 is considered to be the up flow zone. The reservoir volume is recharged only from below, along the Wonji Fault zone (this is a zone on which one of the major faults crosses Aluto). A hot water from depth is thought to rise through this faulted zone and laterally flows outwardly to the east and west direction. This is proved by the experimental fact that the highest temperature is encountered at the site of LA-3 / La-6 with a rapid decrease in temperature east and westwards. About 10% porosity for the crystalline ignimbrite and 8 % for the Bofa basalt was assumed. The area of potential interest is taken to be centered on the WFB system La-3 / La-6 axis having a limited extent 1-2km in the E-W direction. The Bofa basalt is generally affected by convecting fluid circulating and a temperature gradient is observed in this formation. (T/Mariam, 1996)

## **CHAPTER II**

### **GEOPHYSICAL METHODS**

#### **2.1 THE GRAVITY METHOD**

In exploration geophysics, gravity method exploits the earth's gravity field disparity caused by lateral density variations in the earth's crust. If geologic movements causes in the dislocation of rocks of different densities, the resulting indiscretion in lateral density distribution will make corresponding variation in the intensity of gravity. The measured variation in the earth's gravity field is interpreted as credible subsurface mass distributions. The gravity method is also used in modeling the earth's crust, in locating areas of anomalous mantle materials (in areas of plate margins) and it is the basis for the study of the earth's shape (Telford, 1990).

For any one of the above assets of the earth to be studied a gravity survey must be executed. Gravity survey involves measurement, reduction, mapping and interpretation of gravity data (Dobrin, 1988).

##### **2.1.1 Fundamental Principles**

Newton's Law of Universal Gravitation is the foundation of this method. The law states that for any two masses  $m_1$  and  $m_2$  there is a gravitational force of attraction that is directly proportional to the product of the masses and inversely proportional to the square of the

distance between them. That is:

$$\vec{F} = -G \frac{m_1 m_2}{r^2} \hat{e}_r \quad (2.1)$$

where,  $r$  is the distance between the masses,  $G = 6.67 \times 10^{-11} \text{ m}^3/\text{kg s}^2$ ,  $F$  = force between  $m_2$  &  $m_1$  and  $\hat{e}_r$  is a unit vector whose route is the direction of the force. If  $m_1$  is the mass of the earth, then the attraction force of the earth per unit mass acting on the surface of the earth is expressed by

$$\vec{g} = \frac{GM_e}{r^2} \vec{e} \quad (2.2)$$

where,  $g$  is the gravity force per unit mass in the direction of  $\hat{e}_r$ . This (Eq. 2.2) is recognized as the gravitational acceleration of the earth, the gravity field of the earth, gravity intensity or simply gravity. Its unit is meter per second squared. In gravity survey the 'Gal' is used as a unit.  $1 \text{ Gal} = 1 \text{ cm/s}^2$  (in honor of Galileo Galilee)

### 2.1.2 Theoretical Gravity of the Earth

Assuming the earth to be a smooth ellipsoid it is possible to develop the theoretical gravity or normal gravity value of the earth. To start with, assuming the earth to be a spheroid (Heiskanen and Moritz, 1967) and that a body of mass  $m$  is moving with a velocity of ' $v$ ' on the surface of the earth ( $M$  = mass of the earth,  $R$ =radius of the earth), the possible forces acting on the body are:

1. The mass attraction force  $g_m$  that is given by

$$g_m = \frac{GM}{R^2} \quad (2.3)$$

2. The radial component of the centrifugal force per unit mass (due to the rotation of the earth with angular velocity  $\omega$  about its axis of rotation) that is given by:

$$g_\omega = \omega(\omega \times R) \quad (2.4)$$

The maximum force is at the equator and zero at the poles and it opposes the attractive force of the earth.

3. The Coriolis force per unit mass acting on  $m_2$  due to the motion of the mass with linear velocity 'V' on the earth's surface

$$C = 2 (\omega \times V) \quad (2.5)$$

If the mass is at rest on the surface of the earth then  $V = 0$  ( $C = 0$ ).

4. The tidal force per unit mass acting on  $m$  due to mass attraction with other heavenly bodies (T).

The net gravitational field or gravity is given by

$$g = g_m + g_o + C + T \quad (2.6)$$

Since, heavenly bodies constantly change their arrangements with respect to the position of the earth the number of the heavenly bodies and their magnitude of gravitational attraction vary from time to time and it is not simple to put it in a simple formula. It is not constant, but rather vary with the position of heavenly bodies that impose gravitational force on our earth.. Gravity survey shouldn't be administered during the time of significant tide; otherwise, for small magnitude of tide the effect of T on g is generally considered negligible.

However, our earth is not a perfect spheroid. At the pole it is flattened and deviates by about 14.2 km and at the equator it is bulged by about 7.1 km from the normal spheroid of constant radius of 6356.751 km. If 'a' is the equatorial radius of the earth and 'b' is the polar radius of the earth. The polar flattening  $f$  is defined as:

$$f = \frac{a - b}{a} \quad (2.7)$$

The flattening of the optimum reference ellipsoid of the earth was revised many times. The long worked supposition defined in 1930 was exactly  $f = 1/297$ . With the use of satellites and highly sensitive gravimeters, in 1980 the value was revised as  $f = 1/298.257$  (Lowrie, 1997).

## Gravitational Acceleration on Rotationally Distorted Earth

The gravitational acceleration at point P, 'b' distance away from an element of mass  $dm$  of the earth is given by.

$$dg_m = \frac{Gdm}{b^2} \quad (2.8)$$

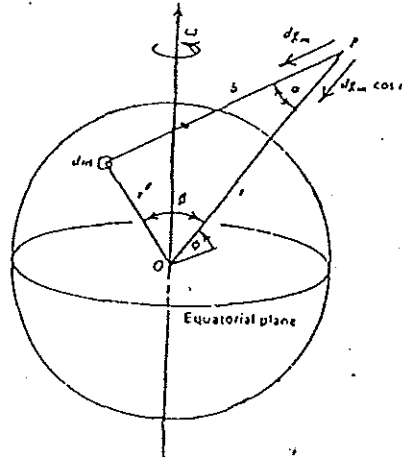


Fig.2.1. Geometry for calculating the contribution of rotational distortion to the gravitational acceleration.

The component of this gravitational acceleration along the line from P to the centre of the earth 'O' is  $g_m = \frac{G \cos \alpha dm}{b^2}$ , where  $\alpha$  is the angle between b and r on the line to the centre of the earth. The net radially inward gravitational acceleration at point P is found by integrating this expression over the entire mass distribution.

$$dg_m = G \int \left( \frac{\cos \alpha}{b^2} \right) dm \quad (2.9)$$

using cosine law,

$$\cos \alpha = \frac{b^2 + r^2 - r'^2}{2rb} \quad (2.10)$$

substituting equation (2.10) in equation (2.9) and simplifying results in:

$$g_m = \frac{G}{2r^2} \int \left( \frac{r}{b} + \frac{r^3}{b^3} \left\{ 1 - \frac{r'^2}{r^2} \right\} \right) dm \quad (2.11)$$

The three distances appearing in the integral of equation (2.11):  $r$ ,  $r'$  and  $b$  are the sides of the triangle connecting  $O$ ,  $P$  and  $dm$ . From the law of cosine's in equation (2.10)

$$b^2 = r^2 + r'^2 - 2 r r' \cos \beta \quad (2.12a)$$

by dividing both sides by  $r^2$  the equation can be rearranged as

$$\frac{r}{b} = \left( 1 - \frac{2r'}{r} \cos \beta + \frac{r'^2}{r^2} \right)^{-\frac{1}{2}} \quad (2.12b)$$

up on substitution equation (2.12b) into equation (2.11) one obtains

$$g_m = \frac{G}{2r^2} \int \left[ 1 + \frac{r'^2}{r^2} - 2 \frac{r'}{r} \cos \beta \right]^{-\frac{1}{2}} \left[ 1 + \left\{ 1 + \frac{r'^2}{r^2} - 2 \frac{r'}{r} \cos \beta \right\}^{-1} \left\{ 1 - \frac{r'^2}{r^2} \right\} \right] dm \quad (2.13)$$

An analytical evaluation of the integral in equation (2.13) is not possible. The integration is complicated because both  $r'$  and  $\beta$  vary with position of  $dm$ . However, by approximating the integrand with a power series of  $r'/r$  the integral becomes manageable.

Using power series expansion and retaining the terms up to  $(r'/r)^2$  only; for P outside mass distribution  $(r'/r) < 1$ . For Power Expansion on  $E < 1$

$$(1 + E)^{-1} = 1 - E + E^2 + \dots \quad (2.14)$$

$$g_m = \frac{G}{r^2} \int dm + 2 \frac{G}{r^2} \int r' \cos \beta dm + 3 \frac{G}{r^4} \int r'^2 \left( 1 - \frac{3}{2} \sin^2 \beta \right) dm \quad (2.15)$$

The integration in equation (2.15) can be carried out in terms of well-known physical properties of mass distribution. The first term is just the integral of  $dm$  over the entire mass distribution. The result is simply the total mass  $M$ . The second term is the integral of  $r' \cos \beta$  over the mass distribution and is a first moment of distribution which is by definition zero. If the origin of the coordinate system is the centre of mass distribution, i.e.,  $2G/r^3 \int r \cos \beta dm = 0$ ; thus equation (2.15) becomes:

$$g_m = \frac{GM}{r^2} + \frac{3G}{r^4} \int r'^2 \left[ 1 - \frac{3}{2} \sin^2 \beta \right] dm \quad (2.16)$$

Where,  $GM/r^2$  is the gravitational acceleration of a spherical mass distribution and the second term is the modification due to rotationally induced oblateness of the body. The

integral appearing in equation (2.16) can be expressed in terms of the moments of inertia of a symmetric axis to the body. Taking  $C$  to be the moment of inertia of the body about the rotational axis or  $\theta = 0^\circ$ , this moment of inertia is the integral over the entire mass distribution of  $dm$  times the square of the distance from  $dm$  to the rotational axis.

$$C = \int [X'^2 + Y'^2] dm = \int r'^2 \sin^2 \theta' [\cos^2 \phi' + \sin^2 \phi'] dm$$

$$C = \int r'^2 \sin^2 \theta' dm \quad (2.17)$$

By using co-ordinates transformation

$$r'^2 = x'^2 + y'^2 \quad (2.18a)$$

$$x' = r' \sin \theta' \cos \phi' \quad (2.18b)$$

$$y' = r' \sin \theta' \sin \phi' \quad (2.18c)$$

$$z' = r' \cos \theta' \quad (2.18d)$$

The moment of inertia about the  $x$ -axis, which is defined by  $\theta = \pi/2$  and

$\phi = \pi/2$  are:

$$A = \int [y'^2 + z'^2] dm = \int r'^2 [\sin^2 \theta' \sin^2 \phi' + \cos^2 \theta'] dm \quad (2.19)$$

The moment of inertia about y-axis defined by  $\theta = \pi/2$  and  $\phi = \pi/2$ , is

$$B = \int [x'^2 + z'^2] dm = \int r'^2 [\sin^2 \theta' \cos^2 \phi' + \cos^2 \theta'] dm \quad (2.20)$$

For a body that is axial symmetric about the z-axis or rotational axis  $A = B$ , the addition of equations (2.17), (2.19) and (2.20) together with the assumption of axial symmetry gives:

$$A + B + C = 2 \int r'^2 dm = 2A + C \quad (2.21)$$

Equation (2.21) expresses the integral of  $r'^2 dm$  appearing in equation (2.16) in terms of moment of inertia of the body. To drive an expression for the integral of  $r'^2 \sin^2 \beta dm$ , because of axial symmetry of the body there is no loss of generality in letting the line OP lies in the x-z plane. With the help of equation (2.21), the required integral can be rewritten as

$$\begin{aligned} \int r'^2 \sin^2 \beta dm &= \int r'^2 (1 - \cos^2 \beta) dm = \int r'^2 dm - \int r'^2 \cos^2 \beta dm \\ &= A + \frac{1}{2} C - \int r'^2 \cos^2 \beta dm \end{aligned} \quad (2.22)$$

The quantity  $r' \cos \beta$  is the projection of  $r'$  along OP. This quantity can be expressed as

$$r' \cos \beta = x' \cos \phi + z' \sin \phi \quad (2.23)$$

where  $\phi$  is the angle between OP and the x-y-plane.  $y'$  has no projection onto OP, since OP

is in the x-z-plane. Using Eq.(2.23) to write the integral of  $r'^2 \cos^2 \beta$  in the form

$$\int r'^2 \cos^2 \beta \, dm = \int x'^2 \cos^2 \phi \, dm + \int 2x'z' \cos \phi \sin \phi \, dm + \int z'^2 \sin^2 \phi \, dm \quad (2.24)$$

For an axial symmetric body:

$$(x'^2 + y'^2) \, dm = \frac{1}{2} C \quad (2.25)$$

The integral of  $z'^2 \, dm$  can be evaluated by using equation (2.17) & (2.21)

$$\int z'^2 \, dm = \int (x'^2 + y'^2 + z'^2) \, dm - \int (x'^2 + y'^2) \, dm$$

$$A + \frac{1}{2} C = \int (x'^2 + z'^2) \, dm + \int x'^2 \, dm = \int r'^2 \, dm$$

$$\int z'^2 \, dm = A + \frac{1}{2} C - C = A - \frac{1}{2} C \quad (2.26)$$

With mass symmetry about the equatorial plane

$$\int x' z' \, dm = \int r'^2 \cos \theta' \sin \theta' \cos \phi \, dm = 0 \quad (2.27)$$

Substitution of equation (2.25) and (2.27) into equation (2.24) yields

$$\int r'^2 \cos^2 \beta \, dm = \frac{1}{2} C \cos^2 \phi + (A - \frac{1}{2} C) \sin^2 \phi \quad (2.28)$$

Combining Eqs. (2.22) & (2.28) and using the trigonometric identity  $\sin^2 \phi + \cos^2 \phi = 1$ ,

$$\int r'^2 \sin^2 \beta \, dm = A \cos^2 \phi + C \sin^2 \phi \quad (2.29)$$

The gravitational acceleration is finally obtained by substituting Eq.(2.21) and Eq.(2.29) into equation Eq.(2.16)

$$g_m = \frac{GM}{r^2} - \frac{3G}{2r^4} (C - A) [3 \sin^2 \Phi - 1] \quad (2.30)$$

The moment of inertia about the rotational axis C is larger than the moment of inertia about an equatorial axis A, because of the rotational flattening of the body. The difference in moment of inertia is:

$$C - A = J_2 M a^2 \quad (2.31)$$

Where 'a' is equatorial radius and  $J_2$  is the polar moment of inertia. Then  $g_m$  can be expressed as:

$$g_m = \frac{GM}{r^2} - \frac{3GMa^2 J_2}{2r^4} (3 \sin^2 \Phi - 1) \quad (2.32)$$

The currently accepted values are:  $a = 6378.139 \text{ km}$ ,  $GM = 3.986005 \times 10^{14} \text{ m}^3 \text{s}^{-2}$ , and  $J_2 = 1.0827 \times 10^{-3}$ . The earth's gravitational field can be accurately determined from the tracking of artificial satellites. Although a satellite is acted upon only by the earth's

gravitational acceleration, an object on the earth's surface is also subjected to a centrifugal acceleration due to the earth's rotation

When the point 'O' is on the surface of the earth at latitude  $\phi$ , the force on a unit mass at that point 'O' to the rotation of the earth with angular velocity ' $\omega$ ' is the centrifugal acceleration  $g_\omega$ . It points radially outward along a line perpendicular to the rotation axis and passing through P and is given

$$g_\omega = \omega^2 S \quad (2.33)$$

where S is the perpendicular distance from P to the rotation axis. If r is a radial distance from P to the centre of the earth and  $\phi$  is the latitude of point P

$$S = r \cos \phi \quad (2.34)$$

$$g_\omega = \omega^2 r \cos \phi \quad (2.35)$$

The gravitational and centrifugal acceleration of a mass at the earth's surface is combined to yield the acceleration of gravity g. Since  $g_\omega$  is very much less than  $g_m$ , it is legal to add the radial component of centrifugal acceleration to  $g_m$  to obtain g. The radial component of the centrifugal acceleration points radially outwards. In agreement with the sign convention that inward-radial accelerations are positive, the radial component of the centrifugal acceleration is given as:

$$g_r' = -g_\omega \cos \phi = -\omega^2 r \cos^2 \phi \quad (2.36)$$

The acceleration of gravity  $g$  is the sum of  $g_m$  in Eq.(2.32) and  $g_r'$ , due to the centrifugal acceleration, Eq.(2.36)

$$g = g_m - g_r$$

$$g = \frac{GM}{r^2} - \frac{3GMa^2 J_2}{2r^4} (3 \sin^2 \Phi - 1) - \omega^2 r \cos^2 \Phi \quad (2.37)$$

Equation (2.37) gives the radially inward acceleration of gravity for a point located on the surface of the model earth at the latitude  $\phi$  and distance  $r$  from the centre of mass.

### 2.1.3 The Gravitational Potential and the Geoid

The gravitational energy of mass  $m$  can be regarded as the negative of the work done on 'm' by the gravitational force of attraction in bringing  $m$  from infinity to its position in the field. The gravitational potential  $V$  is the potential energy of  $m$  divided by its mass. Because the gravitational field is conservative, the potential energy per unit mass  $V$  depends only on the position of the field and not on the path through which a mass is brought to the location. To calculate  $V$  for the rotationally distorted model earth, one can imagine bringing a unit mass from infinity to a distance  $r$  from the centre of the model along a radial path. Since  $g_m$  is a conservative field, it can be derived from  $V$  as:  $g_m = \nabla V$  and  $\text{Curl } g_m = 0$  and also:

$$V = \int_r^\infty g_m dr' = - \int_\infty^r g_m dr'$$

$$V = \int_\infty^r \left( \frac{GM}{r'^2} - \left( \frac{3GMa^2 J_2}{2r'^3} \right) (3 \cos^2 \Phi - 1) \right) dr'$$

$$V = - \frac{GM}{r} + \left( \frac{3GMa^2 J_2}{2r^3} \right) (3 \cos^2 \Phi - 1) \quad (2.38)$$

In evaluating V, one assumes that the potential energy at infinite distance from the earth is zero. The gravitational potential adjacent to the earth is negative; the earth acts as a potential well. The first term in the above equation is the gravitational potential of a point mass. It is also the gravitational potential outside a spherical symmetric mass distribution. The second term is the effect on the potential of the earth model's rotationally induced oblateness. A gravitational equipotential surface is a surface on which V is a constant. The gravity potential 'V' accounts for both mass-gravitation and rotation of the model earth. This gravitational equipotential (U) expressed in polar coordinate is:

$$\begin{aligned} U(r, \Phi) &= - \int g \cdot dr' \\ &= \int_\infty^r \left[ \frac{GM}{r'^2} - \left( \frac{3GMa^2 J_2}{2r'^4} \right) (3 \sin^2 \Phi - 1) - \omega^2 r' \cos^2 \Phi \right] dr' \\ &= - \frac{GM}{r} + \left( \frac{GMa^2 J_2}{2r^3} \right) (3 \sin^2 \Phi - 1) - \frac{1}{2} \omega^2 r^2 \cos^2 \Phi \end{aligned} \quad (2.39)$$

Elevations above or below sea level are distances above or below a reference equipotential surface. The reference equipotential surface that defines sea level is called the geoid. Geoid is the physical equipotential surface of gravity.

The international reference ellipsoid is, a mathematical surface and a close approximation to the equipotential surface of gravity. It reflects the true mass distribution inside the earth and differs from the theoretical ellipsoid by a small amount. The dislocation between the geoid and the ellipsoid is called geoid undulation.

An expression for the geoid surface that is consistent with the second order expansion of the gravity potential in the Eq.(2.39) can be obtained as follows;

U at the equator - ( $\phi = 0^\circ$ ,  $r = a$ )

$$U_o = -\frac{GM}{a} + \left( \frac{GMa^2 J_2}{2a^3} \right) (3 \sin^2 \Phi - 1) - \frac{1}{2} \omega^2 a^2 \cos^2 \theta \quad (2.40)$$

$$U_o = -\frac{GM}{a} \left[ 1 + \frac{1}{2} J_2 \right] - \frac{1}{2} \omega^2 a^2 \quad (2.41)$$

Since the surface of the model earth is defined to be an equipotential surface, the value of the surface gravitational potential at the poles must be  $U_o$ , Here  $r = b$  and  $\phi = -\pi/2$

$$U_o = -\frac{GM}{b} \left[ 1 - \left( \frac{a}{b} \right)^2 J_2 \right] \quad (2.42)$$

The flattening (ellipticity) of the geoid is defined by Eq. (2.7)

As expressed above,  $U_o$  at the equator equals to  $U_o$  at the poles.

$$-\frac{GM}{a} \left[ 1 + \frac{1}{2} J_2 \right] - \frac{1}{2} \omega^2 a^2 = -\frac{GM}{b} \left[ 1 - \left( \frac{a}{b} \right)^2 J_2 \right] \quad (2.43)$$

Multiplying through out by  $-\frac{a}{GM}$  gives

$$1 + \frac{1}{2} J_2 + \frac{\omega^2 a^3}{2GM} = \frac{a}{b} \left( 1 - J_2 \left( \frac{a}{b} \right)^2 \right) \quad (2.44)$$

Substituting  $b = a(1-f)$  and neglect quadratic and higher order terms in  $f$  and  $J_2$

(since  $f \ll 1$  and  $J_2 \ll 1$ ) the final expression for  $f$  can be obtained as follows

$$f = \frac{3}{2} J_2 + \frac{\omega^2 a^3}{2GM} \quad (2.45)$$

Taking  $\frac{\omega^2 a^3}{2GM} = 3.46775 \times 10^{-3}$  and from satellite observation,  $J_2 = 1.0827 \times 10^{-3}$ ,

$f = 1/298.256$  is the ellipticity. This is valid only if the surface of the planetary body is an equipotential. The shape of the model geoid is nearly a spherical surface. If  $r_o$  is the

distance to the geoid then

$$r_o \approx a (1 - \varepsilon) \quad (2.46)$$

Where eccentricity  $\varepsilon \ll 1$ . By setting  $U = U_o$  and  $r = r_o$  in the gravity potential equation and substituting the gravity potential at the equator for  $U_o$  and  $r_o = a (1 - \varepsilon)$ , and neglecting quadratic and higher order terms in  $f$ ,  $J_2$ ,  $\frac{\omega^2 a^3}{2GM}$ , and  $\varepsilon$ :

$$\varepsilon = \left( \frac{3}{2} J_2 + \frac{\omega^2 a^3}{2GM} \right) \sin^2 \Phi \quad (2.47)$$

$$r_o = a(1 - \varepsilon) = a \left( 1 - \left( \frac{3}{2} J_2 + \frac{\omega^2 a^3}{2GM} \right) \sin^2 \Phi \right)$$

$$r_o = a (1 - f \sin^2 \phi) \quad (2.48)$$

where,  $f = \frac{3}{2} J_2 + \frac{\omega^2 a^3}{2GM}$

The non-dimensional quantity  $\frac{\omega^2 a^3}{GM}$  is a measure of the relative importance of the centrifugal acceleration due to the rotation of the earth compared with the gravitational attraction of the mass within the earth. The rotational contribution is about 0.33% of the mass contribution. In the above analysis it is considered only terms linear in  $J_2$  and  $a^3 \omega^2 / GM$ . In order to provide a reference geoid, against which geoid anomalies are to be measured, it is necessary to include higher-order terms. By convention, the reference geoid

is a spheroid (ellipsoid of revolution) defined in terms of the equatorial and polar radii by

$$\frac{(r_0 \cos \Phi)^2}{a^2} + \frac{(r_0 \sin \Phi)^2}{b^2} = 1 \quad (2.49)$$

The eccentricity of the spheroid is given by

$$\varepsilon = \frac{(a^2 - b^2)^{\frac{1}{2}}}{a} = (2f - f^2)^{\frac{1}{2}} \quad (2.50)$$

Using  $b = a(1 - f)$  in the spheroid equation and simplifying for  $r_0$  gives

$$r_0 = a \left( 1 + \frac{2f - f^2}{1 - f^2} \sin^2 \Phi \right)^{-\frac{1}{2}} \quad (2.51)$$

The difference in elevation between the measured geoid and the reference geoid  $\Delta N$  is referred to as a geoid anomaly. The maximum geoid anomalies are of the order of 100m; this is about 0.5% of the 21km difference between the equatorial and polar radii. The anomaly in the potential of the gravity field measured on the reference geoid  $\Delta U$  can be related directly to the geoid anomaly  $\Delta N$ . The potential anomaly is defined by

$$\Delta U = U_{m_0} - U_0 \quad (2.52)$$

where  $U_{m_0}$  is the measured potential at the location of the reference geoid and  $U_0$  is the reference value of the potential defined by Eq.(2.40). The potential on the measured  $U_0$ ,  $U_{m_0}$

and  $\Delta N$  are related by

$$U_0 = U_{m_0} + \left( \frac{\partial U}{\partial r} \right)_{r=r_0} \Delta N \quad (2.53)$$

since  $\frac{\Delta N}{a} \ll 1$ , the radial derivative of the potential in the Eq. (2.53) is the acceleration of gravity on the reference geoid, with remarkable accuracy which can be expressed as:

$$\left( \frac{\partial U}{\partial r} \right)_{r=r_0} = g_0 \quad (2.54)$$

where  $g_0$  is the reference acceleration of gravity. Just as the measured potential on the reference geoid differs from  $U_0$ , the measured acceleration of gravity on the reference geoid differs from  $g_0$ . Substitution of Eq. (2.53) and Eq.(2.54) into Eq.(2.52) gives

$$\Delta U = -g_0 \Delta N \quad (2.55)$$

Local mass excess produces an outward warp of gravity equipotential and therefore a positive  $\Delta N$  and a negative  $\Delta U$ . It should be emphasised that the measured geoid is essentially defines sea level. Deviations of the sea level from the equipotential surface are due to lunar and solar tides, winds and ocean currents. These effects are generally of the order of few meters. The reference acceleration of gravity on the reference geoid is found by substituting the expression for  $r_0$  given by Eq.(2.48) and Eq.(2.37) and simplifying the

result by neglecting quadratic and higher-order terms in  $J_2$ ,  $\frac{a^3 \omega^2}{GM}$

$$g_o = \frac{GM}{a^2} \left( 1 + \frac{3}{2} J_2 \cos^2 \Phi \right) + a\omega^2 (\sin^2 \Phi - \cos^2 \phi) \quad (2.56)$$

To provide a standard reference acceleration of gravity against which gravity anomalies are measured, it is necessary to retain higher order terms in Eq. (2.56). By international agreements in 1967 the reference gravity field was defined to be

$$g_o = 978031.846 [1 + 0.0052789 \sin^2 \phi - 0.000005 \sin^2 2\phi] \text{ mgal} \quad (2.57)$$

with  $g_o$  in  $\text{m/s}^2$ . This is the IGRS 1967 (International Geophysics Reference System) formula to calculate the theoretical gravity as a function of latitude ( $\phi$ ). Gravity anomalies are the differences between measured values of  $g$  on the reference geoid and  $g_o$  (Gerald, 1979; Tsuboi, 1983; Telford, 1990; Heiskanen and Moritz, 1967).

#### 2.1.4 Gravity Corrections

The magnitude of gravity (Eq.2.57) depends on latitude, elevation, topography, earth tides and density variations in the subsurface. Therefore, before comparing gravity measurements the following corrections must be done.

##### Latitude Corrections

Gravity increases with increasing in latitude. The variation of gravity with latitude over the surface of an ellipsoidal earth can be expressed using the theoretical gravity formula IGRS

1967 (Eq.2.57). The latitude correction  $\delta g_L$  is obtained by differentiating the theoretical gravity formula

$$\frac{\delta g_L}{\delta s} = \left( \frac{1}{R} \right) \frac{\delta g_\phi}{\delta \phi} = 0.811 \sin 2\phi \text{ mgal} \quad (2.58)$$

where  $R = 6371\text{km}$  is the mean radius of the earth,  $\delta s = R\delta\phi = \text{N-S horizontal distance}$  and  $\phi$  is the latitude angle (Telford, 1990).

#### **Free Air Correction.**

The free air correction takes into account the station height. When the elevation of a gravimeter increases, by the inverse-square law, the acceleration of gravity will decrease. So by correcting this change in gravity it is possible to reduce observations to a datum surface (Tsuboi, 1983). The correction is obtained by differentiating the scalar potential equation.

The gravity at a point located at a height  $h$  above the geoid is (Tsuboi, 1983)

$$g_h = \frac{GM}{R^2} \left( 1 + \frac{h}{R} \right)^{-2} \quad (2.58)$$

Applying the Binomial expansion for the term  $(1 + h/R)^{-2}$  and ignoring higher order terms and taking only the first two terms gives

$$g_h = \frac{GM}{R^2} \left(1 - \frac{2h}{R}\right) \quad (2.59)$$

The free air correction is therefore given by

$$\delta g_{FA} = g - g_h = \frac{2gh}{R} = 0.3086 \text{ hmGal / m} \quad (2.60)$$

The free air correction is added to the gravity reading when the station is above the geoid and subtracted when it is below.

### **Bouguer Correction.**

The Bouguer correction accounts for the attraction of excess material between the station and the datum plane, which is ignored in free air correction. If stations were located on a plateau of large horizontal extent and uniform thickness and density, gravity readings would be increased by the effect of this slab between the station and the datum plane. The gravity attraction for a point on the surface of a slab is obtained by the following expression.

$$\delta g_B = 2\pi G \rho h \quad (2.61)$$

where  $h$  is the height of the gravity station above the geoid and  $G$  is gravitational constant and  $\rho$  is density of the slab. For mean crustal density ( $\rho = 2.67 \text{ gm/cm}^3$ ) and  $h$  in meters, the Bouguer correction reduces to

$$\delta g_B = 0.1119h \text{ mgal/m} \quad (2.62)$$

### **Terrain Correction.**

The effects of surface irregularities in the vicinity of a station are considered in terrain correction. Terrain correction is done by computing graphically the gravity effect at the observation point of all the hills above the station level and all valleys below it. One such method is that of Hammer (1939). Specially designed transparent graticule is divided in to zones by circles, which are subdivided into compartments by radial lines. The total effect is the sum of each compartment, the effect of each compartment being computed by its average height. The gravity effect of a single sector is calculated from the formula.

$$\delta g_{\text{sec}}(r, \theta) = G \rho \theta [(r_o - r_i) + (r_i^2 - h^2)^{1/2} - (r_o^2 + h^2)] \quad (2.63)$$

where  $\theta$  is the sector angle in radians,  $h = |e_s - e_a|$ ,  $e_s$  is the station elevation,  $e_a$  is the average elevation in the sector, and  $r_o$  and  $r_i$  are the outer and inner sector radii respectively. The terrain correction,  $\delta g_t$ , is the sum of all the contribution of the sectors.

$$\delta g_t(r, \theta) = \sum_i \sum_\theta \delta g_{\text{sec}}(r, \theta) \quad (2.64)$$

### **Drift Corrections.**

The null reading value of a gravimeter changes gradually with time. The main cause of this drift is a creep in the springs. Even under well-controlled environment, at constant temperature, the spring and associated mountings and connections are not perfectly stable,

and slow or abrupt changes may occur. Therefore, drift correction accounts to such variations. Drift correction is made by checking the change in the reading of the gravimeter for a fixed station (base station) at every regular interval of time. The drift is the difference between the last and the first observations and it is usually positive. It is taken to be linear within these intervals.

### 2.1.5 Gravity Anomalies

Any local deviation of gravity from what is normally expected as regular or smooth trend is a gravity anomaly. Such anomaly is the final output of the data processing from which geological interpretation is made. In general free air anomaly gives information about the actual gravity information along the surface of the earth; while, Bouguer anomaly give information about hidden underground masses. (Tsuboi, 1983)

#### Free Air Anomaly.

Only the effect of elevation of a station from the geoid is considered by the free air anomaly. Here the attraction of materials between the elevation and the geoid will not be taken into account and that is why it is called the free-air.

$$\Delta g_{FA} = g_{obs} + 0.3086h - g_o \quad (2.65)$$

where  $g_{obs}$  = observed gravity,  $g_o$  = theoretical gravity and  $h$  =elevation.

#### Bouguer Anomaly.

Bouguer anomaly is the difference between the measured gravity value at the point of observation and the theoretical value calculated for that station, by considering a Bouguer slab of appropriate density for the effect of earth's material between the geoid and the station.

The Bouguer anomaly calculated by ignoring topographic effects is simple Bouguer anomaly (S.B.A).

$$S.B.A. = g_{obs} + 0.3086h - 0.1119h - g_o \quad (2.66)$$

When the free-air, Bouguer, and terrain correction are applied to the observed gravity, the resulting anomaly obtained by subtracting the standard theoretical gravity at the given latitude is called the complete Bouguer anomaly (C.B.A)

$$C.B.A = g_{obs} + 0.3086h - 0.1119h + \delta g - g_o \quad (2.67)$$

#### 2.1.6 Determination of Density

The density of rock in the vicinity of gravity profile is important in the calculation of the Bouguer plate and terrain correction. One way of determining appropriate density is to use a representative collection of rock samples with the aid of a geologic map. The specific gravity of a sample is found directly by weighing first in air and then in water, and applying Archimedes principle. This gives its density  $\rho$  relative to that of water:

$$\rho = \frac{W_a}{W_a - W_w} \quad (2.68)$$

Seismic velocity, gamma-gamma logging and borehole gravimetry help to find the density of rocks. From borehole gravimetry density can be calculated as

$$\rho = \left( 3.683 - 11.93 \frac{\Delta g}{\Delta h} \right) \times 10^3 \text{ kgm}^{-3} \quad (2.69)$$

There are other two methods devised by Parasinis, (1971) and by Nettleton, (1976) which use graphical methods.

## 2.2. THE RESISTIVITY METHOD

The electrical resistivity method is one of the principal geophysical exploration techniques. It utilizes both natural and artificial sources of electric current to study the electrical properties of rock masses of the subsurface. The large contrast in resistivity between ore bodies, fluid inside rocks, alteration mineral assemblages and their host rock is exploited in electrical resistivity prospecting. It is used to map lithologic layers and unique geologic structures.

In electrical resistivity method, artificially generated direct or low frequency alternating current is introduced into the ground through point electrodes; while, potential between two points on the ground is measured by other two point electrodes called potential electrodes. The subsurface rock resistivity variations affect the electrical current flow that affects the distribution of surface electrical potential. Divergence from the pattern of potential difference expected from a homogeneous ground provides information on the form of the subsurface anomalous mass that is referred to as resistivity anomaly (Parasnis, 1989)

Most rock masses are anything but homogeneous and isotropic in the electrical sense because they are full of fractures. In particular, shale, slates, limestone and schist have a definite anisotropy character, especially with respect to the host rock. Such rock units, with respect to their electric behavior, are referred as anisotropy mediums (Grant & West, 1965).

### 2.2.2. Fundamental Principles

The physical principle underlying this method is Ohm's law; which states that if a direct current is made to flow through a circuit element, the ratio of the potential drop across the element to the current flowing through it is a constant.

$$R = \frac{\Delta V}{I} \quad (2.70)$$

Assuming a uniform electrical current flowing through a homogeneous cylinder in the direction of its axis, the resistance will be proportional to the length (L) and is inversely proportional to the cross sectional area (A) of the cylinder i.e.,

$$R = \frac{\rho l}{A} \quad (2.71)$$

The constant of proportionality  $\rho$  is numerically equal to the resistance between opposite faces of a cube of unit dimensions cut from the material. It is called resistivity. Its unit is Ohmmeter ( $\Omega\text{-m}$ ).

Instead of considering the total current flowing through a finite volume it is possible to consider the current density field  $J$ ; and instead of the potential drop across the specimen, electric potential gradient  $E$ . Taking a small rectangular parallelepiped having linear dimensions  $\Delta x$ ,  $\Delta y$ ,  $\Delta z$ ; and assuming, no current discontinuity to happen in the material, the resistance across the parallelepiped can be written as:

$$R = \frac{\vec{E} \Delta z}{\vec{J} \Delta x \Delta y} = \frac{\rho \Delta z}{\Delta x \Delta y} \quad \Rightarrow \quad \rho = \frac{1}{\sigma} = \frac{\vec{E}}{\vec{J}}, \quad \text{or}$$

$$\vec{J} = \sigma \vec{E} \quad (2.72)$$

Where  $\sigma$  is called conductivity.

Where  $E$  is electric field in volts per meter and  $\sigma$  is the conductivity of the medium. Eq. (2.72) is another form of Ohm's law. It is applied to an isotropic medium.

This relation when applied to anisotropic mediums is expressed as:

$$\vec{J}_i = \sigma_{ik} \vec{E}_k \quad (2.73)$$

Where the conductivity ( $\sigma_{ik}$ ) now appears not as a scalar, but as a second-rank tensor. Elements of this tensor will be most significant depending on the nature of the anisotropy. When  $\sigma_{11} = \sigma_{22} = \sigma_{33} = \sigma$  and all other components of  $\sigma_{ik}$  vanish it reduces to the isotropic case.

### 2.2.2. General Equation for the Electrical Potential

The electric field is the gradient of the electric scalar potential,

$$\vec{E} = -\vec{\nabla} V \quad (2.74)$$

$$\vec{J} = \sigma \vec{\nabla} V \quad (2.75)$$

To obtain an equation for the potential, the principle of the conservation of charge is applied. Using this principle, across any surface S that encloses a volume within which there are no sources or sinks of electrical current is:

$$\oint_S \vec{J} \cdot \vec{n} ds \quad (2.76)$$

Hence, according to Gauss's theorem,

$$\vec{\nabla} \cdot \vec{J} = 0 \quad (2.77)$$

Therefore: -

$$\nabla(\sigma \nabla V) = 0 \quad (2.78)$$

$$\nabla \sigma \nabla V + \sigma (\nabla)^2 V = 0 \quad (2.79)$$

If  $\sigma$  is constant throughout, the first term vanishes and we have Laplace's equation, which is,

$$(\nabla)^2 V = 0 \quad (2.80)$$

This potential is harmonic function. There are two boundary conditions that must hold at any contact between two regions of different conductivity. The boundary condition for interfaces where  $\sigma$  and  $E$  change abruptly.  $E_{x1} = E_{x2}$

$$\sigma_1 E_{z1} = \sigma_2 E_{z2} \quad (2.81a)$$

Where, the x and z axes are tangent and normal to the ground, respectively, to the interface;  $E_{x1}$  is the tangential component of the electric field in medium 1, while,  $E_{z2}$  is the tangential component of the electric field in medium 2. From the continuity of the electric potential;

$$V_1 = V_2 \quad (2.81b)$$

Mostly two electrodes are used to supply a controlled electrical current to the ground. Such electrodes are called current electrodes. From the two current electrodes, there is a set of successive equipotential surfaces, in the form of a hemispherical surface. The potential difference between these equipotential surfaces can be measured where they intersect the ground surface using a second pair of electrodes called potential electrodes.

Consider the flow of current around an electrode that introduces a current I at the surface of a uniform half space the expression for electric field becomes.

From Eq.(2.70)

$$E = \frac{-dV}{dr} = \rho J = \frac{\rho I}{2\pi^2} \quad (2.82)$$

Taking the necessary boundary conditions (2.81a, 2.81b), the electric potential V at a depth r due to a single potential electrode located on the surface is:

$$V = \frac{\rho I}{2\pi r} \quad (2.83)$$

From this the ground resistivity can be expressed as

$$\rho = \frac{2\pi r V}{I} \quad (2.84)$$

Similar expressions can be found by solving the electric potential in spherical coordinates

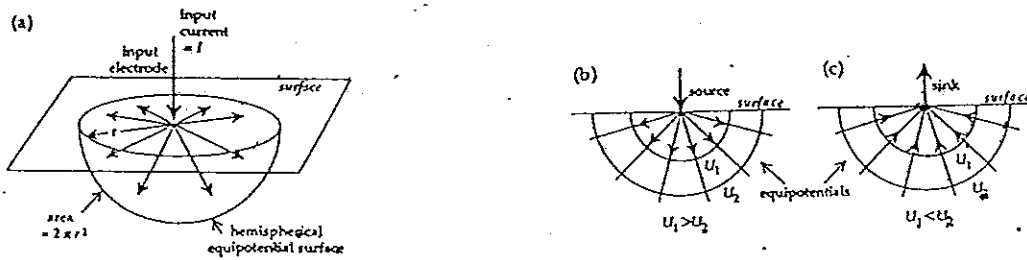


Figure 2.2 Electric field lines and equipotential surfaces around a single electrode at the surface around a single electrode at the surface of a uniform space. (Lowrie, 1997)

By subtracting from each other, two of Eq. (2.83), a relation for the potential at a point, due to a pair of current electrodes is obtained. The potential at a point  $r_1$  away from the source and  $r_2$  away from the sink is:

$$\Delta V = \frac{\rho I}{2\pi} \left( \frac{1}{r_1} - \frac{1}{r_2} \right) \quad (2.85)$$

This leads to the formula for the ground resistivity to any electrode configuration.

The electrical resistivity of the ground as measured by two potential electrodes after current is introduced to the ground by two other current electrodes is:

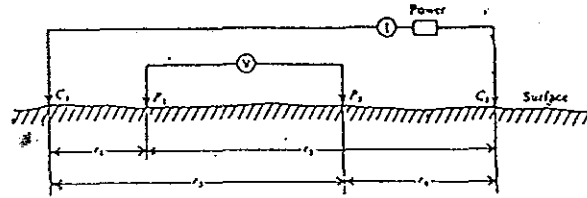


Figure 2.3. Two current and two potential electrodes on the surface of homogeneous isotropic ground of resistivity  $\rho$  ( After Telford, 1990)

$$\Delta V = \frac{\rho I}{2\pi} \left\{ \left( \frac{1}{r_1} - \frac{1}{r_2} \right) - \left( \frac{1}{r_3} - \frac{1}{r_4} \right) \right\} \quad (2.86)$$

Since this equation depends on the geometry of the array of electrodes the resistivity derived from this equation is an apparent resistivity.

$$\rho_{app} = \frac{2\pi\Delta V}{I} \left\{ \frac{1}{\left( \frac{1}{r_1} - \frac{1}{r_2} \right) - \left( \frac{1}{r_3} - \frac{1}{r_4} \right)} \right\} \quad (2.87)$$

Even though, there are several styles of electrode arrangements for resistivity survey the Schlumberger array is demonstrated below because in this study this array is utilized.

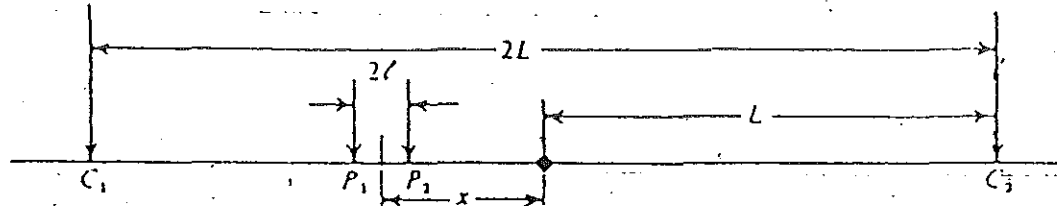


Figure 2.4. The Schlumberger array

Current electrodes are spaced much further apart than the potential electrodes.

When  $r_1 = (L - x) - l$ ,  $r_2 = (L + x) + l$ ,  $r_3 = (L - x) + l$  and  $r_4 = (L + x) - l$ , upon substitution of these values in equation (2.87) and approximating  $(L-x) \gg 3l$ ,

$$\rho_{app} = -\frac{\pi}{2l} \left\{ \frac{L^2 - x^2}{L^2 - x^2} \right\} \frac{\Delta V}{I} \quad (2.88)$$

$$\frac{L^2 - x^2}{L^2 + x^2} \quad (2.89)$$

Equation (2.89) is called geometric factor for this array because it varies with the current electrodes separation ( $2L$ ) and potential electrodes separation  $2l$ . The geometry of configuration for the electrodes affects the measured resistivity, which means that what is actually measured is not the true resistivity of the subsurface but is an apparent resistivity.

In Schlumberger spread the potential electrodes are closely spaced with respect to the current electrodes spread, implying that the measurement is effectively of potential gradient at the mid point (i.e.,  $l = x$ )

$$\rho_{app} = -\frac{2\pi L^2}{I} \left( \frac{\Delta V}{\Delta r} \right) \quad (2.90)$$

When  $2l = 2r \Rightarrow 0$  (very small)

$$\frac{\Delta V}{\Delta r} \Rightarrow \text{where, } \Delta V = \Delta r^2 (\partial^2 V / \partial r^2)$$

$$\begin{aligned} \Delta V &= \frac{I\rho_{app}}{2\pi} \left\{ \frac{1}{r} - \frac{1}{r-\Delta r} - \frac{1}{r+\Delta r} + \frac{1}{r} \right\} \\ &\cong -\frac{I\rho_{app}}{\pi} \left\{ \frac{\Delta r^2}{r^3} \right\} \end{aligned} \quad (2.91)$$

Using second approximation,

$$\rho_{app} \cong -\frac{\pi r^3}{\Delta r^2} \left\{ \frac{\Delta V}{I} \right\} \cong -\left( \frac{\pi r^3}{I} \right) \left\{ \frac{\partial^2 V}{\partial r^2} \right\} \quad (2.92)$$

### 2.2.3. A Point Electrode at the Surface of a Layered Ground

Taking  $n$  horizontally stratified layers with finite thicknesses and distinct resistivity it is possible to solve the electric potential for each layer assuming that each layer is homogeneous and isotropic but layers with different electrical properties.

Because of the presence of these layers, the potential will no longer have spherical symmetry about a given point '0' where the potential electrode is located. The solution of  $\nabla^2 V = 0$  of Eq.(2.86) in cylindrical coordinate system whose origin is at  $p$  and whose  $z$  axis is vertical

and positive in the downward senses is made to satisfy the continuity conditions at a number of horizontal boundaries.

$$\nabla^2 V = \frac{\partial^2 V}{\partial r^2} + \frac{\partial V}{r \partial r} + \frac{\partial^2 V}{\partial z^2} = 0 \quad (2.92)$$

The complementary solution of this equation is formed from the characteristic of the separated variables. By choosing only those well-defined terms as  $r \rightarrow 0$ , the complementary solution of equation (2.92) is obtained as

$$V(r, z) = \int_0^\infty [A(\lambda)e^{-\lambda z} + B(\lambda)e^{\lambda z}] J_0(\lambda r) d\lambda \quad (2.93)$$

It is known as the Stefanescu integral.  $\lambda$  is arbitrary constant,  $A(\lambda)$  &  $B(\lambda)$  are arbitrary functions of  $\lambda$  and  $J_0$  is the Bessel function of order zero.

To which we must add the particular solution  $V(r, z) = \frac{\rho_1}{2\pi R} I$  that applies within the close vicinity of P.

$$V_1(r, z) = \frac{I\rho_1}{2\pi R} + \int_0^\infty [A(\lambda)e^{-\lambda z} + B(\lambda)e^{\lambda z}] J_0(\lambda r) d\lambda \quad (2.94)$$

$$\text{for } 0 \leq z \leq h$$

If no boundary exists other than the surface  $z=0$ , then  $A(\lambda)=B(\lambda)=0$ . If there are boundaries,

then these coefficients will be determined from the boundary conditions. Since in the substratum there is no external source of current, terms involving  $e^{\lambda z}$  are rejected because the potential must remain finite when  $z \rightarrow \infty$ . Consequently, the potential in  $z \geq h$  is:

$$V_2(r, z) = \int_0^{\infty} C(\lambda) e^{-\lambda z} J_0(\lambda r) d\lambda \quad (2.95)$$

The boundary conditions, which these solutions must satisfy, are:

$$\frac{\partial V_1}{\partial z} = 0 \quad \Rightarrow \quad z = 0 \quad (2.96a)$$

$$V_1 = V_2 \quad z = h \quad (2.96b)$$

$$\frac{\partial V_1}{\rho_1 \partial z} = \frac{\partial V_2}{\rho_2 \partial z} \quad z = h \quad (2.96c)$$

Thus, the above relations are available to determine the three unknown functions A, B, and C.

To apply these conditions Lipschitz integral identity is required.

$$\frac{1}{R} = \int_0^{\infty} e^{-\lambda z} J_0(\lambda r) d\lambda \quad (2.97)$$

Then upon substituting for  $V_1$  and  $V_2$  in to Equation 2.96a, 2.96b, 2.96c and inserting  $\frac{I\rho_1}{2\pi R}$  in

to the constants, the following expressions can be arrived at

$$A - B = 0 \quad (2.98a)$$

$$(1 + A) e^{-\lambda h} + B e^{\lambda h} = C e^{-\lambda z} \quad (2.98b)$$

$$-\frac{1}{\rho_1} [(1 + A) e^{-\lambda h} - B e^{\lambda h}] = -\frac{1}{\rho_2} C e^{-\lambda h} \quad (2.98c)$$

Using creamer's rule to solve the above equations the solution for  $A$  and  $B$  becomes

$$A = B = \frac{I \rho_1 k}{2\pi (e^{2\lambda h - k})} \quad (2.99)$$

Where  $K$  is the reflection coefficient of Eq.(2.99). When  $z = 0$ ,

$$V_1(r) = \left( \frac{I \rho_1}{2\pi R} \right) \left[ 1 + 2kr \int_0^\infty (e^{2\lambda h} - K)^{-1} \right] J_0(\lambda r) d\lambda \quad (2.100)$$

$$V_1(r) = I \rho_1 / 2\pi \int_0^\infty \{1 + 2 A_1(\lambda)\} J_0(\lambda r) d\lambda \quad (2.101)$$

$$A_1(\lambda) = K_1 \frac{e^{-2\lambda h}}{K_1 e^{-2\lambda h}} \quad (2.102)$$

$$V(r) = \frac{I \rho_1}{2\pi} \int_0^\infty K(\lambda) J_0(\lambda r) d\lambda \quad (2.103)$$

where,  $K(\lambda)$  = Slichter Kernel function (after Slichter, 1933)

Stefanescu integral can be solved for any number of layers. For Schlumberger array, the resistivity transform  $T(\lambda)$  (introduced by Koefoed, 1970) is defined in terms of resistivity  $\rho$  and Slichter Kernel function  $K(\lambda)$  as

$$T(\lambda) = \rho K(\lambda) \quad (2.104)$$

$T(\lambda)$  is very important in the interpretation of resistivity sounding.

For the Schlumberger array approximating the apparent resistivity by:

$\rho_{app. schl.} = -2\pi L^2 / I \{(\partial V / \partial r)_{r=L}\}$ .  $\partial / \partial x (J_0(x)) = -J_1(x)$ , which is Bessel function of order one then the apparent resistivity takes the form:

$$\rho_{app. schl.} = \rho_1 + 2\rho_1 L^2 \int_0^\infty A_1(\lambda) J_1(\lambda s) \lambda d\lambda,$$

or using the transform function

$$\rho_{app. schl.} = \rho_1 + s^2 \int_0^\infty [T(\lambda) - \rho_1] J_1(\lambda s) \lambda d\lambda \quad (2.105)$$

The above equation shows the relationship between apparent resistivity function and apparent resistivity for the Schlumberger array.

## 2.2.4. Current Distribution in a Horizontally Stratified Earth

The current pattern in a uniform half-space extends laterally on either sides of the profile line. To evaluate the depth of penetration of current in a uniform half-space, Orthogonal Cartesian Coordinate with the x-axis parallel to the profile and the z-axis vertical gives:

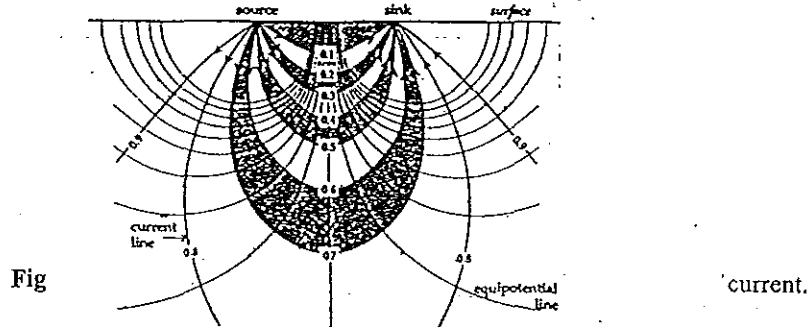


Figure 2.5. Equipotential surfaces between a source and a sink of current.

Let the spacing of the current electrodes be  $L$  and the resistivity of the half space is  $\rho$ . The horizontal electric field  $E_x$  at  $(x, y, z)$  is

$$E_x = -\frac{\partial V}{\partial x} = -\frac{\partial}{\partial x} \left\{ \frac{\rho I}{2\pi} \left( \frac{1}{r_1} - \frac{1}{r_2} \right) \right\} \quad (2.106)$$

Where  $(x^2 + y^2 + z^2)^{1/2} = r_1$  and  $r_2 = [(L - x)^2 + y^2 + z^2]^{1/2}$

Differentiating and using equation (2.72)

$$J_x = \frac{I}{2\pi} \left\{ \frac{x}{r_1^3} + \frac{(L - x)}{r_2^3} \right\} \quad (2.107)$$

If  $(x, y, z)$  is on the vertical plane mid-way between the current electrodes

$x = \frac{L}{2}$  and  $r_1 = r_2$  and the current density is given by

$$J_x = I \frac{L}{2\pi} \left( \left( \frac{L}{2} \right)^2 + y^2 + Z^2 \right)^{\frac{3}{2}} \quad (2.108)$$

The horizontal current  $dI_x$  across an element of area ( $\delta y \delta x$ ) in the median vertical plane is  $\delta I_x = \delta J_x \delta y \delta x$ . The fraction of the input current  $I$  that flow across the median plane above a depth  $z$  is obtained by integration:

$$\frac{I_x}{I} = \frac{L}{2\pi} \int \frac{1}{\left( \frac{L}{2} \right)^2 + Z^2} dZ = \frac{2}{\pi} \tan^{-1} \frac{2Z}{L} \quad (2.109)$$

This equation helps to find the fraction of current between any two depths found from the difference in the fraction above each depth. When a current meets an interface between two layers the resistivity contrast of the layers expressed by a K-factor is defined as the reflection coefficient as:

$$K = \frac{\rho_1 - \rho_2}{\rho_1 + \rho_2} \quad (2.110)$$

And also the electrical laws of reflection holds true as:

$$\frac{\tan \theta_1}{\tan \theta_2} = \frac{\rho_1}{\rho_2} \quad (2.111)$$

Half the current crosses the plane above a depth  $Z = L/2$  will never penetrate below the depth  $Z = 2L$  as much as 70.5 % and almost 90 % passes above the depth  $Z = 3L$  (Lowrie,

1997, Parasnis, 1986)

### 2.2.5 The Effects of Temperature and Porosity on Resistivity

All minerals and semiconductors increase their conductivity with increase in temperature according to the equation (Parasnis, 1986),

$$\sigma = \sigma_o e^{\frac{E}{kT}} \quad (2.112)$$

K = Boltzman constant, T = temperature,  $\sigma$  = original conductivity of the rock, E = energy gap or activation energy for the subsurface in question. However, the activation energy is poorly known for most rocks. On the other hand, the resistivity of porous water -bearing rocks (without clay minerals) follows Archie's law

$$\rho = \rho_o f^{-m} S^{-n} \quad (2.113)$$

where  $\rho$  is the resistivity of the water filling the porous space,  $f$  is the porosity (volume fraction porous),  $S$  is the fraction of porous space filled by water and  $n$ ,  $m$  are certain parameters. The value of  $n$  is close to two, if more than 30 % pore space is filled with water. The value of  $m$  depends upon the degree of cementation. It varies from about 1.3 for loose tertiary sediments to about 1.95 for well-cemented Paleozoic ones (Parasnis, 1986).

## **CHAPTER III**

### **DATA ACQUISITION, PROCESSING AND PRESENTATION**

#### **3.1 THE GRAVITY METHOD**

For dependable interpretation accurate gravimetric measurements and cautious data reduction are desired. Meyer (1974) briefly elucidates gravity data acquisition, reduction, process and interpretation in few steps as follows:

- A. Collection of gravity values on the earth's surface;
- B. Computing Bouguer values;
- C. The irregularly spaced gravity values are interpolated onto a square grid;
- D. Regional residual separation to isolate components of small and large size;
- E. Several interpretation and filtering techniques are used to obtain a better insight in to the composition of the field;
- F. A model fitting technique is applied in order to obtain a geologic model that could produce the observed part of the surface field.

##### **3.1.1. Field Procedures and Data Acquisition**

Generally, for any gravity survey (principally for regional) the absolute gravity value must be recognized from the near by primary base station whose absolute gravity value is known in the International Gravity Standardization Network 1971 (IGSN71). If the survey line is not conveniently close to such a primary base, secondary base stations must be established by repeated difference measurements (ties). To maintain the accuracy level of the Bouguer

anomaly it is beneficial to establish many base stations for checking drift as many times as possible. Different individuals can collect gravity data at different times using different secondary base stations. All the data collected at different time referring to different secondary base stations should be brought to the same datum to make as if all the data were collected from the same base station. To get this, the gravimeter reading is multiplied by the instrument conversion factor and after the instrument drift correction is carried out the normal and absolute gravity of each data point is obtained. The elevation record of every station is necessary for terrain and free air corrections.

### **3.1.2 Gravity Data Processing and Presentation**

To produce the Bouguer anomaly map using discrete gravity anomaly values that are located at random points on the ground, the random data should be converted to line data through appropriate interpolation technique to apply filters. In this study the linear interpolation technique is used. Interpolation, in general, assigns values to points that have originally no measured data values, depending on the selected searching radius and grid cell. Interpolation is a must, since it is not possible to take infinite measurements that represent the infinite points on the earth's surface. The linear interpolation, in this study, gives gravity values for most of the areas covered by water body such as Lake Langano, Lake Ziway, Lake Abijata and Lake Shala. In places, where the gravity data points are at great distance to each other, beyond the searching radius, gravity values are not assigned. Areas like south of Butajira, East of Langano and north of Butajira, due to the density and spreading of the data points (Fig. 3.1), it was not possible to assign values by interpolation. Of course, values can be assigned for these areas by choosing a large searching radius; however, this will introduce large error in the Bouguer anomaly.

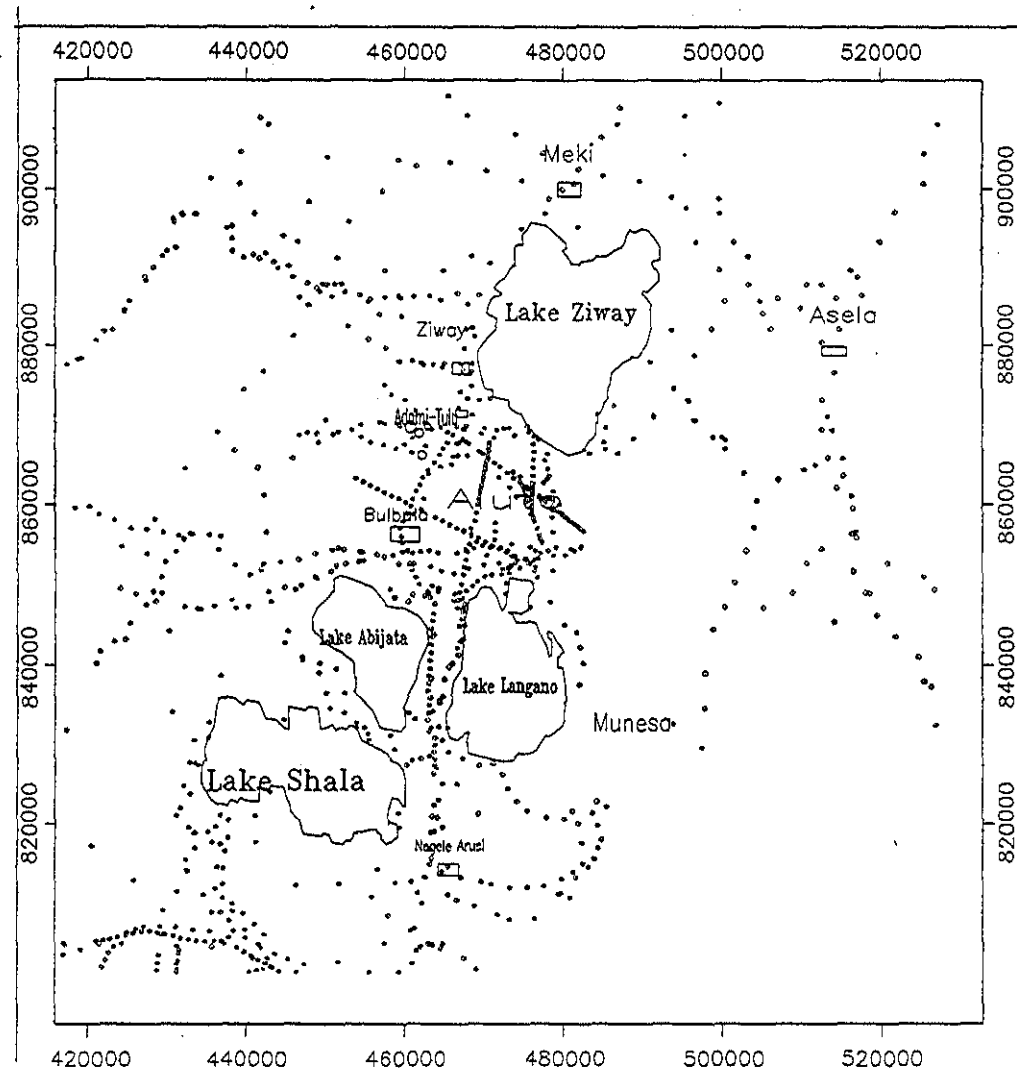


Fig. 3.1 Gravity data location

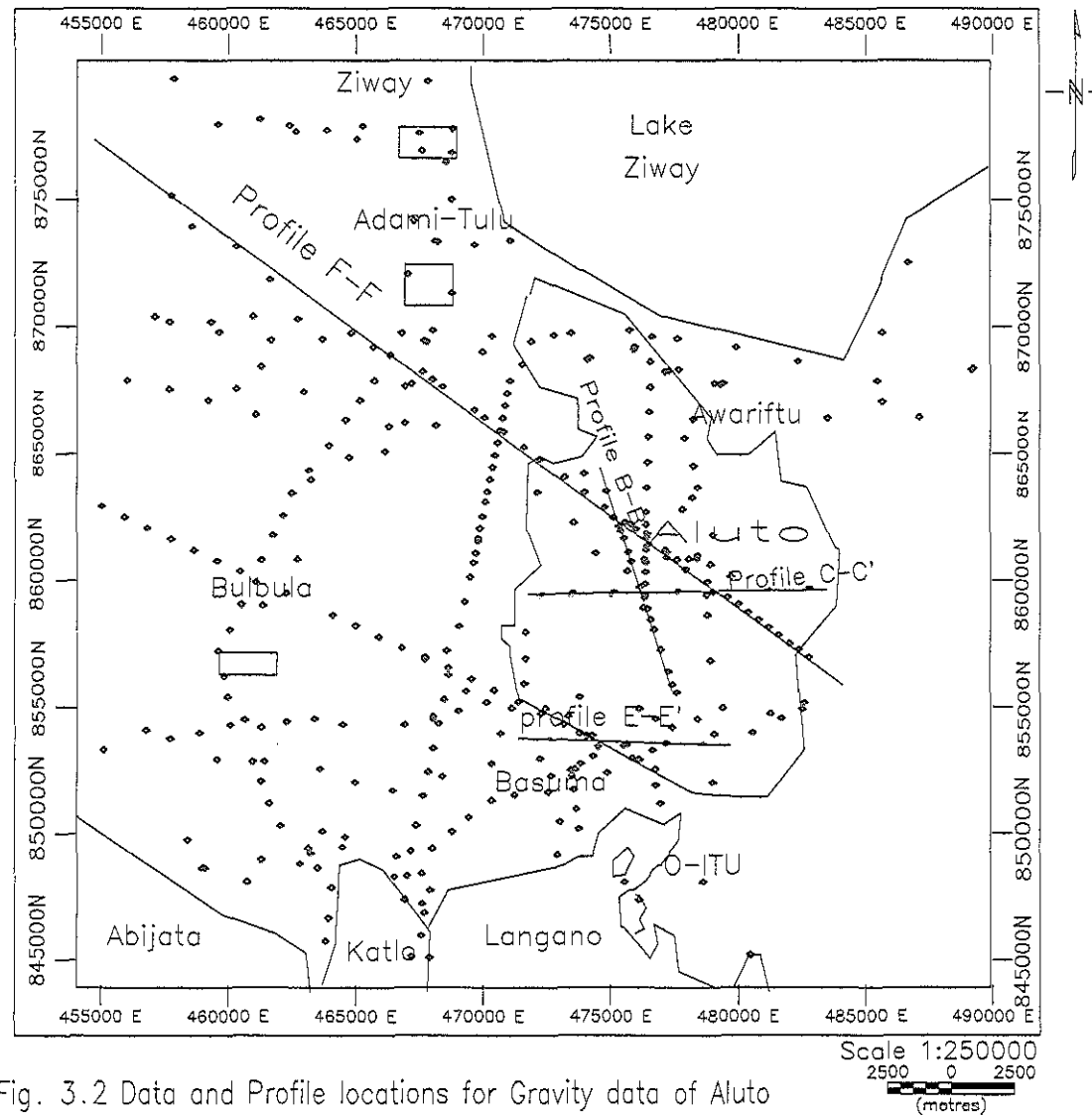


Fig. 3.2 Data and Profile locations for Gravity data of Aluto

Here, gridding software called GRID.CON (in GEOSOFT, 1994) is used. To assign a pixel value to a point on the map the program does mathematical averaging of all points found within the searching radius by giving different weights ( $1/r^2$ ). This has also another advantage of suppressing high frequency surface noises. Points at far spot from the center of the circle prescribed by the searching radius are given less value than those near the point under consideration. In gravity data analysis interpolation is advantageous to estimate the gravity value of a point based on a balanced composition of the field records in the vicinity the gravity field itself measured at a point is the result of the gravity field contribution of many anomaly sources.

All potential field filters in MAGMAP (GEOSOFT, 1994) work in wave number or frequency domain. The foundation of wave number filtering is that all continuously varying functions of distance  $x$  or time  $t$  are considered to be made up of sine and cosine curves of various wavelengths, amplitudes and phase (Fig. 3.3). Gravity profiles are functions of space ( $x, y$ ) and it can be defined in the wave number domain. Gravity field is a non-periodic function. Non-periodic functions can be considered to have wavelengths ranging from zero to infinity. The transition from space domain to wave number domain is done by Fourier transform. Zadro (1984) has showed the steps to Fourier transform of the gravity potential (and its space derivative, the gravity field) from the space domain to the wave number domain and vice versa, and how the wave number transformation furnishes grid sampling.

Gravity is a continuously varying field in  $x, y$  space with no discontinuity (Meyer, (1980) has showed the process of digitization of this continuous field. When this field is transformed to wave number domain data processing is much faster than in the space-domain. Bouguer

gravity profiles (such as Fig. 3.3) are functions of distance or space working in the space domain. However it is measured at finite number of discrete points.

Making use of the Fourier transformation from space to wave number domain Bhattacheryya, (1964), Spector and Grant (1970) developed the power spectrum (the square of the Fourier amplitude) analysis for potential fields to estimate the depth to the top of a statistical ensemble of blocks of anomaly sources. Gupta & Remani (1980) have clearly stated the use of the power spectra plot developed by Spector and Grant (1970). A single straight line fitted to a part of the spectrum (Fig 4.2 and Fig. 4.10) corresponds to a single average depth.

The mean depth to each ensemble is estimated analytically from the graph using Macleod's (1986, in Asfaha, 1990) relation as:

$$\text{Average depth to a statistical ensemble} = -\frac{\ln(E)}{4\pi} \quad 3.1$$

where, E = radially averaged power spectrum.

For any type of qualitative and quantitative interpretation, the gravity field sampling (station separation) is very decisive. Gravity field can be sampled from few meters interval to tens of kilometers interval depending on the type of survey. Detail surveys demand very precise measurement with sampling interval in few meters while for regional gravity survey the sampling interval can be in kilometers. In the present study the gravity data is not line data and is sampled from 500m to tens of kilometers intervals (Fig 3.1 and Fig.3.2).

When a gravity field is sampled, from a Bouguer map, along a profile a curve is obtained.

Any such profile from the Bouguer map, taken in the space domain,  $\delta x$  being the sampling interval, the wave number which is sampled twice per cycle is called the Nyquist wave number or folding wave number that is given by:

$$\nu_N = \frac{1}{2\delta x} = \frac{1}{\lambda_n} \quad 3.2$$

where,  $\lambda_n$  is the Nyquist Wavelength.

In this thesis, to make gravity profiles, the sampling intervals are 500m for profile F-F' and 100m for profile B-B', C-C' and profile E-E'. Hence, the Nyquist wavelengths are 1000m and 200m. While the Nyquist wave number of folding wave numbers are:

$$\nu_N = \frac{1}{2\delta x} = \frac{1}{\lambda_n} = \frac{1}{2000\text{ m}} = 0.0005\text{ m}^{-1} \text{ and}$$

$$\nu_N = \frac{1}{2\delta x} = \frac{1}{\lambda_n} = \frac{1}{2 \times 1000\text{ m}} = 0.0005\text{ m}^{-1}$$

Principally, wave numbers less than the Nyquist wave number can perfectly be sampled, but those greater than or less than  $\nu_n$  will be distorted. Regular sampling loses no information provided that the sampling frequency is greater than twice the highest frequency component in the waveform being sampled. Therefore, length of the Fourier wavelength considered during sampling is 200m for the first three and 1000m for the last modeling. By doing so it is tried to minimize the sampling error. The quantitative approach as to the ability of identifying the smallest possible spherical anomalous body found at a depth of  $Z_c$  with the given sampling interval is shown by Childers et al, (1999):

$$\text{Fourier wavelength} = 4 \times \text{geologic wavelength} = 3.1 Z_c. \quad 3.3$$

Therefore, for Fourier wavelength = 200 m  $\approx 3.1 Z_c \Rightarrow Z_c = 200 \text{ m} \div 3.1 \approx 34 \text{ m}$ , and for Fourier wavelength = 1000m  $\approx 3.1 Z_c \Rightarrow Z_c = 1000 \text{ m} \div 3.1 \approx 333 \text{ m}$

Sampling the gravity data every 100m is sampling the interpolated gravity field at twice less than the smallest original sampling interval that is 500m and the ability to identify a small anomaly at a depth of 34m can be erroneous. While the result found by sampling the gravity field at 500m is more reliable. This is also reflected on the gravity models (Fig. 4.20a and Fig. 4.21 as well as Fig. 4.21a and Fig. 4.21b)

To extract more information from the Bouguer anomaly data on the location and orientation of the anomaly source different filters are applied. A major step in the analysis of the gravity data is the process of isolating observed anomaly patterns in to regional and residual components. As explained by Gupta and Ramani, (1980) the definition of regional is purely subjective. What is considered regional in one's consideration is taken as residual for another depending upon the nature of the information sought from the data. The separation of regional from residual is challenging due to the fact that gravity anomaly is the sum of overlapping gravitational effects of two or more separate geologic structures of varying dimensions and depth. Therefore, the interpretation of gravity can be confusing without geological information.

In the separation of the residual from the regional many types of filters (that are believed to be relevant to the study) are employed. Band pass filter, low pass filter, high pass filters and vertical derivatives filters found in MAGMAP (first developed by Paterson, Grant and Watson limited) are used. The polynomial surface trend is also employed in the separation of

the residual from the regional. To use all the filters using the wave number domain, first the Bouguer gravity plotted in Fig. (4.1) and Fig. 4.10) in the space domain must be converted to wave number domain by the Fourier transformation.

The band pass filter works in the wave number domain and selects only specific range of wavelength to pass and reject any wavelength above or below the boundary of selection. By doing so, a group of anomaly sources at a particular depth are selected (This is also the theoretical base of the radially averaged power spectrum method developed by Spector and Grant, 1970). These zones of the gravity field source are then interpreted (Figs. 4.6, 4.7, 4.15, 4.16, 4.19). In this study the band pass filter is able to separate layers that are called gravi-stratigraphic layers only up less than 500m. Band pass filter is used in the same way as used by Corredo and Rapolle (1981) for crustal modeling technique. Here it is to delineate various lithologic horizons that show similar density contrast.

The low pass filter applied in this study (Figs. 4.4, 4.5, 4.12, 4.13, 4.14) are employed to pass wave number below a particular selected wave number to refer to those deep anomaly sources that contribute gravity field for the regional. While, the high pass filter applied in this study (Fig. 4. 3) is to allow high wave number and reject low wave number. This is to get a residual gravity anomaly map by filter out the gravity field of the shallow source from the deep sources.

Other most frequently used filters are vertical derivatives. In this study first and second order vertical derivatives are used. However vertical derivatives up to order 5 were prepared but due to the sampling interval and the error in the Bouguer anomaly computations the

derivative of order 3 and above appear to show artifacts.

The first vertical derivative  $\frac{\partial g}{\partial z} = -\frac{\partial^2 V}{\partial z^2}$  and the second vertical derivative  $\frac{1}{2 \times 1000 \text{ m}}$ , tending to magnify near surface features by increasing the power of the linear dimension in the denominator. This is because the gravity effect varies inversely as the distance squared, while the first, second, and higher derivatives vary as the inverse of the 3<sup>rd</sup>, 4<sup>th</sup> etc Telford et al, (1990) powers respectively. Successive higher vertical derivatives enhance near surface effects at the expense of deeper anomalies.

Polynomial trend surface residualizing method is used to compare the result with that found by the low pass filtering (Figs.4.11). The Polynomial trend surface is simply representing the regional long wavelength anomaly by a low order analytical surface. The analytical surface is determined by a least square fit (Agocs, 1951 in Telford ,1990). The assumption is that as the order of the polynomial increases the residual will be a representative of the surface geology of the area of interest. In this study only the second order polynomial trend surface is used. The mathematical explanation for the second order polynomial trend surface is:

$$\Delta g(x,y) = Ax + By + 2cxy + Dx^2 + Ey^2 + F \quad 3.4$$

For the quantitative study of the Bouguer gravity of the region trend surface, band pass filters, vertical derivatives, low pass and high pass filters are used to separate the regional from the residuals. From the Bouguer map about 4 profiles were selected and gravity models are prepared by using the gravity modeling software GM-SYS version 3.50G

All the raster and contour maps were produced by the standard gravity and magnetic processing and mapping software called GEOSOFT, (1994, 1995). To grid the gravity maps for Aluto and its surrounding a grid cell size of 200m and searching radius of 7500m are used, while for Aluto a grid cell size of 100m, and a searching radius of 3500m is employed. Terrain correction is applied by the method of Hammer (1939) up to M Zone for which topographic map of 1:50,000 scale is used. Maximum terrain effect obtained is 1.95mgal. Estimation of densities of rocks is taken to be the average value of crustal density  $2.67 \text{ g / cm}^3$ . And to see by how much this value defers from the true value for reduction density about three profiles (Fig 3.4a, 3.4b and 3.4c) were taken and compared. According to Nettleton, (1976) the density that results in the best correlation of the Bouguer profile to the topography plot of the same profile is selected. Accordingly, the profiles witnessed that the selected reduction density did not produce noticeable error on the data processing.

### 3.1.3 Homogenization and Anomaly Conversion of the gravity data

Secondary-gravity-data collected from any organization can be tricky in handling if the data is collected in dissimilar datum points (IGSN71 and the POTSDAM system). The normal gravity value used can be in the old (1930) gravity formula or the current (1967) gravity formula. However, every reduction and processing is preferable if the IGSN71 and the 1967 gravity formula are used. The anomaly conversion first discussed by Woollard, (1979) can plainly shun the trouble by treating the Free Air anomaly value at sea level.

$$FA_{old} = g_{old} - \gamma_{old} \quad (3.5)$$

Where,  $g_{old}$  is observed gravity value on an absolute base of the Potsdam system;  $\gamma_{old}$  is the old theoretical sea level gravity value (1930). Using the new gravity system:

$$g_{\text{new}} = g_{\text{old}} - g_{\text{cor}} \quad (3.6)$$

Where,  $g_{\text{new}}$  is assumed observed gravity value in the IGSN71 system and  $g_{\text{cor}}$  is the datum correction.

$$\gamma_{\text{new}} = \gamma_{\text{old}} - \gamma_{\text{cor}} \quad (3.7)$$

Where,  $\gamma_{\text{old}}$  = old theoretical sea level gravity value,  $\gamma_{\text{new}}$  = the new theoretical sea level gravity value and  $\gamma_{\text{cor}}$  datum correction. The new free air gravity correction is

$$FA_{\text{new}} = g_{\text{new}} - \gamma_{\text{new}} \quad (3.8)$$

Substituting Eqs.3.2 and 3.3 in Eq.3.4

$$FA_{\text{new}} = FA_{\text{old}} - g_{\text{cor}} + \gamma_{\text{cor}} \quad (3.9)$$

However, the elevation values in the old and new systems remain invariant. The conversion of Bouguer anomaly values from the old to the new system can similarly be expressed as:

$$BA_{\text{new}} = BA_{\text{old}} - g_{\text{cor}} + \gamma_{\text{cor}} \quad (3.10)$$

The datum correction for the theoretical gravity value is expressed as follows (Parasnis, 1986)

$$g_{1930} - g_{1967} = (172 - 136 \sin^2) \text{ m/s}^2 \quad (3.11)$$

$$g_{1967} = (g_{1930} + 136 \sin^2 - 172) \text{ m/s}^2 \quad (3.12)$$

Substituting  $7.25^\circ$  and  $8.25^\circ$  (the study area's latitude boundaries) values for  $\phi$  in Eq. (3.12), the datum values come to be 16.93658mgal and 16.91997mgal, respectively. On the other hand, the absolute gravity value correction can be established by comparing the absolute gravity values of the POTSDAM and IGSN71 for the same primary stations. By taking the absolute IGSN71 gravity value of 977452.16mgal and of the POTSDAM value of 977467.07mgal of the Addis Ababa Geophysical Observatory primary base, the difference appears to be 14.91mgal. From Eq. (3.4):

$$\begin{aligned} BA_{\text{new}} &= BA_{\text{old}} - g_{\text{cor}} + g_{\text{cor}} = BA_{\text{old}} + (\delta_{\text{cor}} g_{\text{cor}}) \\ &= BA_{\text{old}} + (14.91 - 16.91997) \text{ mgal} \\ &= BA_{\text{old}} - 2.09 \text{ mgal.} \end{aligned}$$

If data in-homogeneity occurs, then it is possible to isolate the data by computing the free air anomaly Eq.(2.65). If the elevation reprocessed from the free air anomaly computed based on the new gravity standardization does not confirm to that of the previous then the datum used in the original reduction is concluded to be of the older system; but if it comes out to be the same then there is no datum in-homogeneity.

## 3.2 THE RESISTIVITY METHOD

### 3.2.1 Field Procedures and Data Acquisition

The Schlumberger array is mostly used in vertical electrical sounding for its better depth of penetration and that it is less sensitive to lateral in-homogeneities because the potential electrodes remain fixed during a number of successive measurements with expanding current electrodes.

In this study the current source used was alternating current of low frequency. When alternating current is used the current has the tendency to concentrate at the surface of the earth (skin effect) (Koefoed, 1979). For a homogeneous isotropic earth model, the alternating current density decreases exponentially with depth according to the equation  $j_z = j_0 e^{-\frac{z}{\xi}}$ ; where,  $j$  is the current density,  $Z$  = the depth, and  $\xi$  is a constant with physical dimension of a length, commonly referred to as the depth of penetration of the current. The magnitude of the depth of penetration depends both on the frequency of the alternating current and on the resistivity of the ground. The equations relating these quantities to each other is  $\xi = \sqrt{\frac{\rho}{\pi \mu f}}$ ; where,  $\rho$  is the resistivity and  $\mu$  is the magnetic permeability of the ground material and  $f$  is the frequency of the alternating current. This equation shows the inverse relationship between the current's depth of penetration and the frequency of the alternating current.

There are two basic field procedures that are used in resistivity work: Resistivity Sounding and Resistivity Profiling. Resistivity profiling is employed for lateral investigation of the

resistivity of rocks. The interpretation of resistivity profiling data is mostly qualitative and is aimed at delineating zones of anomalous resistive zones. The procedure used in resistivity profiling is to keep the electrode separation of the array fixed whilst moving the entire array along a line from one station interval to another. This is to maintain an approximately constant depth of investigation and look for lateral variations in resistivity.

Resistivity sounding is a depth investigation procedure. It is to determine the variations of resistivity with depth. Resistivity sounding is taken by gradually expanding the array of the current electrodes. This is to increase the current's depth of penetration. The depth of investigation of an array depends of the electrode separation and also on the distribution of resistivity of the ground. As a rule-of-thumb the approximate depth of investigation is from  $1/3$  to  $1/5$  of the current electrode separation.

The basic equipment required for the electrical resistivity survey consists of a transmitter, a receiver, steel electrodes and electrical cables. The instruments used were: Scientrix IIR-10 15kw transmitter and IP receiver/ $f=0.125\text{HZ}$ . A steel wire is used to connect the two ends of stainless steel current electrodes (A and B) to the transmitter output terminals and the potential electrodes (M and N) to the receiver input terminal. (This information is taken from the VES data sheet). The half current electrodes separation ( $AB/2$ ) used are: 10m, 20m, 40m, 70m, 100m, 147m, 215m, 316m, 464m, 681m, 850, 1000m, 1470m, 1810m, 2700m and 3160m with overlaps at 100m, 147m, 464m, 681m, 850m, 1000m, 1235m, 1470m, 1810m and 2150m. The respective potential electrode separation ( $MN/2$ ) are: 2m, 4m, 8m, 15m, 30m, 100m, 150m, 200m, and 350m.

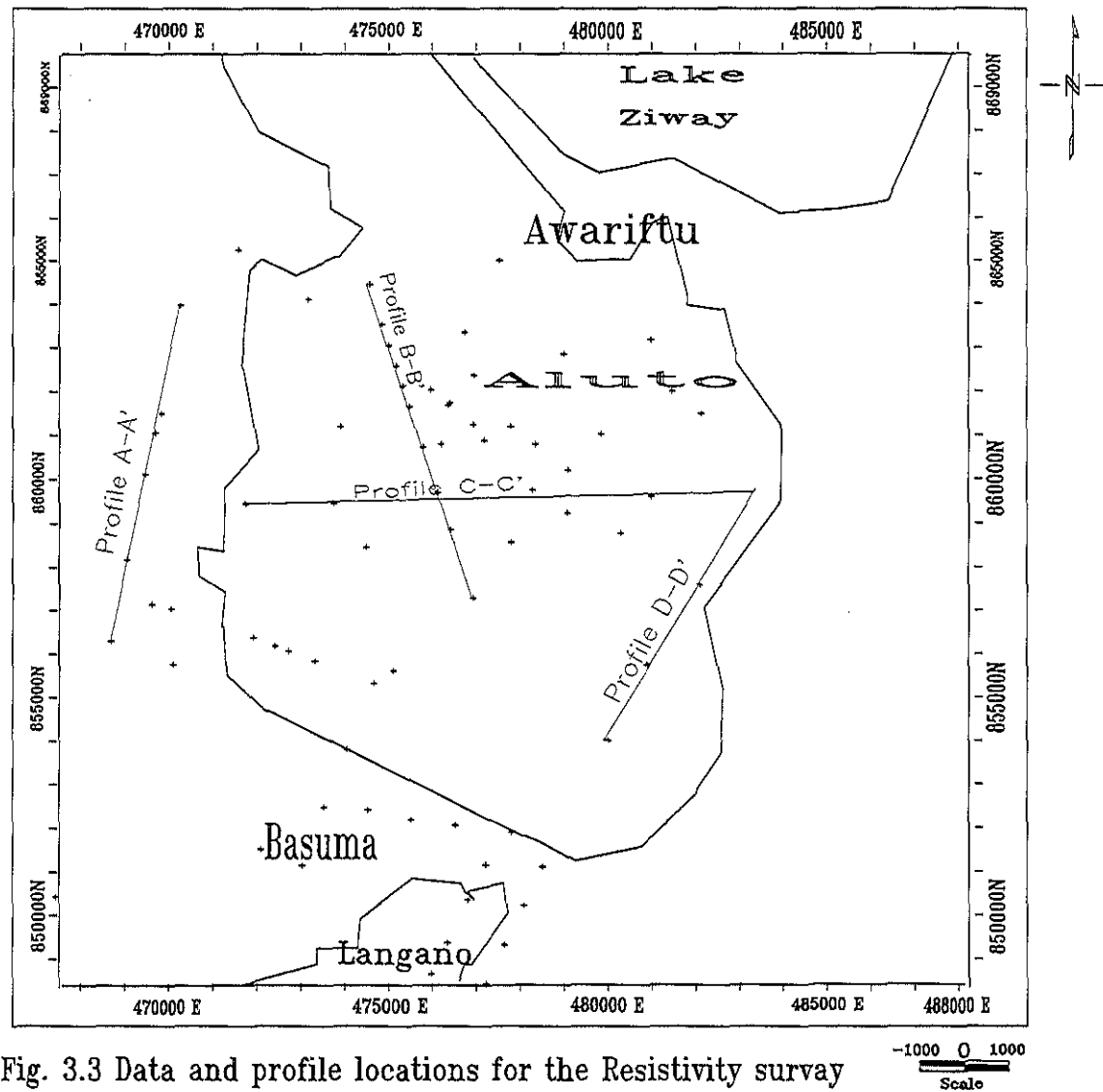


Fig. 3.3 Data and profile locations for the Resistivity survey

### 3.2.2 Resistivity Data Processing and Presentation

The apparent resistivity data obtained are presented in a map form for  $AB/2=10\text{m}$ ,  $AB/2 = 100\text{m}$ ,  $AB/2 = 1000\text{m}$  and  $AB/2 = 2100\text{m}$ . The maps are prepared by GEOSOFT mapping and processing software (1994) with a grid cell size of 100m and a blanking radius of 3000m. About four profiles are taken from these maps as profile plots (Fig. 4.28a, Fig.4.29a, Fig 4.30a and Fig. 4.31a)

The VES data were plotted on a bi-logarithmic graph paper of modules 62.5mm. The preliminary interpretation was done using partial curve matching technique using two-layer master curve and auxiliary point chart curves (H, K, Q and A types). The layer parameters obtained by this technique were used as initial model parameters for the inversion done by computer program RESIST87. The program has an option to fix some model parameters from well-known sources and has 30 iterations. The iteration for this study was performed from 30 to 60 times by controlling the appearing parameters by the depth information from the deep geothermal wells. This is to determine true depth and true resistivity values of the ground and minimize the ambiguity from the equivalency problem. Good to excellent sounding curves were obtained with RMS error less than 2.5%. The final layer parameters were plotted against elevation to make a geoelectric section. The apparent resistivity data was also gridded and contoured to produce pseudosection using (GEOSOFT, 1994). This is just to see the apparent resistivity distribution along the selected profiles.

One of the first step in the interpretation of VES data is curve matching. It helps to get initial model parameters. The curve matching procedures is briefed as follows:

1. Plot the field data on log-log paper, with  $\rho_{app}$  as ordinate and  $AB/2$  as abscissa
2. Fit the first part of the field curve with a two layer standard curve, by keeping the axes parallel to the 2-layer master curve. Read  $\rho_1 = \rho_2 / R_1$  from the value of the matched curve. Mark as  $O_1$  the origin of the master curve on the field curve read  $\rho_1$  and  $t_1$  (values

that are coordinates of the origin of the master curve on the field curve). The value of  $\rho_2$  is computed from the relation  $\rho_2/\rho_1 = \rho_1'/\rho_1$

3. Using  $O_1$  as origin trace the approximate auxiliary curve, corresponding to the value of  $\rho_2/\rho_1$  and the shape of the field curve. Keep axes parallel.
4. Remove the auxiliary curves. Fit the next part of the field curve with a standard two layer curve on the auxiliary curve traced in 3.
5. The position of the origin of the standard curve on the auxiliary curve for the best fit gives the position and coordinate of the auxiliary point  $(\rho_1', t_1')$ . Also read the value of  $\rho_2'/\rho_1 = \rho_3/\rho_1$  from the standard 2-layer master curve. Thus the value of  $\rho_3$  is found.
6. The value of  $t_2/t_1$  is determined from the position of the auxiliary point on the auxiliary curves: This gives  $t_2$ .
7. The process continues by repeating steps 3-6 using the auxiliary  $t_2/t_1$  point as origin replacing  $\rho_3/\rho_1$  etc. until the field curve is exhausted.

In this study all the four types of curves are found: H-type ( $\rho_1 > \rho_2 < \rho_3$ ), K-type ( $\rho_1 < \rho_2 > \rho_3$ ), A-type ( $\rho_1 < \rho_2 < \rho_3$ ) and Q-type ( $\rho_1 > \rho_2 > \rho_3$ ).

The two layer master curve and the auxiliary point charts plotted by the image point method are prepared by Orellana and Mooney, (1966).

### 3.3. GEOPHYSICAL DATA INVERSION AND THE PROBLEM OF EQUIVALENCY

Geophysical data can be interpreted quantitatively as forward and inverse modeling problems. In the direct modeling techniques the geophysical problem has a unique solution while in the inverse problem the geophysical problem has infinite solutions. In a least-squares procedure of the inverse method a mathematical model based on prior knowledge

of the geology plus additional information from the general appearance of the profiles and contours is given in a limited number of parameters and are allowed to vary (iteration).

In inverse modeling, any given geophysical data set can have many models that can fit the data equally well or a given model can be obtained from many other data sets of possible anomaly sources (Telford et al., 1990).

To minimize the equivalency problem in gravity modeling, the information found from the power spectrum analysis is used. In VES interpretations, even though it is possible to estimate the number of layers from the field curve, different number of layers with different resistivity values can match a single resistivity curve (Koefoed, 1979). To ease this crisis in the interpretation of resistivity the well information are taken to constrain the thickness of resistivity layers. In this study softwares, RESISIT 87 and GM-SYS 3.05G did the inversion processes of resistivity and gravity, respectively.

### **3.4 EVALUATION OF ERRORS**

It is crucial to figure out or at least speculate the error that emerges in measurements or during data analysis to evaluate the accuracy level of the quantitative interpretations.

In gravity survey the possible errors come up from the precision in determining the geodetic latitude ( $\delta\phi$ ), precision in determining the elevation of the station ( $\delta h$ ), the reduction density ( $\delta\rho$ ), the reading of the observed gravity value ( $\delta g$ ), the normal gravity value and the instrument's accuracy. During data processing, error can also arise by interpolation from the selection of poor searching radius. That is  $\Delta g = \Delta g(g, h, \rho, \phi)$ .

From the general formula of error propagation (Taylor, 1983), for independent and random-errors in  $g$ ,  $h$ ,  $\rho$ ,  $\phi$  and (error from different sources) to be measured with uncertainties in  $\delta g$ ,  $\delta h$ ,  $\delta \rho$ ,  $\delta \phi$  and the propagation of errors in the point Bouguer gravity value can be expressed as

$$\delta g^2 = \left( \frac{\partial(\Delta g)}{\partial g} \delta g \right)^2 + \left( \frac{\partial(\Delta g)}{\partial h} \delta h \right)^2 + \left( \frac{\partial(\Delta g)}{\partial \rho} \delta \rho \right)^2 + \left( \frac{\partial(\Delta g)}{\partial \phi} \delta \phi \right)^2 + \sigma^2$$

From the point Bouguer Anomaly reduction given in (Eq.2.67), from the Bouguer plate formula Eq. (2.61) and from the normal gravity formula (Eq.2. 57) it is possible to get expression and evaluate the error according to the above expression. The total error, in this study, accordingly is estimated to be 1.98mgal. On the other hand, the quantitative interpretation of resistivity survey has to pass through inverse modeling technique. The VES interpretation depends on the initial number of model parameters: depth and resistivity values. The final error in matching the field to the theoretical curve is computed by RESIST87. The maximum error during iteration process in the resistivity interpretation is from 0.5 to 2.5 %. The error found during the inversion process is the only quantitative error that could be assessed in this survey. It is found difficult to assess errors introduced in resistivity interpretation through any other factor, on quantitative bases.

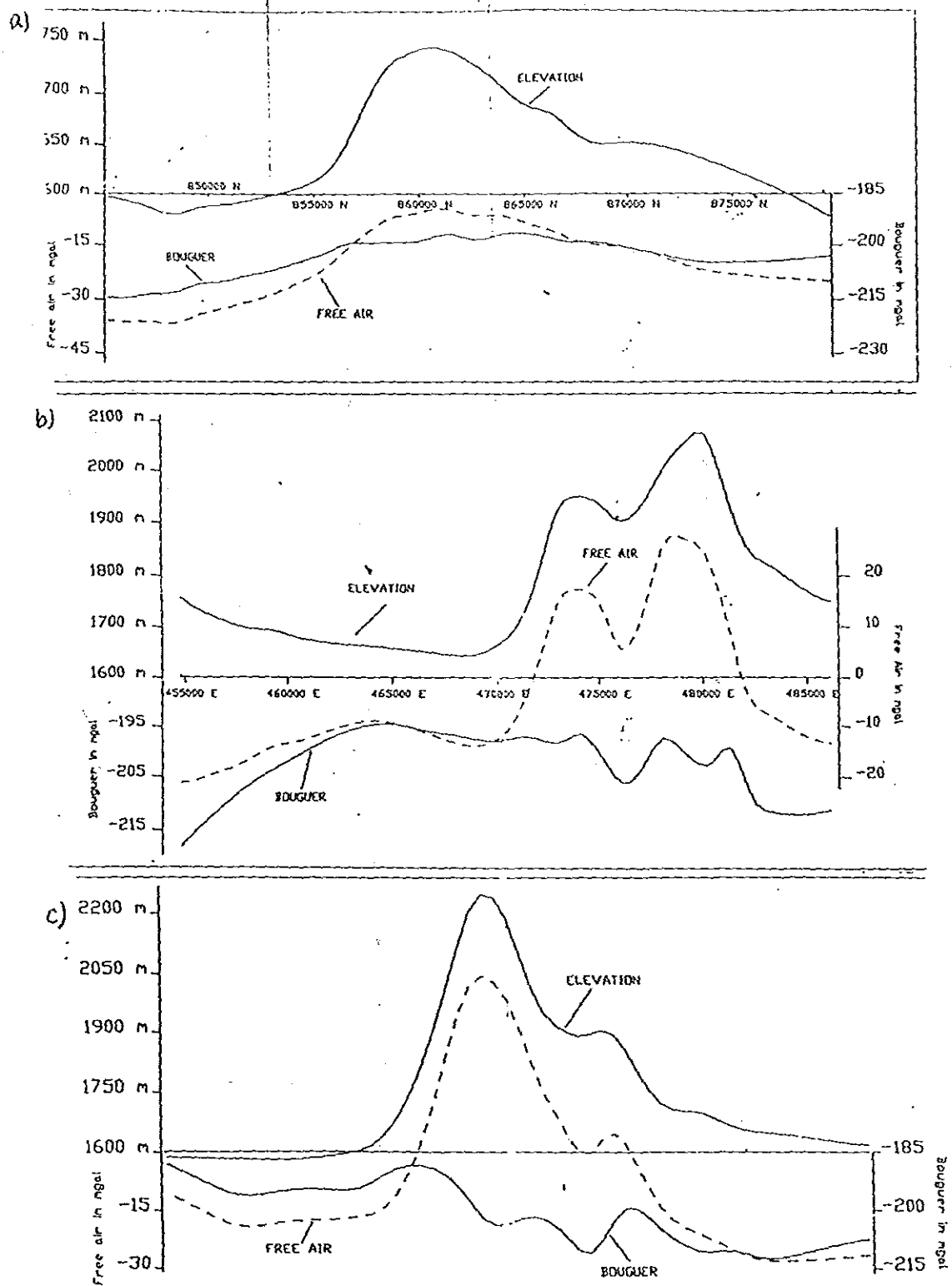
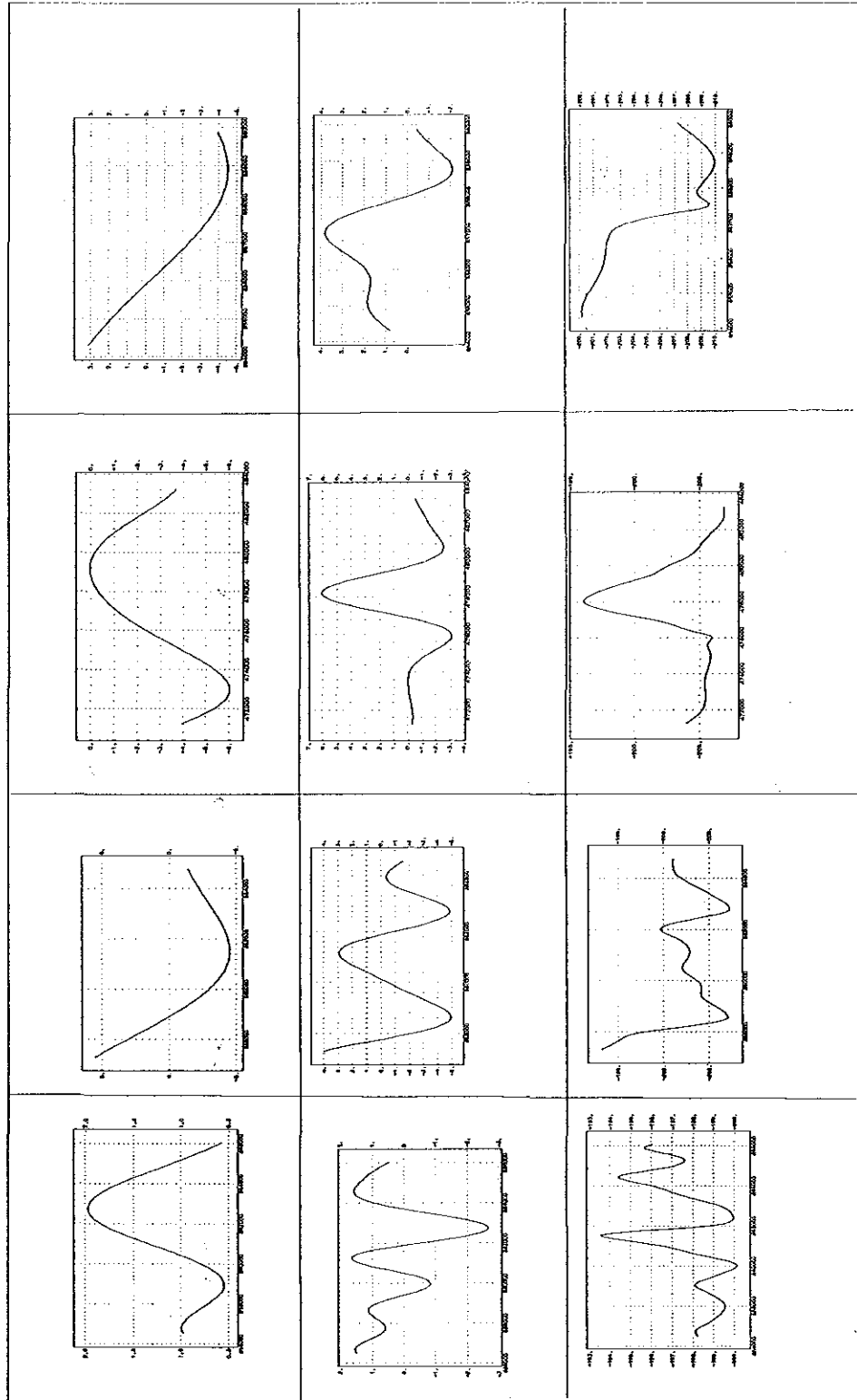


Figure 3.4 Gravity profiles to check the selected Bouguer density

# Gravity Profiles

A-A'      B-B'      C-C'      D-D'



Regional

Residual

Bouguer anomaly

Fig. 3.5 Wavelength decomposition of the Bouguer anomaly of Auro

## **CHAPTER IV**

### **RESULT AND INTERPRETATIONS**

#### **4.1 RESULTS AND INTERPRETATION OF GRAVITY DATA**

Gravity method is convenient in the searching of geothermal energy resources by determining the depth of the geothermal reservoir and by spotting geological structures that are associated with geothermal energy resources. Duprat, (1987) mentioned that the majority geothermal areas demonstrate significant positive gravity anomaly to tens of milli-gals. Positive residual gravity anomalies are caused by volcanic intrusions, densification of host rocks by hydrothermal minerals through deposition in fractures, removal of low-density mineral and replacement by denser hydrothermal alteration products. While negative residual gravity anomalies could be caused by ash flows, thick pyroclastic deposits, replacement of denser minerals by lighter hydrothermal minerals and lowering of the densities of the formations due to thermal expansion.

##### **4.1.1 Qualitative Interpretations of the Gravity anomaly maps.**

###### **The Bouguer Anomaly maps of Aluto and it's Surrounding.**

The Bouguer anomaly map (Fig. 4.1) discloses indications of the structural features of the study area and the anomalous subsurface mass distribution causing sporadic high Bouguer anomalies and long wavelength regional negative anomalies caused by upwelling anomalous mantle material to higher levels of the crust.



This anomaly map shows that the Values of the Bouguer anomaly in the study area ranges from a least value of -255 mgal to a highest value of -185 mgal (and on the residual anomaly map (Fig. 4.3) from -20mgal to +20mgal ). The Bouguer gravity value here in the rift is commonly negative. This negative value of Bouguer field in the rift is explained in two different ways. Chorowicz et al., (1987) considers this gravity negative in the Ethiopian Rift as caused by crustal thinning.

"...Lithospheric thinning produces regional gravity minimum, which approximately centered on the rift valley...a larger negative anomaly is still associated with the rift, but a narrow positive anomaly may form as a result of inter rift horst blocks and intrusion." (Swain, 1992 in Doser and Keller, 1999)

Conversely, (Gess et al., 1978; Fairhead, 1979; and Lysack, 1987: in Rogers et al., 1999) argue that this strong negative anomaly in the rift is caused by the anomalously hot, low-density, low velocity mantle at shallow depth (all related to mantle pluming).

Fig. (4.3) gives a better account of Bouguer anomaly map of Aluto in terms of positive highs and negative lows. It is the residual gravity map of the same region found after removing the regional by a band pass filter of wave number 0.008cycl/km. Thus, the Corbetti-Shala section of the WFB sited on southern part of Shala is discernible by relatively positive Bouguer anomaly values, reaching to positive 20 mgal. This is mutually from deep-seated intrusive bodies following the Corbetti-Shala segment of the WFB and from the Pleistocene Basalt flows (WoldeGebriel, 1999). From Ziway extending NNE in the direction of Gademsa is marked by relatively high Bouguer anomaly value, the involvement of which is both from the

deep intrusive bodies related to the east Ziway-Gadamsa segment of the WFB and Pleistocene basalts (WoldeGebriel et al., 1999). The Pleistocene basalt flows associated with the Silte-Debrezeit fault belt are marked by positive Bouguer anomalies reaching to positive 10 mgal. A positive 20 mgal Bouguer anomaly at the northern part of lake Langano bay and southern part of Aluto was depicted by many authors such as Searle and Gouin, (1972) and UNDP, (1973) as a rhyolitic intrusion. There is also positive 20-mgal gravity high near Adami-Tulu the cause of which is found to be an intrusive body (will be described in the subsequent maps). Other strong positive Bouguer gravity values at mount Bora and another at the NW top of the map marked by positive 20 mgal both of which are related to Basaltic intrusions and basaltic flows. A positive 20 mgal strong gravity anomaly is observed at Munisa mountain and continues to the SSW. It is clearly that the gravity response from the silicic volcanic mountain (Aluto) is masked by the north-Langano and the Adami-Tulu positive Bouguer anomaly values. All the strong negative gravity values are described in the section below.

### **The Regional Anomaly Maps of Aluto and it's Surrounding**

The Bouguer anomaly map (Fig 4.1) and its radially averaged power spectrum plot on Fig. (4.2) show that the observed anomaly can be at any depth as far as its gravitational field can be detected. However, small gravity anomaly sources produce gravity field detectable only in their vicinity (short wavelength) while large geologic bodies produce strong gravity field that can be felt at a significant distance from the point of source (long wavelength). What is at a far distance (at a depth) is called regional and is less significant for the immediate need of man.

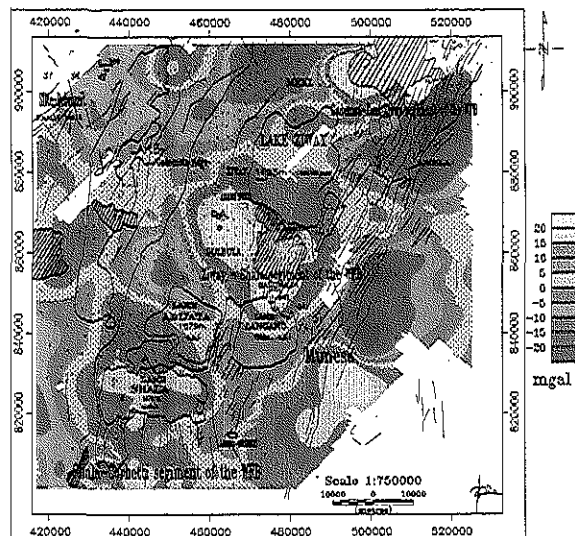


Fig. 4.3 Residual gravity anomaly map of Aluto and its environs found by applying a highpass filter with cut-off wavenumber of 0.0225cyl/km

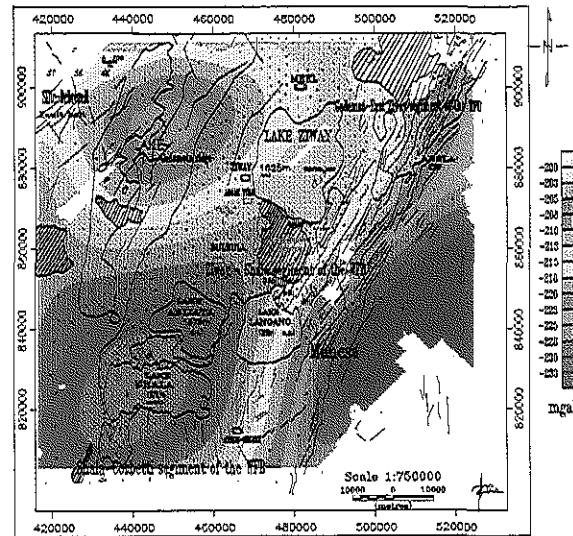


Fig. 4.4 Regional gravity anomaly map of Aluto and its environs after a lowpass filter with cut-off wavenumber of 0.015cyl/km is applied.

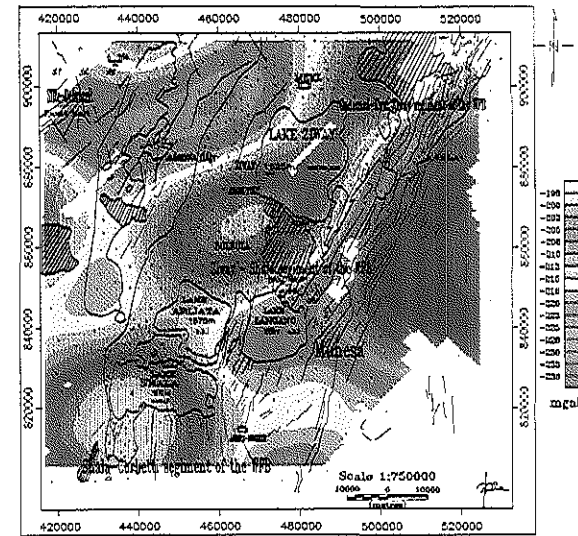


Fig. 4.5 Regional Bouguer anomaly map of Aluto and its environs found after applying a lowpass filter with cut-off wavenumber of 0.0225cyl/km

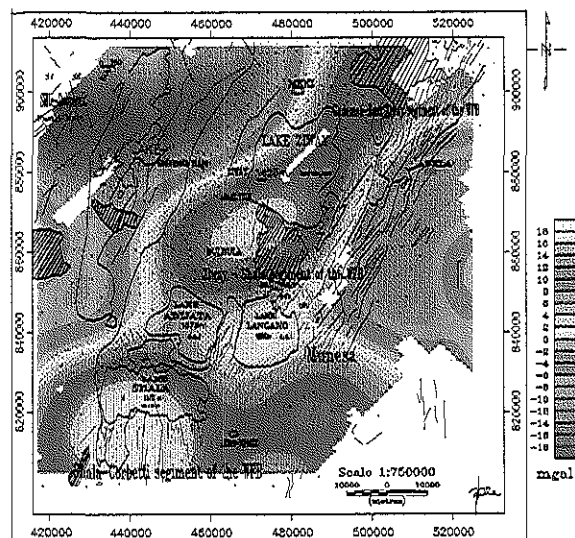


Fig. 4.6 The deepest gravi-stratigraphic layer found after applying a bandpass filter with cut-off wavenumbers of 0.008cyl/km and 0.0225cyl/km

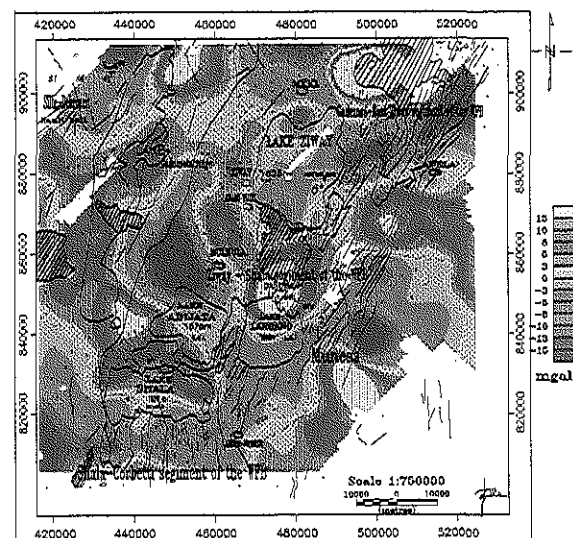


Fig. 4.7 Gravi-stratigraphic layer found after applying a bandpass filter with cut-off wavenumbers 0.0225cyl/km and 0.128cyl/km

Therefore, in most interpretation work deep gravity anomaly sources are filtered out and the remaining /residual is interpreted. In this thesis work a lot of regional-residual separation techniques are employed (Figs. 4.3, 4.4 & 4.6). The regional Bouguer anomaly found after subtracting a third order polynomial surface trend and those found by applying low pass filter with cut-off wave number of 0.015cyc/km and 0.0225cyc/km show a high density intrusive body (that is taken to be a magmatic intrusion) centered at Shala. This intrusion is at an estimated depth of 10 to 12km.

At about 7 to 10km (Fig. 4.5) a high-density anomalous region forms a belt following the direction of main axis of the WFB. In this belt there is another small nearly circular intrusion northern part of Aluto indicating that at this depth there is a relatively shallow intrusive body. These regional maps show the connection of the Aluto geothermal sources to the rest of the rift.

### **The Residual Anomaly Maps of Aluto and its Surroundings**

The residual gravity maps (Fig. 4.6 & Fig. 4.7) produced here are found by applying a band pass filter using the cut-off wave numbers 0.008cyc/km, 0.0225cyc/km and 0.0225cyc/km, 0.128cyc/km. The result of the band pass filter with cut-off wave numbers of 0.008cyc/km - 0.0225cyc/km show the deepest gravi-stratigraphic layer that contains what is previously considered as magmatic-intrusions. From the radially averaged power spectrum results this layer is expected to have a thickness of about 15 to 19km at a depth 7 to 10 km from the surface. This is expected to be the Basement Complex (?). The intrusion about Shala is able to make a Bouguer gravity anomaly contrast of 36mgal with the host rock. Here the place of extension fractures at the main axis of the WFB are accompanied by magmatic and basaltic

intrusions to result in a relatively high Bouguer anomaly, further strengthening the existence of a geothermal heat source abundant along this axis of extensional fractures. The residual Bouguer anomaly map of Fig. 4.7 shows that the short wavelength gravity sources at a depth of few hundreds of meters to a depth of 5 to 7 km. Here the main Bulbula and Abijata (east-dipping half-graben deep basin) situated at the western side of Aluto and northern part of Abijata making a minimum Bouguer anomaly contrast of -16 mgal. The central basin of lake Langano marked by a relatively low Bouguer value of -5 mgal, the Ziway basin marked by relatively low Bouguer value of about -5 mgal, the Meki and Awash basins located at the north- central part and north-western part of the map. While, the remaining relatively low Bouguer anomaly sources are related to Pleistocene tephra and recent sediments found abundant in the study area. In these Bouguer gravity maps the gravity highs are related to volcanic intrusions and basaltic flows that are assumed to be the sources of heat for the geothermal energy in the study area. The main structural trends identified by the gravity survey are expected to facilitate the hydrothermal fluids circulation. While all the relatively low Bouguer gravity minimums are related to the rift shoulders and sedimentary deposits in the rift basins. Of all these the prominent anomalies mentioned here above focus will be made to the anomaly of the Aluto complex and its surroundings where a separate detailed map is generated.

### **The Free Air Anomaly Map of Aluto**

The free air anomaly raster map of Aluto (Fig. 4.8) shows a strong positive correlation with the topography (contour map) of the study area.

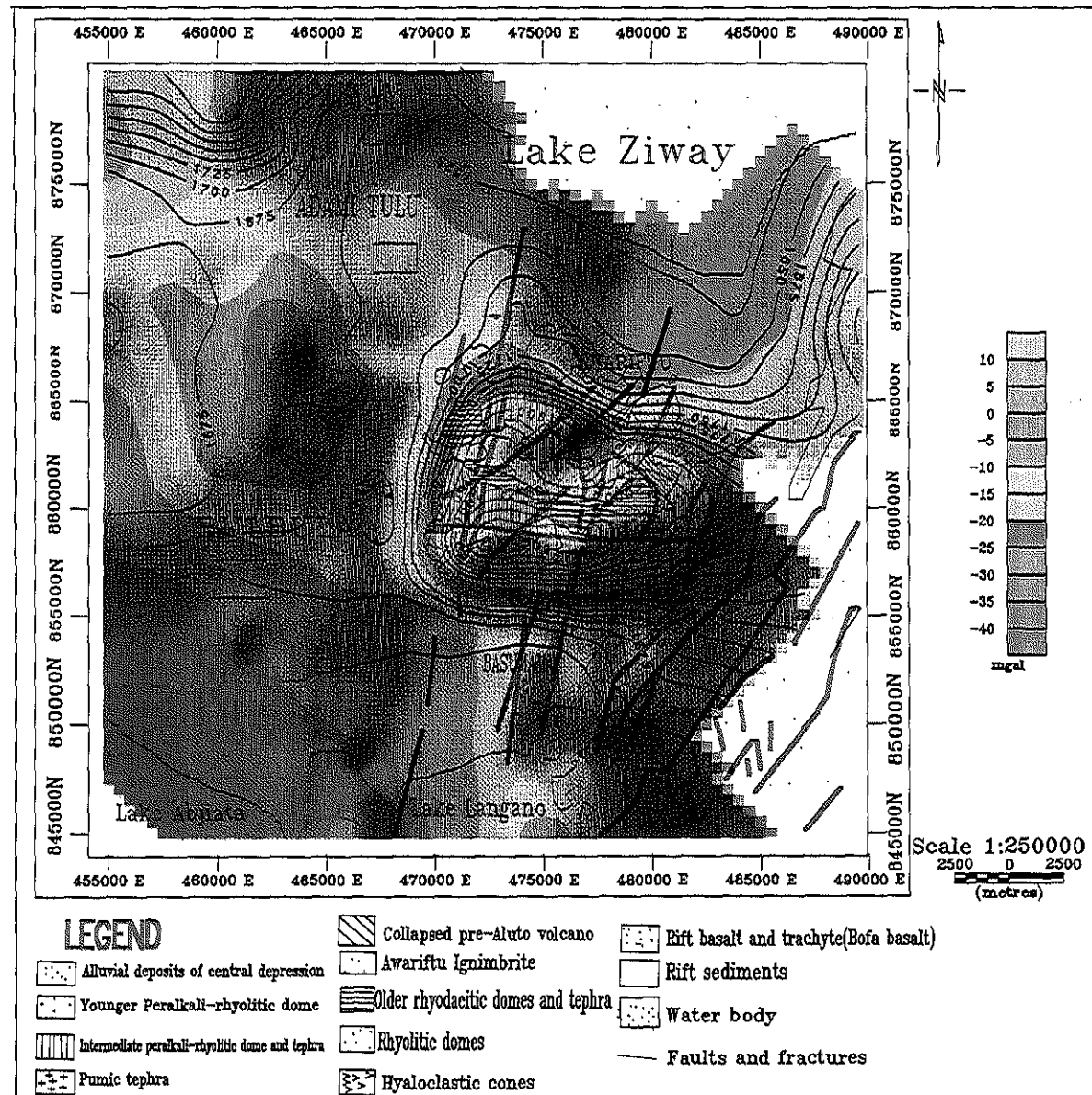


Fig. 4.8 Free air anomaly map of Aluto superposed on the elevation contour

It shows that it has a maximum positive value of 10 mgal/m at the top of mount Aluto where it has a maximum elevation value of 2328 m and it has a minimum negative value of -40 mgal/m towards lake Abijata where the elevation is about 1575 m. The free air anomaly in general shows the distribution and vertical-gradient of the gravity field on the surface of the earth; while, the Bouguer anomaly shows the density distribution of the subsurface (Tsuboi, 1983). Here in this study the Bouguer anomaly map is considered more useful than the free air anomaly.

### **The Bouguer Anomaly Map of Aluto**

For the anomaly map of Aluto (Fig 4.9), the smallest data interval is 500m that correspond to a Nyquist wave number of 1cycl/km. In the Bouguer anomaly map of Aluto the values range from a minimum of -220 mgal towards the Bulbula-Abijata basin to a maximum value of -190 mgal at the north Langano and south of Adami-Tulu. Most major anomaly causes were discussed in the former discussion. In this anomaly map the summit of Aluto shows relatively low Bouguer anomaly value as compared to Adami-Tulu and the northern Bay of Langano. This is interpreted as the sedimentary deposit of the central depression, the volcanic ash and pyroclastic materials on the top of the mountain. The composition of Aluto volcanic products are mostly silicic, and silicic rock in general have low density, therefore it makes it doubtful to find an intrusive body in kilometer depth just beneath the central part of Aluto that is the cause for the geothermal energy of Aluto. Specially, at what is considered as the up flow zone by ELC, (1986) and T/Mariam (1996).

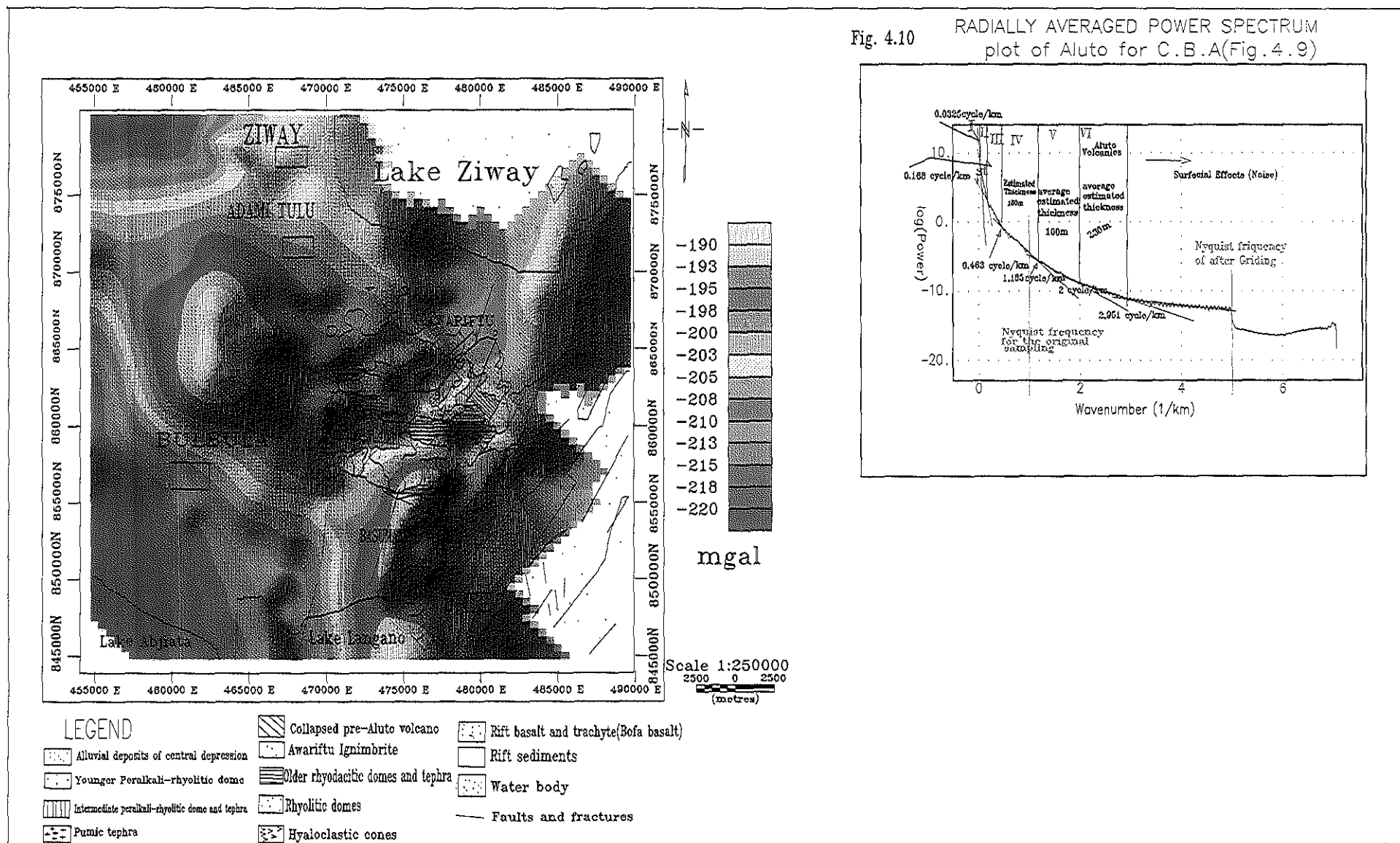


Fig. 4.9 Complete Bouguer anomaly map of Aluto (shaded relief map)

A relatively low anomaly of -210 mgal (as mentioned in the previous map) corresponds to the Awariftu sediments and clastic sedimentary depositions at the southern shore of lake Ziway. At the right margin of the map low Bouguer anomaly is observed that is assumed to be due to the deposition of sediments at the margin of the rift. The southwest part of this map is a region marked by relatively low Bouguer anomaly value that is the response from the main Bulbula and Abijata basin. To make use of this Bouguer gravity anomaly for further interpretation on the depth and location of the geothermal heat sources, the wave number values obtained from the radially averaged power spectrum (Fig 4.10) are: 0.0325cycl/km, 0.168cycl/km, 0.463cycl/km and 1.185 cycl/km, 2cycl/km and 2.95cycl/km are used.

### **The Regional Bouguer Anomaly Maps of Aluto**

The regional anomaly maps (Fig. 4.11, 4.12, 4.13 & 4.14) are produced to show the location of the high-density bodies/intrusions most probably magmatic intrusion that is taken to be the major heat source of the Aluto-Langano geothermal site. The regional gravity anomaly map (Fig 4.11) is found after removing a second-degree polynomial surface trend from the complete Bouguer anomaly map of Aluto (Fig 4.9). This map is similar to that of the regional anomaly map found after applying a low pass filter with cut-off wave number of 0.0325cycl/km (Fig. 4.12). From these maps it can be postulated that a main magmatic intrusion (magmatic reservoir) is found at a depth of 7 to 10km depth whose central location is as shown in the maps. Applying a low pass filter on the complete Bouguer anomaly map of Aluto and using the consecutive short wavelength cut-off wave numbers found from the power spectrum, this magmatic intrusion is found to bifurcate causing Bouguer gravity high at Adami-Tulu and the northern bay of Langano.

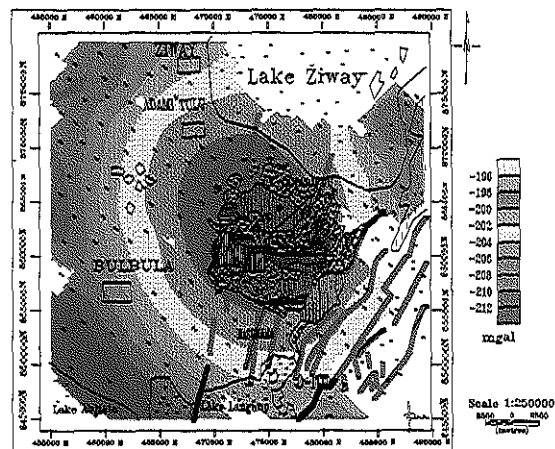


Fig. 4.11 Regional gravity anomaly map of Aluto-geothermal-area after a second degree polynomial surface trend is removed from the C.B.A. map

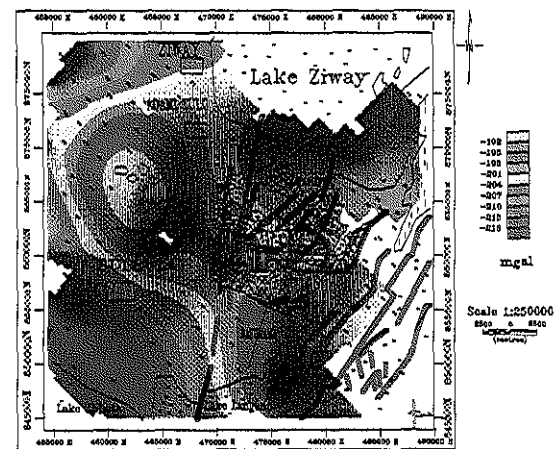


Fig. 4.13 Regional gravity anomaly map of Aluto after a lowpass filter with cut-off wavenumber of 0.08cyl/km is applied

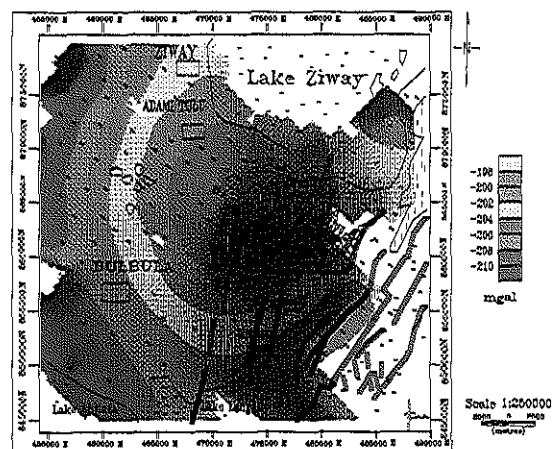


Fig. 4.12 Regional gravity anomaly map of Aluto-geothermal-area after a lowpass filter with out-off wavenumber of 0.0325cyl/km is applied

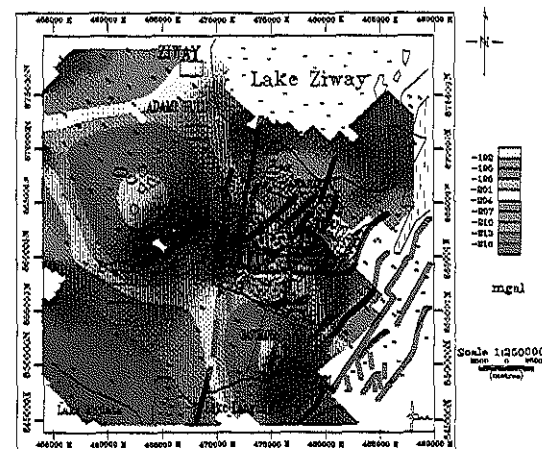


Fig. 4.14 Regional gravity anomaly map of Aluto-geothermal-area after a lowpass filter with out-off wavenumber of 0.09cyl/km is applied

## **The Residual Bouguer Anomaly Maps of Aluto**

The vertical derivatives and band pass filters are employed to produce the residual Bouguer anomaly maps of Aluto. The second vertical derivative map (Fig. 4.16) of the complete Bouguer anomaly map (Fig 4.9) shows a close anomaly pattern as that found by using a band pass filter (Fig 4.18). These anomaly patterns are at an approximate depth of 1-2 km below the surface while what the first derivative map shows is at greater than this depth. Vertical derivative filters enhance shallow anomaly sources. As the degree of derivation increases shallow anomalies will be enhanced more. Hence, the second vertical derivative map shows anomalies at a shallower depth than the first vertical derivative map is expected to show. What is considered here as the deepest gravi-stratigraphic layer is found at an approximate depth of 10 to 15km and has a thickness of 6 to 8km (Fig 4.19); it is expected to host the major magmatic intrusion found under Aluto. The map produced by using cut-off wave numbers of 0.225cycl/km and 0.0325cycl/km shows that this intrusion makes a gravity contrast of about 7 to 9 mgal with the surrounding host rock. At 10 to 15 km depth one expects high-density rocks due to the pressure from the overlaying huge quantity of the crust and this intrusion makes a gravity contrast of 7 to 9 mgal. The next gravi-stratigraphic layer found by applying a band pass filter with cut-off wave numbers 0.0325cycl/km and 0.168cycl/km shows that the intrusion revealed in Fig. 4.19 is divided in two branches. These two intrusions are able to make a gravity contrast of 10 to 15mgal with the surrounding rocks. This gravi-stratigraphic layer is about 5 to 7km thick and is at an approximate depth of 2.5 to 3.5 km. At this depth what is expected is the tertiary ignimbrite (from the well results).

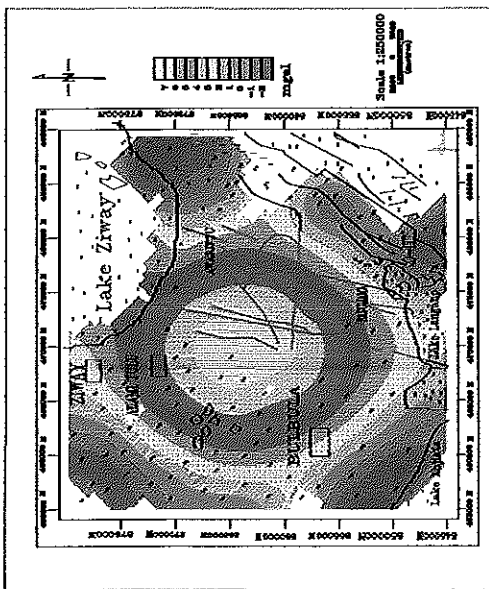


Fig. 4.15 The deepest gravi-stratigraphic layer filtered out by a bandpass filter with boundary out-of wavenumbers 0.0225cy/km and 0.0325cy/km

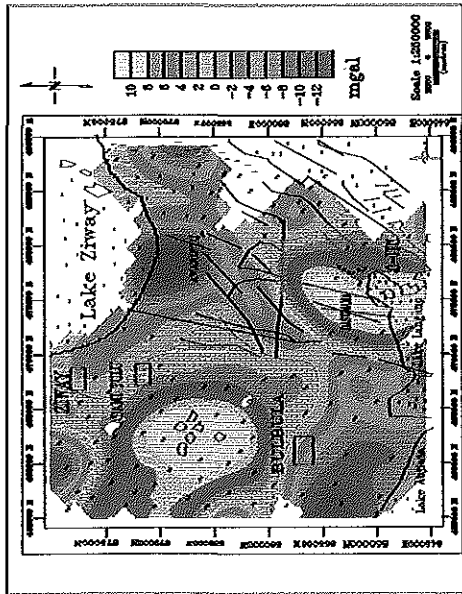


Fig. 4.16 A gravi-stratigraphic layer found by applying a bandpass filter with boundary out-of wavenumbers 0.0325cy/km and 0.168cy/km

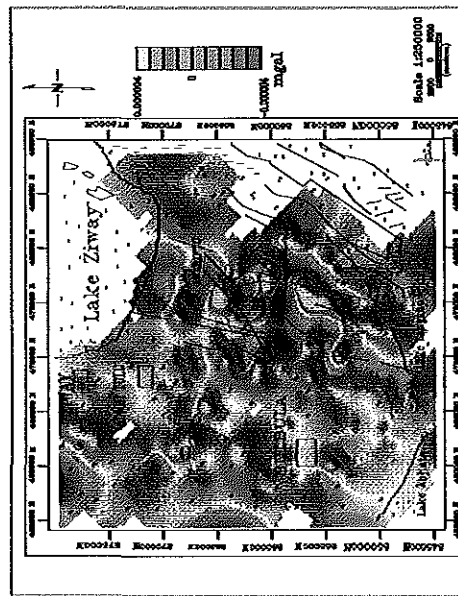


Fig. 4.18 The second vertical derivative map of the Bouguer anomaly of Aluto

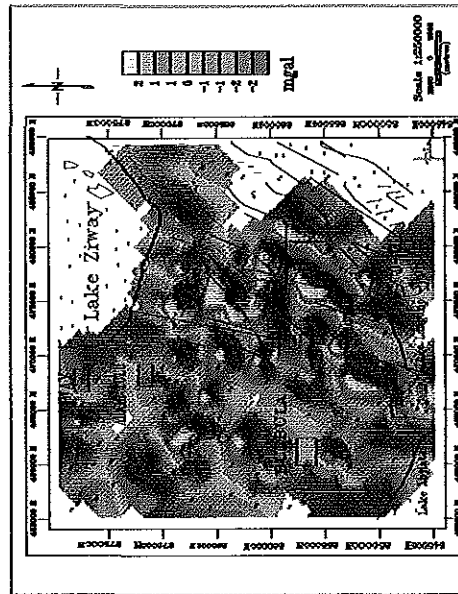


Fig. 4.19 A gravi-stratigraphic layer filtered out by using a band passfilter with boundary out-of wavenumbers of 0.168cy/km and 0.463cy/km

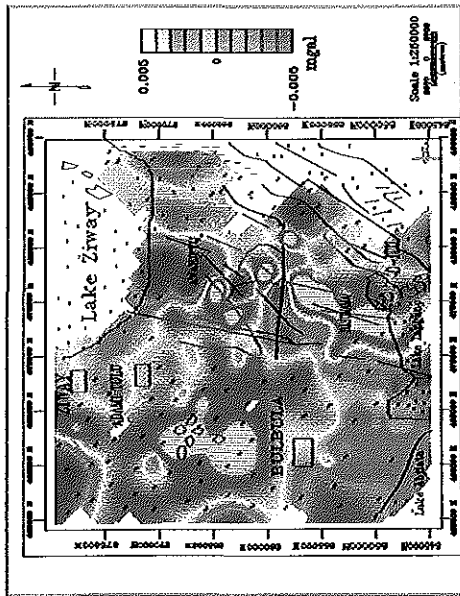


Fig. 4.17 The first vertical derivative map of the Bouguer anomaly of Aluto

How these bifurcated intrusions are further divided can be seen from the first vertical derivative map (Fig 4.15). The gravi-stratigraphic layer (Fig. 4.18) is expected to be 2-3 km thick at a depth of 500 m to few kilometers. From the well data this is within the upper part of the tertiary ignimbrite, the Bofa basalt and the overlying lithologic sequence. The map shows that these scattered anomaly sources make a gravity contrast of 2 to 3mgal with the host rock. These residual maps, in general, show the deep and shallow intrusions that may contribute to the geothermal field of the Aluto-Langano geothermal site.

#### 4.1.2 Quantitative Interpretation of the Gravity Survey

##### Summery of results from the radially averaged power spectrum plots

Lithologic Interfaces	Mean depth	Description	Remak
1	27 -29km	Crust mantle interface	Figure 4.2
2	10-15km	Precambrian basement (?) and Tertiary rocks Interface	Figure 4.2
3	2.5-3.5km	Tertiary ignimbrite and the Bofa basalt interface	Figure 4.10
4	540m*	Bofa Basalt and Huloseyo ignimbrite interface	Figure 4.10
5	330m*	Hulo Seyo and lower lacustrine interface	Figure 4.10
6	230m*	Aluto Volcanics and the underlying layer interface	Figure 4.10

\* Doubtful figures. These values are computed for sampling interval that is beyond the Nyquist wave number for the original sampling; however, the results agree with the well results (ELC, 1986).

Table 4.1. Summery of the results from the Radially Averaged Power Spectrum Plots

To model the crust under the Ethiopian Rift, many scholars have given important suggestions and have done quantitative measurements. It is suggested that the Ethiopian Rift System has

undergone the greatest amount of lithospheric thinning (Roger et al., (1999). The shallowest lithospheric mantle beneath the western shoulder of the Ethiopian Rift is detected at a depth of 40 to 50 km (Roger et al., 1999). On the other hand, beneath the southern rift the lithosphere is thinned up to 50 to 60 km (Roger et al., 1999). The normal continental lithosphere is usually greater than 100km thick (Lowrie, 1997) as compared to 35 to 40 km normal thickness of the continental crust, thus the result that the crust beneath the study area is about 23 km is acceptable due to the fact that the lithosphere that consists of the crust and the upper-solid mantle has undergone tremendous amount of thinning in the Ethiopian Rift.

#### **Estimation of Depth to the Main Magma Chamber under Aluto**

In the absence of any information about the shape of the anomalous body depth to the top surface of the anomalous body can be computed by the formula derived by Bott and Smith (1958) and Smith (1959) (in Telford et al., 1990).

$$\text{Depth to the anomalous mass: } \leq \frac{0.86\Delta g_{\max}}{\left| \frac{\Delta g}{\Delta x} \right|_{\max}} \quad (4.1)$$

where,  $\Delta g_{\max}$  = the pick value of the Bouguer gravity and  $\left| \frac{\Delta g}{\Delta x} \right|_{\max}$  = the maximum gradient of the gravity field. By making use of the regional Bouguer anomaly map of Fig.4.12 it is possible to guess the depth to the top surface of the intrusive body. The maximum gravity anomaly observed in the map is about 10mgal while the maximum gradient found in the NNW-SSE and NNE-SSW directions, respectively are computed as follows

$$\left(\frac{\Delta g}{\Delta x}\right) = \frac{10m\ gal}{8.0645km} = 1.24m\ gal / k \quad \text{and} \quad \left(\frac{\Delta g}{\Delta x}\right) = \frac{10m\ gal}{6.4516km} = 155m\ gal / k$$

Substituting these values in the former equation the results are 8.32 km to 10.4k m depth, which is in agreement with the radially averaged power spectrum results.

### **Gravity Inverse Modeling Using Computers**

The inverse modeling is done using gravity modeling software GM-SYS 3.05G. There are about four profiles selected from the Bouguer anomaly map to produce gravity models. The models are aimed at identifying the main structural units, major lithologic units and volcanic intrusion that contributes to the heat source in the study area. The models are shown in Fig 20 to24

In this study the gravity sampling interval and the degree of accuracy couldn't allow detail modeling of the study area. The gravity modeling taking the well data as constraints (Fig 4.20 and .4.21) results in the identification of geologic contacts but are not able to show definite lithologic layers as clearly as possible. Profile B-B' (Fig. 4.20) is lined in the NNW-SSE on the central part of Aluto and is about 5.5km long while profile C-C' (Fig. 4.21) is in the E-W direction on the center of Aluto and is about 11km long. On the other hand, the gravity models produced by giving the radially averaged power spectrum as initial model parameters (Fig4.19 and Fig.4.20) couldn't show geologic contacts and faults. The reason is that the faults that cross the selected profile could not make appreciable lateral density variation. Moreover, it is not possible to compare the results of the gravity models to that of the resistivity is the case of profile C-C' and profile D-D' because the data sampling the gravity

survey is more for regional structures and lithologic layers than that of the resistivity. The gravity models (Fig. 4.20, 4.21, 4.22, 4.23) presented here are modeled just by giving the power spectrum result as initial parameters and the initial density parameters: 2.8 gm/cm<sup>3</sup> for the deepest layer, 2.6, 2.4 and 2.2 gm/cm<sup>3</sup> for the top layers. Since there is no density information depth wise this is found fair to assign the density of the crust increasing with depth. In general terms, the models show high-density materials intruding in to the near surfaces.

Profile E-E (Fig. 4.22) is about 7km long across the intrusive body south of Aluto. This gravity profile data is modeled to see the depth and orientation of the intrusive body that causes relatively high-gravity value. Accordingly, it is seen to intrude in two branches reaching up to 1 to 1.5km of depth. More over it shows the shape of the various layers identified by the power spectrum results. Where as, profile F-F (Fig. 4.23) is the longest profile that has a length of about 40km that is lined in the NW-SE direction across the Adami-Tulu and North Langano gravity highs. This gravity profile data is modeled to hunt both major structural contacts and the intrusive bodies that cause the gravity highs. This model succeeds to find about two significant faults one from the eastern escarpment and the other from the western margin of the Aluto.

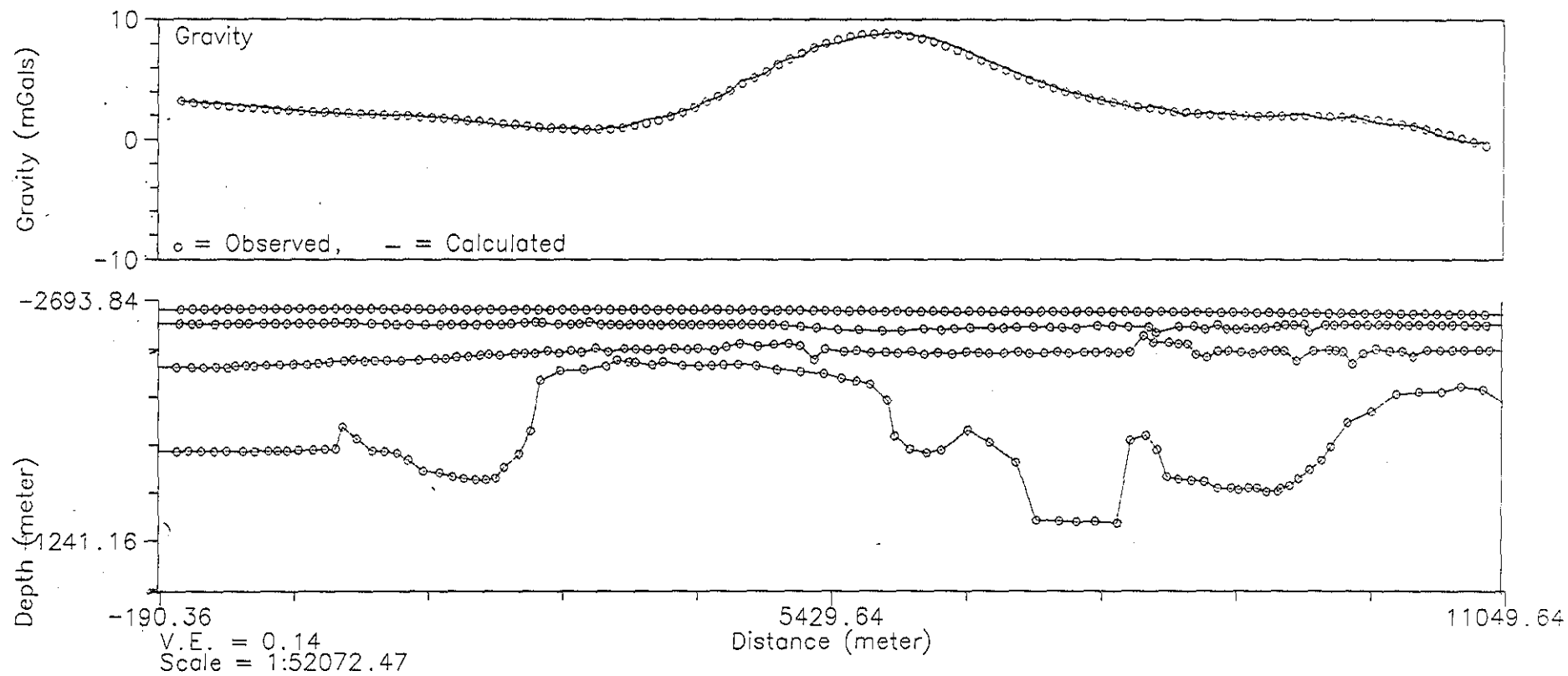


Fig. 4.20 Gravity model along profile D-D'

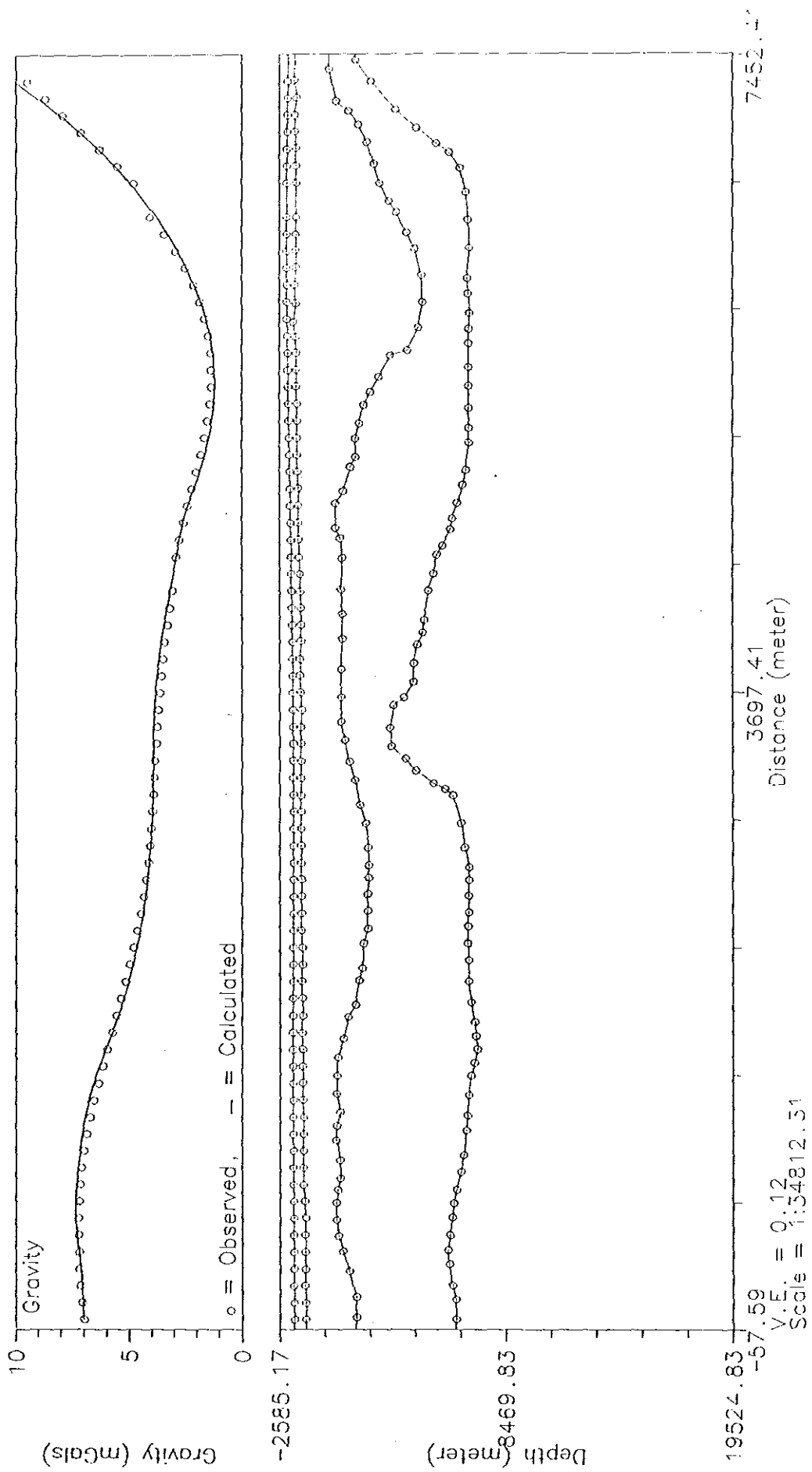


Fig. 4.21 Gravity model along profile C-C'

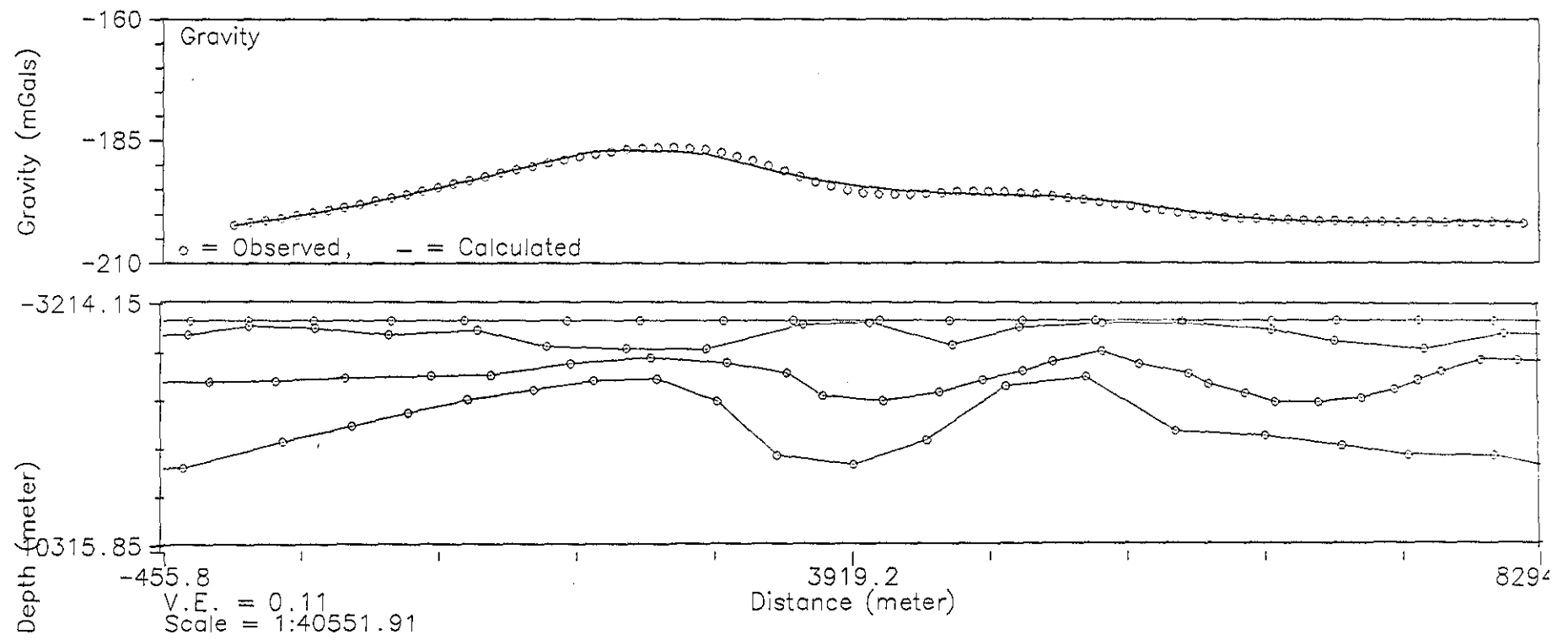


Fig 4.22 Gravity Model along profile E-E'

## 4.2. RESULTS AND INTERPRETATION OF RESISTIVITY SOUNDING

It is evident from the numerous reports and case histories in geothermal energy explorations that electrical resistivity method gives very useful information on:

- A. The depth, thickness and size of the aquifer and aquicludes,
- B. Porosity of rocks/porous zones such as fractured zones,
- C. Ionic contents of fluids and temperature in the case of hydrothermal fluid circulations and hydrothermally altered zones (Willie, 1963; Keller and Fisknecht, 1966; Dakhove, 1962; Ward Fraser, 1967; Keller, 1970; Zohdy et al., 1973; Dupret, 1987)

In this thesis work qualitative and quantitative interpretations on the major anomalies are given to the resistivity maps, to the Psuedosection and to the geoelectric sections.

### 4.2.1 Qualitative Interpretation of the Resistivity Data

#### **Apparent Resistivity Map at $AB/2 = 10\text{m}$**

The apparent resistivity map at  $AB/2 = 10\text{ m}$  (Fig 4.24) is expected to show the response from about 4 to 7m depth. Except on the northern part of Aluto, around fumaroles and sedimentary deposits on the top of the mountain all the Aluto volcanics at very shallow depth exhibit relatively high resistivity values. The apparent resistivity values, in general vary from less than  $50\ \Omega\text{m}$  to a maximum value of  $4000\ \Omega\text{m}$ . The relatively high resistivity values form a belt in the east west direction mostly focusing at the young peralkali-rhyolitic flows. This is due to low intensity of weathering on the young products of the Aluto volcanics. The glassy pumice and obsidian found abundant over the study area are dry and resistive, contributing to the high resistivity values observed. The relatively low resistive regions are found in between

Aluto and lake Langano that may be due to the rift sediment in between north of Langano and the southern foot of Aluto. On the summit of the mountain low resistive region is observed with 100 to 400 $\Omega$ m that is found to correspond to the positions of the fumaroles and where the alluvial deposit of central depression is located. The low resistive zone with resistivity value less than 100 $\Omega$ m at the northern part of the map indicates relatively weathered and moist ground.

#### **Apparent Resistivity Map at $AB/2 = 100$ m**

This (Fig. 4.25) apparent resistivity map is expected to show the apparent resistivity distribution at a depth of about 50 to 70m below the surface. At this depth what is found up to this depth is the Aluto volcanics (from the well results). At this level the apparent resistivity values range from less than 50 $\Omega$ m to 700 $\Omega$ m indicating that there is a decrease in the resistivity with depth. ELC (1986), has pointed out the existence of a shallow aquifer at a very shallow depth and T/Mariam et al, (1996) has shown the lateral outflow of hydrothermal fluids at a shallow depth. Though the depth can be deeper than the depth this map is expected to show, the effect of this shallow aquifer and the heat from the hydrothermal fluid circulation can affect the resistivity of this zone better than a very shallow depth of investigation by the  $AB/2=10$ m depth discussed above. Here all the resistive regions are found to correspond to the location of intermediate peralkali-rhyolite and tephra and all relatively very low regions on the central part of Aluto are found to correspond to the position of the fumaroles. The high resistive layer in this map seems to follow the fault line that crosses the mountain. Low resistivity zone south of this map and its continuation to the west is interpreted to be the effect of the rift sediments found at north of Langano.

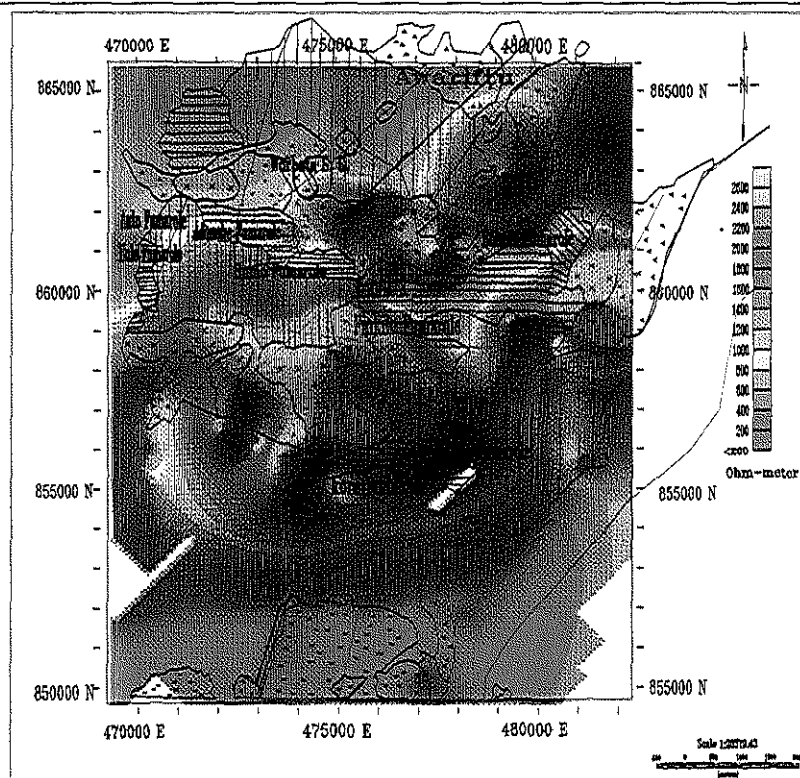


Fig. 4.24 Apparent resistivity map of Aluto-geothermal-area.  $AB/2 = 10m$

Prepared by Tibebe Ayale. January, 2001

pu

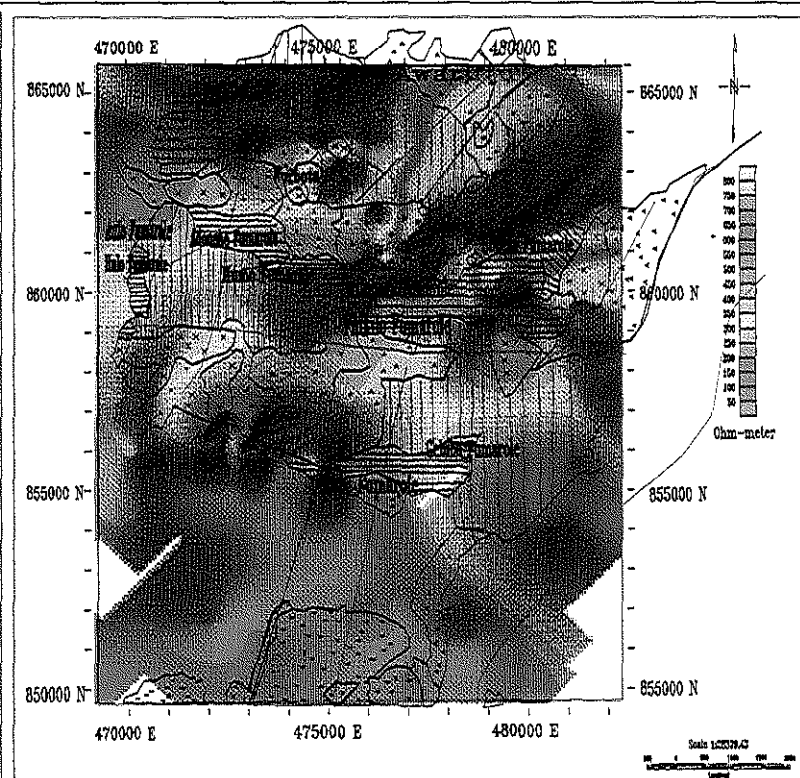


Fig. 4.25 Apparent resistivity map of Aluto-geothermal-area.  $AB/2 = 100m$

Prepared by Tibebe Ayale. January, 2001

pu

## LEGEND

- |  |                                    |                                       |
|--|------------------------------------|---------------------------------------|
| Alluvial deposits of central depression          | Collapsed pre-Aluto volcano        | Rift basalt and trachyte(Bofa basalt) |
| Younger Peralkali-rhyolitic dome                 | Awariftu Ignimbrite                | Rift sediments                        |
| Intermediate peralkali-rhyolitic dome and tephra | Older rhyodacitic domes and tephra | Water body                            |
| Pumic tephra                                     | Rhyolitic domes                    | Faults and fractures                  |
|  | Hyaloclastic cones                 | S.G =steaming ground                  |

### **Apparent Resistivity Map at AB/2= 1000m**

This (Fig. 4. 26) map reflects that the resistivity of the ground still decreases with depth. Here, the apparent resistivity value varies from a minimum of less than  $5\Omega\text{m}$  to over  $65\Omega\text{m}$ . The map is expected to show the resistivity distribution at a depth of 400m to 700m. This is a depth where pyroclastic and sedimentary units are found. Sedimentary units and poorly cemented pyroclastic rocks permit fluid flow. Generally, very conductive zones are located at the sites of the fumaroles and the rift sediments. A relatively high apparent resistivity reaching to 40-  $50\Omega\text{m}$  is found forming a belt in the NNW to SSE direction.

### **Apparent Resistivity Map At AB/2=2150m**

In this map (Fig. 4.27) the apparent resistivity values range from a positive possible minimum value to  $40\Omega\text{m}$ . This is a zone that is expected to reach to a depth of 900m to 1500m. This is the average depth of the Bofa basalt that underlies the various sequences of pyroclastic and sedimentary sequences. Here, the temperature is over  $200^{\circ}\text{C}$  (from the well results). Except the east west belt of relatively high apparent resistivity values (not greater than  $40\Omega\text{m}$ ), all region shows very low resistivity. This region is highly affected by the hydrothermal fluids and the associated thermal heat flow. This is the most expected productive zone from which geothermal heat source can be taped.

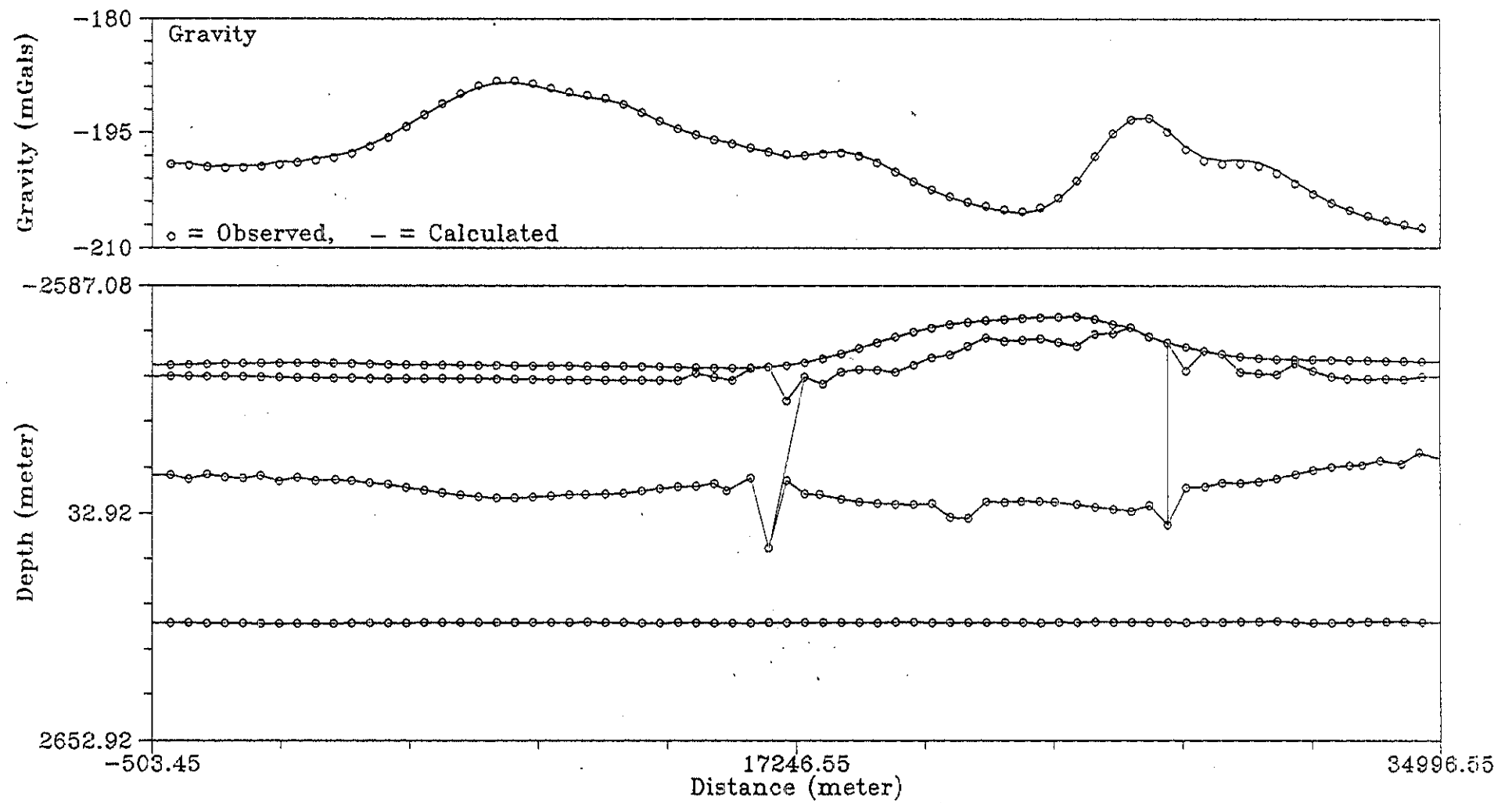


Fig. 4.23 Gravity model along profile F-F'

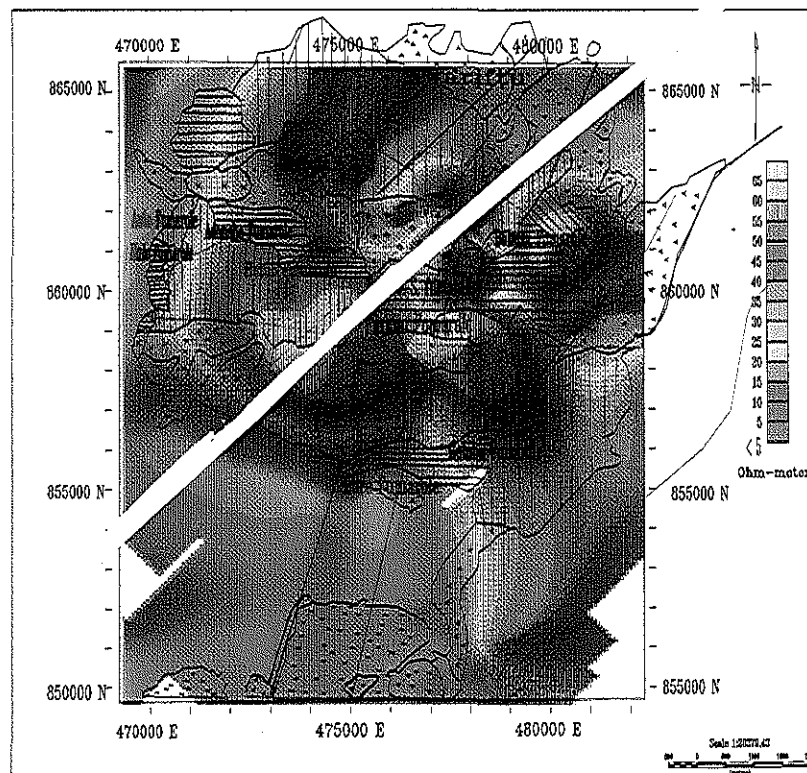


Fig. 4.26 Apparent resistivity map of Aluto-geothermal-area.  $AB/2 = 1000m$

Prepared by Tibebe Ayele, January, 2001

Tbe

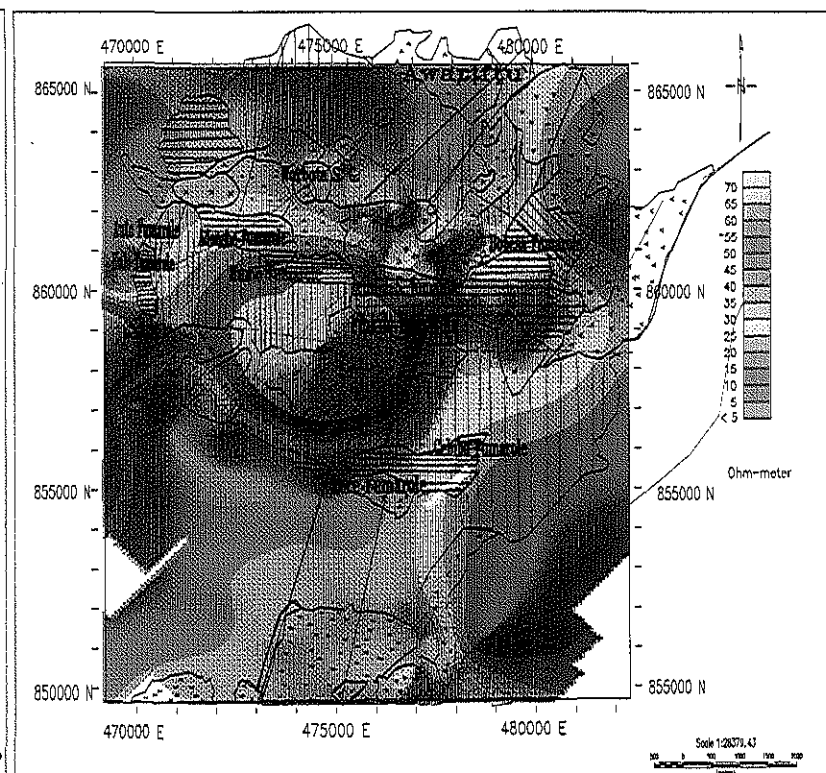


Fig. 4.27 Apparent resistivity map of Aluto-geothermal-area.  $AB/2 = 2150m$

Prepared by Tibebe Ayele, January, 2001

Tbe

## LEGEND

- Alluvial deposits of central depression
- Younger Peralkali-rhyolitic dome
- Intermediate peralkali-rhyolitic dome and tephra
- Pumic tephra

- Collapsed pre-Aluto volcano
- Awariftu Ignimbrite
- Older rhyodacitic domes and tephra
- Rhyolitic domes
- Hyaloclastic cones

- Rift basalt and trachyte(Bofa basalt)
- Rift sediments
- Faults and fractures
- S.G = steaming ground

## 4.2.2 Quantitative Interpretation of the Resistivity Data

### Profile A-A'

The apparent resistivity pseudosection (Fig.4.28b) shows the distribution of apparent resistivity values from a maximum of 2100Ωm at the surface to a minimum of 25Ωm at depth. The upper part of this section is characterized by relatively high apparent resistivity and followed by low resistive zone. The most resistive portion between VES 1 and VES 3 is probably due to dry volcanics. Adjacent to this section is a low resistive small section that corresponds to the location of Auto fumaroles. The rest of the top layer parts are marked by intermediate resistivity. The succeeding layer is marked by very low resistivity. The geoelectric section of this profile shows about four geoelectric layers: top resistive layer with resistivity values ranging from 300Ωm to 1300Ωm, a second resistive layer that finally fades and dies out to the left. It is marked by a resistivity value of 200-300Ωm, a third very conductive region with resistivity 2-10 Ωm and a low resistive bottom layer. It identifies no geologic contact or fault but a low resistivity doming up around VES 4. The conductive zone is found relatively shallower depth of 100 to 200 meters down from the surface and has a thickness of about 100 to 600m.

### Profile B-B'

This profile crosses Aluto from the NNW direction to the SSE. There are 9 VES points in the same profile, in a distance of 5.5 Km. It is the best of all the other profiles in terms of station density and orientation of the profile. In the geoelectric section (Fig 4.29c) and the pseudosection (Fig. 4.29b) about three weak zones are identified.

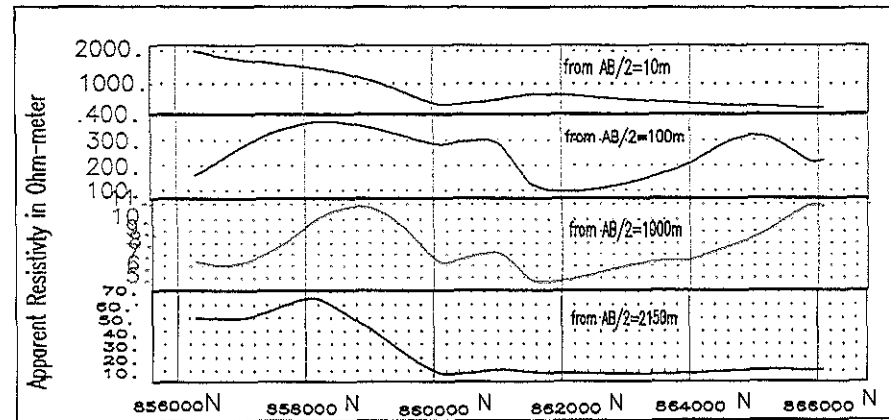


Fig. 4.28a Apparent resistivity profile plots along A-a'

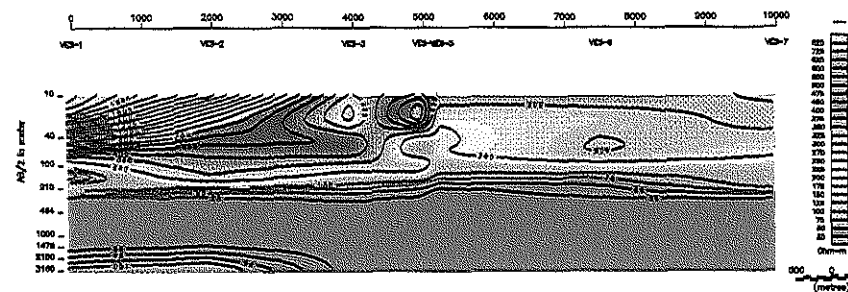


Fig. 4.28b Apparent resistivity pseudosection of profile A-A'

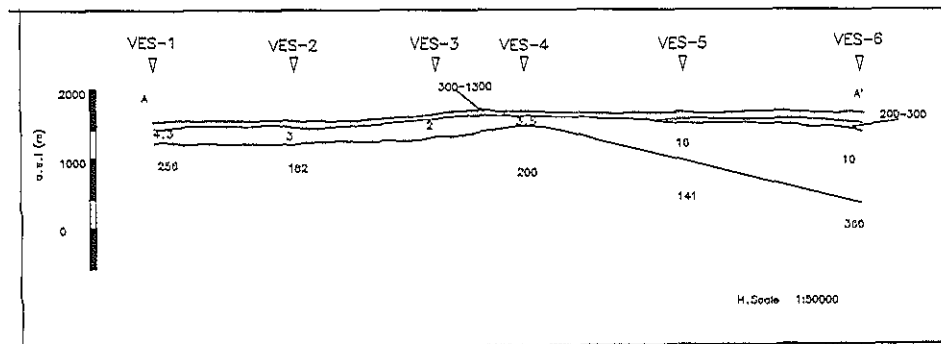


Fig. 2.28c Geoelectric section along pforile A-A'

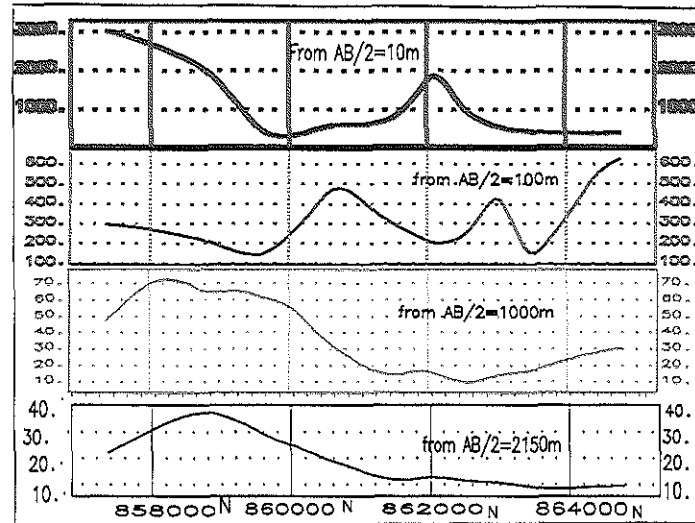


Fig. 4.29a Apparent resistivity profile plots

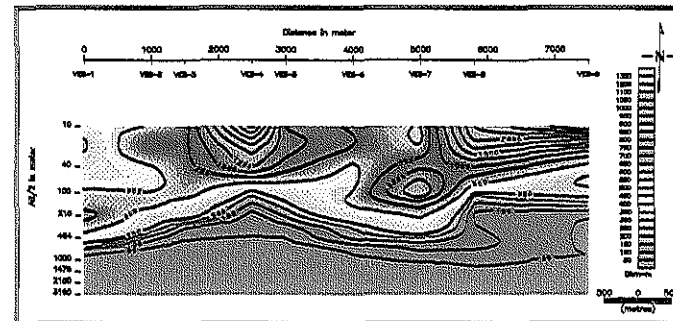


Fig. 4.29b Apparent resistivity pseudosection along profile B-B'

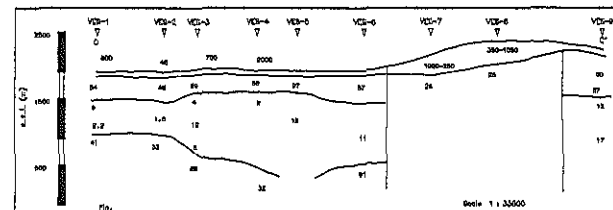


Fig. 4.29c Geoelectric section along profile B-B'

The gravity model (Fig. 4.19a) also shows these weak zones. These weak zones are marked by lateral resistivity changes. In the psuedosection (Fig. 4.29b) a relatively high resistive layer is seen to be the response from Aluto's young and old rhyolite, except in places where fumaroles are around. Other than this top resistive layer, the section shows decrease in resistivity with depth. The geoelectric section (Fig 4.29c) shows top thin resistive layer of resistivity 300 $\Omega$ m to 4000  $\Omega$ m having thickness about 70 to 150 meters are followed by an intermediately resistive layer of resistivity between 50 $\Omega$ m to 250 $\Omega$ m. Next to this layer, the resistivity drops to a very low value of 1.6-16 $\Omega$ m showing that this region is very conductive and highly affected by hydrothermal fluids. At about VES-8 there is a doming structure that corresponds to the older rhyodacitic dome and tephra in the geologic map.

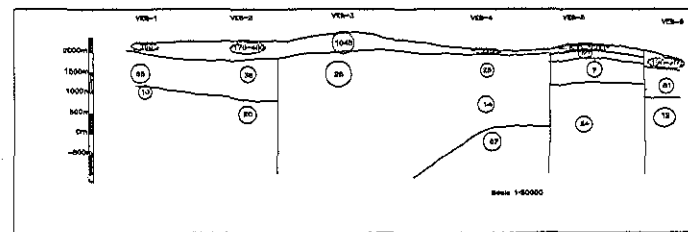
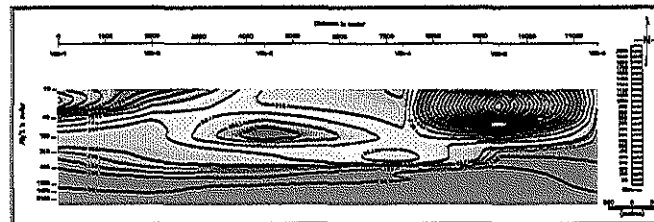
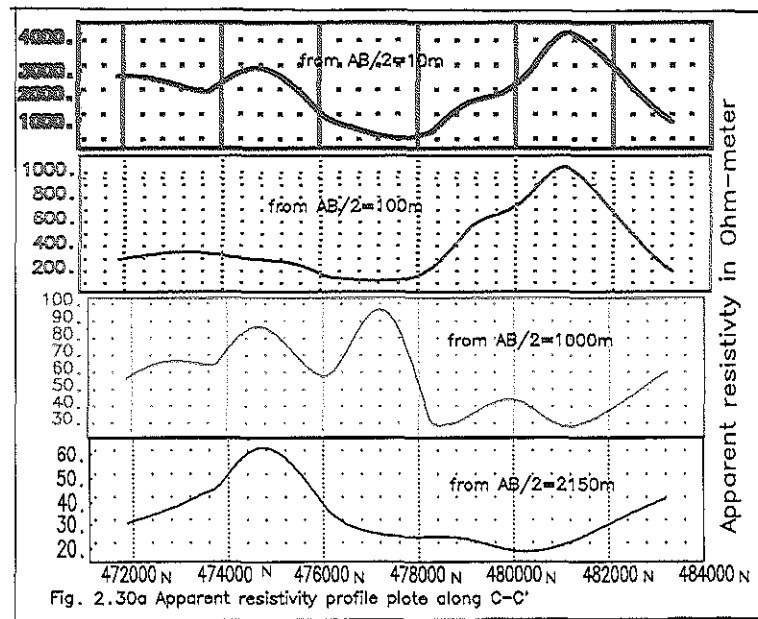
#### **Profile C-C'**

This profile crosses Aluto from east to west. It shows about three weak zones and a dome at VES-5 The psuedosection (Fig 4.30b) along this profile shows distinct pockets of resistive regions. In general the top resistive layer corresponds to the Aluto volcanics. In this top layer a more resistive regions at either corners correspond to the dry and resistive intermediate peralkali-rhyolite. There is also a very resistive pocket of layer beneath VES-3 whose causative body may be a very localized dry and resistive region. This psuedosection also shows a relatively low resistive region on the top surfaces at the location of Finkilo Fumaroles. The succeeding zone is highly conductive that corresponds to the lower lacustrine sediments and the upper part of the weathered and fractured part of the Bofa basalt. The geoelectric section identifies about three structurally weak zones/probably fault/ and a domed structure just around VES-5. The top resistive layer has a resistivity ranging from 170 to

3000 $\Omega$ m while the succeeding layers have very low resistivity. This geoelectric section shows that all the underlying layers below the first top layer are very conductive. From the very low resistivity nature of the layers it can be concluded that there is intense hydrothermal alterations.

#### **Profile D-D'**

This profile consists of four VES points and is along the eastern margin of Aluto. As the pseudosection (Fig 4.31b) of this profile shows, the top layer is relatively resistive. In the upper part of this layer there is a relatively high resistive portion observed at the left of the profile with apparent resistivity of 750 $\Omega$ m. In the same stratum going to the right along this profile the resistivity drops to about 200 $\Omega$ m probably due to lacustrine siltstone, sandstone and interbedded tuff predominantly rhyolite adjacent to the eastern margin of Aluto. Going from left to the right of this profile there is a sharp gradient of contours showing a dome (the profile passes across the intermediate peralkali rhyolitic dome). The underlying stratum appears to be more conductive than the overlying layer. From the well data this corresponds to the Gadamotta pyroclastic, the older lacustrine sediments and probably the upper part of the Bofa basalt. The geoelectric section reveals three layers: a relatively resistive top layer with resistivity range between 125-875 $\Omega$ m, a second layer with resistivity 37-55 $\Omega$ m and a bottom layer with resistivity less than the others. The last two layers show small resistivity variation with each other. Generally, the resistivity in this section varies with depth. The description of the geoelectric layers is similar with that given in the pseudosection of this profile.



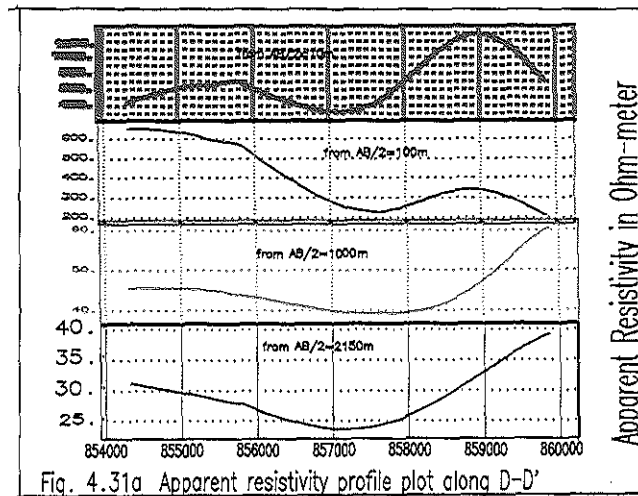


Fig. 4.31a Apparent resistivity profile plot along D-D'

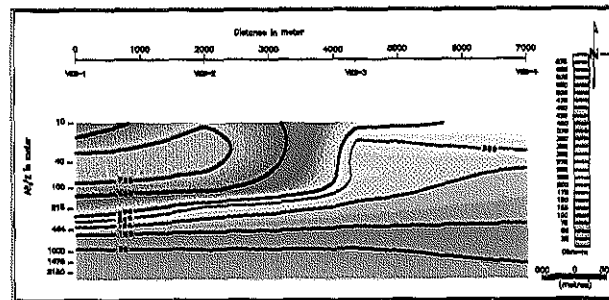


Fig. 4.31b Apparent resistivity pseudosection along profile D-D'

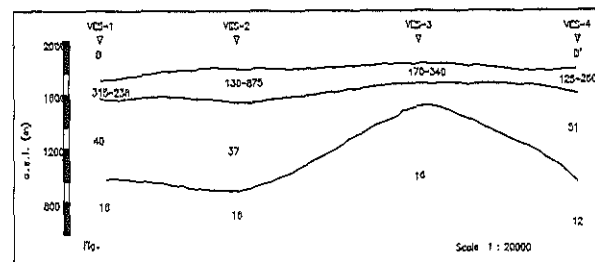


Fig. 4.31c Geoelectric section along profile D-D'

### 4.3 COMBINED INTERPRETATION AND ZONAL CLASSIFICATION

Figs 4.32a and 4.32b demonstrate the association between resistivity and gravity responses of the Aluto geothermal area at an estimated depth of 2 to 3km. The maps illustrate sporadic maximum and minimum values of the gravity and resistivity values. Nearly all gravity positives in the map are evidently related to faults and fractures (Fig. 4.32C) mapped on the surface; where as, resistivity maximums do not show much correlation with structural settings (except to that of the east west fault in the center of Aluto, considered to be the up flow zone). At this depth a single or at most two lithologic units are anticipated; explicitly, the Bofa basalt and the Tertiary ignimbrite. The resistivity map display anomaly values ranging up to 40 Ohmmeter; the gravi-stratigraphic unit also exhibit gravity values ranging from negative 4 mgal to positive 4 mgal signifying that there is definite lateral disparity of physical properties in the lithologic unit that is certainly caused by heat, hydrothermal fluids, hydrothermal alterations, porosity and intrusive bodies. Anchored in this observation geothermal wells are proposed in section (5.2.2).

The Tertiary ignimbrite and the Bofa basalt are the two branded lithologic successions exceedingly influenced by hydrothermal alterations due to up flow and lateral outflow of hydrothermal fluids. The Bofa basalt demonstrates prominent veins and amygdales filled by secondary minerals (TekleMariam, 1996).

Gravity and resistivity anomalies can be associated with densification of host rock, hydrothermal mineral depositions in fractures (Marshet, 1983 in Befekadue et al, 1983), mafic intrusive bodies (Johnstone, 1982 in Befekadue et al, 1983) or/and exchange of hydrothermal

minerals by hydrothermal fluids, porosity and temperature. Two types of hydrothermal alterations are detected in the Aluto-Langano geothermal area: propylitic and argillic (Teklemariam, 1996).

The former one is found in the up flow zone with high temperature reaching up to 335°C. It is characterized by the presence of epidote, calcite, garnet, quartz and chlorite (Teklemariam, 1996). Most of these minerals are characterized by high density and high resistivity physical properties (Telford, 1990). Conversely, the later one is characterized by calcite and clay alteration that is found in the lateral outflow of the hydrothermal fluid mostly confined to the Bofa and tertiary ignimbrite Teklemariam, (1996). Clay in general is characterized by low density and low resistivity physical properties (Telford, 1990).

Based on this postulation, promising zones can be mapped using the integrated gravity and resistivity outcome on this most likely productive zone. Here, relatively low-resistivity and high-density zones are assumed to be more productive. The rationale in selecting most geothermal prospective zone as high-density and low-resistivity is that high-density is interrelated to intrusive bodies and active alteration zones (metamorphism takes place where it is associated with high temperature and high fluid enthalpy); while low resistivity regions are associated with high temperature, circulating hot fluids, porous zones filled with fluids.

Based on the above assumption the study region is zoned as I, II, III, IV and V, in decreasing order of expected productivity.

(Fig. 4.18)

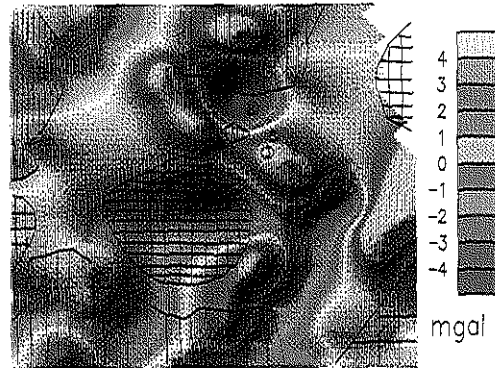
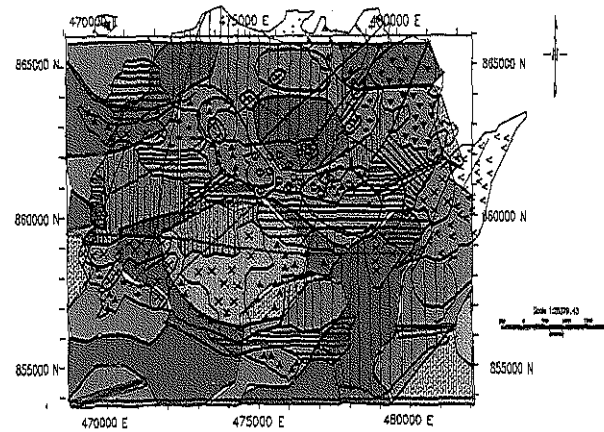


( Fig. 4.27)



- I Relatively very high gravity ( $> 3$  mgal)  
Relatively very low resistivity ( $< 10$  Ohmmeter)
- II Relatively high gravity ( $1-4$  mgal)  
Relatively low resistivity ( $10-40$  Ohmmeter)
- III Relatively Very low gravity ( $< -2$  mgal)  
Relatively very low Resistivity ( $< 10$  Ohmmeter)
- IV Relatively Very high resistivity ( $> 30$  Ohmmeter)  
Relatively low gravity ( $-2$  to  $2$  mgal)
- V Relatively very high resistivity ( $> 30$  Ohmmeter)  
Relatively very low gravity ( $< -2$ mgal)

Fig.4.32 Zonal classification of Gravity and Resistivity anomalies

## CHAPTER V

### DISCUSSION, SUMMERY AND RECOMMENDATIONS

#### 5.1 SUMMERY OF RESULTS

The apparent resistivity maps, psuedosection and geoelectric sections illustrate:

- A. The resistivity of the ground decreases with depth,
- B. High conductive zone is seen below an average depth of 300m,
- C. Due to the relatively highly resistive anomalous zone that formed an E-W belt in all the maps the ground water flow from Ziway (1625m) to Langan (1586m) through Aluto seems doubtful. This implies that the hydrothermal fluids flow through the NNE to SSW faults is blocked by the E-W faults. This has another implications that the northern and the southern parts form separate geothermal systems. This is in agreement with what is proposed by the EIGS, (1983)

The gravity data analysis results show:

- A. The crust is divided in to three major grai-stratigraphy layers:
  - 1. The Basement Complex (15 to 19 km thick),
  - 2. The Tertiary Basalts and (5 to 7km thick),
  - 3. Recent sediments and silic volcanic products (less than 3 km thick).
  - 4. The average thickness of the crust is estimated to be around 28 km.

It must be taken into account that this major classification obviously disregards thin sedimentary lineaments that may be found between these major units. Moreover, the

Precambrian basement that assigned to the deepest unit is expected to be perforated magmatic and basaltic intrusions.

- B. The main spreading zone has a width of 20 to 80 km at a depth greater than 10 km and follows the WFB surface alignment direction.
- C. Major deep heat source at a depth below 7 km are mapped and are interpreted as magmatic intrusions. These intrusions are at Shala and under Aluto.

## **5.2 THE ORIGINALITY OF THE STUDY AND NEW RESULTS.**

In no other related study in the same region (within the reach of the author) has tried to show the following outcomes quantitatively.

- A. The thickness of the crust in this part of the rift.
- B. The major lithologic layer below a depth exceeding 2km (depth of the deep geothermal well at Aluto) and the average thickness of the lithologic units.
- C. Mapping of the lateral extent and width of the spreading zone at a depth below 7 km and major structural units at a depth of 3 to 5 km.
- D. Mapping of intrusive bodies at various depths, the magma chamber and its further branching at shallow depths as well as many sporadic intrusions that contribute to the geothermal heat source for the study area.
- E. Structurally weak zones are delineated by the resistivity interpretation.

## **5.3 LIMITATIONS OF THE SURVEY**

The geophysical techniques engaged here are effective for depth investigation. The electrical

resistivity data with maximum electrode spacing  $AB = 6300$  m has appreciable depth of penetration that reaches up to 2km depth. Yet, topographic corrections for this data could not be done due to lack of appropriate software, implying that the resistivity interpretations have minor limitations. In contrast, the gravity data sampling interval and the accuracy level hampered shallow mapping of anomalies up to the depth of few tens of meters. In both the surveys the sampling intervals were not contemplated.

### **5.3 RECOMMENDATION**

#### **5.3.1 Recommendation to Further Strengthen the Results of this Study.**

Based on the investigations made in this study geophysical methods are recommended for a further detail study of the problem and locate the site for better exploratory wells.

- A. A detail resistivity survey with VES point separation in a few tens of meters using very sensitive devices and avoiding topographic effects helps to precisely map the resistivity distribution of the subsurface. This can help to trace minor fractures and structurally weak zones that are possible channels for hydrothermal fluids to flow through.
- B. A detail gravity survey with station separation in few tens of meters. Fixed bench marks on the summit of the Aluto, at the north and southern foots of the mountain and on the northern end of Langano to monitor the net mass transfer due to the net withdrawal of hydrothermal fluid. This can help to monitor the extractable geothermal energy quantity.
- C. A detail magnetic survey helps to assess the hydrothermal deposits of the study

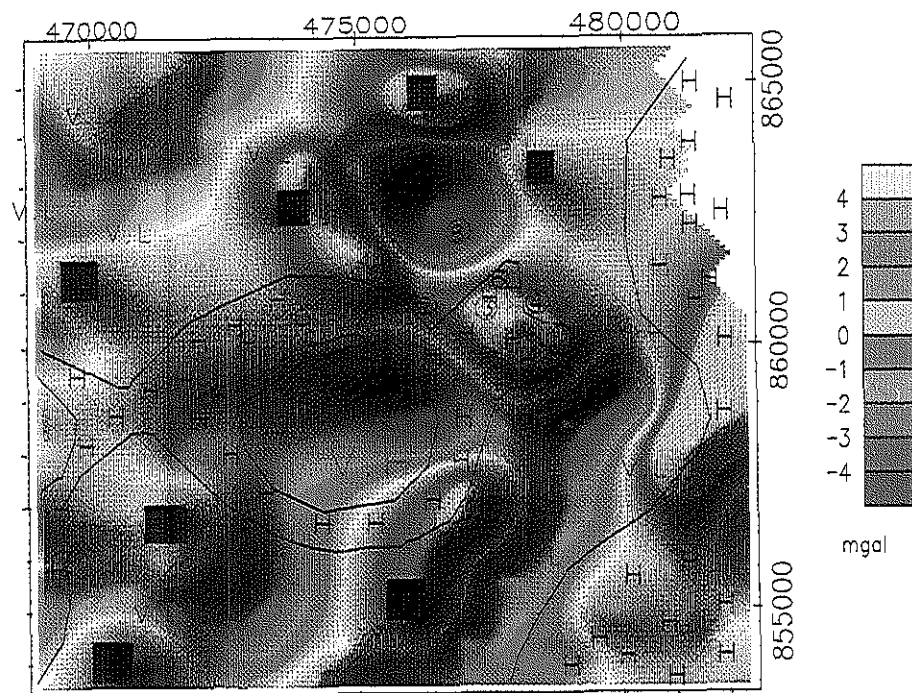
area and further verify the depth estimations made using the gravity method.

- D. Seismic reflection is compulsory to identify structures, study densities of rocks at various depths and for a precise determination of depth to the magma chamber, provided that the natural earthquake does not noise the signal of the artificial seismic wave.
- E. A magneto telluric method is recommended to study the electrical nature of the deep-seated rock units.

### **5.3.2 Recommendation to test wells.**

Best recommendations are instituted by appropriately evaluating all the geophysical, geochemical and hydrological information. However, it is legal to recommend productive wells based on this study. The recommended wells can later be strengthened by the recommended geophysical methods.

The anticipated wells are sited at regions where the resistivity is low and the density is relatively high with the supposition that gravity high is linked to intrusive bodies, densification of host rock by alteration minerals in the up flow zone together with resistivity low that are thought to be associated to thermal-zones with circulating fluids and porous regions filled with fluids. A test well for temperature log preceded by geothermal wells is what is proposed in this recommendation.



## LEGEND

H = High i.e., between 10 and 40 Ohmmeter

V.L = Very Low i.e., < 10 Ohmmeter

V.H = Very high i.e., > 40 Ohmmeter

○ = Previous well sites

■ Proposed Geothermal wells

Fig. 5.1 Sites for future Geothermal wells

## REFERENCES

- Abebe, T., Mazzarini, F., Innocenti, F. & Manetti, P.(1998):** The Yerer-Tullu Wellel volcanotectonic lineament: a transtensional structure in central Ethiopia and the associated magmatic activity. *J. Afr. Earth Sci.*, 26, 135-150.
- Agocs, W.B., (1951):** Least- Squares residual anomaly determination. *Geophysics* 16
- Alula, A., et al., (1992):** Geological Map of the Nazaeret- Dera region ( Main Ethiopian Rift ) 1: 50,000 scale , Ministero degli Esteri, Consiglio Nazionale delle Ricerche, S.El. CA , Firenze , Italy ,1992
- Asfaha, W.,(1990):** Processing and interprtaion of gravity and aeromagnetic data. Gambel, SW Ethiopia. Msc. Theisis. Department of Earth Resources Survey. ITC.
- Baker, B.H, Mohr, P.A. and Williams, L.A.J., (1972):** Geology of the East Rift System of Africa. *Geol. Soc. Am., Spec. Paper.*, 136:67pp.
- Barberio, M. R., Donato, P., Yirgu, G., Peccerillo, A., Wu, T.W (1999):** Petrology and Geochemistry of Quaternary magmatism in the northern sector of the Ethiopian Rift between Debrezeit and Awash park. *Acta. Volcano. Vol. II(I)* 69-81
- Befelkadu O., Abiy, H., & Ketsela (1983):** Geophysical Survey in the Aluto - Langano Geothermal field.
- Bhattacheryya, B.K., (1964):** Magnetic anomalies due to prism- shaped bodies with arbitrary polarization. *Geophysics* 29. Pp 17-31
- Boccaletti, M., Bonini.M., Mazzuoli.R., Trua,T. (1999):** Pliocene-Quaternary volcanism and faulting in the northern Main Ethiopian Rift. *Acta Vulca. VolIII(1)* Pp:83-97
- Boccaletti,M., Mammo.T., Bonini,M. &Abebe, B., (1994):**Seismotectonics of East African rift System: Evidences of active oblique rifting. *Ann. Tectonicae*, 8, 87-99.

**Boccaletti, M., Getaneh, A., Mazzuoli, R., Tortorici, L. & Trua, T. (1995):** Chemical variation in a bimodal magma system: the Plio-Quaternary volcanism in the Dera Nazereth area. *Afr. Geosci. Rev.*, 2, 37-60

**Boccelethi, M., Getaneh, A. & Tortorici, L. (1992):** The Main Ethiopian Rift: an example of Oblique rifting. *Ann. Tectonica*, 6, 20-25

**Boccaletti, N., Bonini, M., Mazzuoli, R., Abebe, B., Poiccardi, L. & Tortorici, L. (1998):** Quaternary Oblique extensional tectonics in the Ethiopian Rift. *Tectonophysics*. 287, 97-116

**Childers, V.A., Bell, R.E., and Brozene, J.M., (1999):** Airborne gravity : An investigation of filtering. Appx.. Determining the smallest observable anomaly. *Geophysics*. Vol. 64 Pp. 68-69.

**Chorowicz, J., Collet, B., Bonovia, F., Korme, T., 1994.** NW to NNW Extention direction in the Ethiopian Rift deduced from the orientation of extention structures and fault-slip analysis. *Geol. Soc. Am. Bull.* 105, 1560-1570.

**Chorowicz, J., Le Fourier, J. & Vidal, G. (1987):** A model for rift development in the East Afric. *Geol. J.*, 22, 494-513

**Coblentz, D.P. & Sandiford, M. (1994):** Tectonic Stress in the African Plate: Constrains on the ambient lithospheric stress state. *Geology*, 22, 831-834

**Corrado, D.I., & Keller, G.R., (1981):** The Gravity field of Italy: Analysis of its spectral composition and delineation of a tridimensional crustal model for Central - Southern Italy. *Geofis. Bul.*, Vol. XXIII, N.89

**Doser, D.I., & Keller, G.R. (1999):** Seismicity of the East African Rift and its relation to Rift Development. *Acta. Volcanologica*-, Vol. II(I)-43-51

- Dakhnov V. N. 1962.** Geophysical well logging. Quart. Colo. Sch. Min., 57.
- Di Paola, G.M., (1972):** The Ethiopian Rift Valley ( between 7° and 8° oo' lat. North. Bull.Vulcan.,36. 517-560.
- Di Paola, G.M., and Berhe, S., (1979):** The Kella Horest: A hithero unknowmn precamberian crystalline basement in the Ethiopian Rift Valley.
- Dobrin, M.B.,and Savit, C.H., (1988):** Introduction to Geophysical prospecting. McGraw-Hill Inc. Singapore.
- Doser, D. I. and Keller, G. R. (1999):** Seismicity of the East African Rift and its relation to rift development. Acta Vol. II(1)- 1999 43-51
- Duprat, A. (1987):** Geophysics in Geothermal Prospecting . Applied Geothermics. John Wiley & Sons.Ltd.
- Ebinger ,C.J., Yemane. T., WoldeGabriel , G., Aronson, J.L., & Walter, R.C (1993):** Late Eocene-Recent Volcanism and faulting in the southern main Ethiopian rift. J. Geol. Soc., London, 150, 99-108.
- Electroconsult, (1986):** Exploitation of Langano-Alutu geothermal resources. Feasibility report No. Electroconsult. Milano, Italy. Ethiopia. Journal of African Earth Sciences, vol.8, No.1,pp.99-105.
- GEOSOFT Mapping system , 1994.** Toronto. Canada.
- Gianelli , G., & Teklemariam, M., (1993):** Wate-rock interaction processes in the Altu-Langano geothermal field (Ethiopia ). Journal of Volcanology and Geothermal Research, 56, 429-445.
- Gouin, P., (1979):** Earthquake history of the Ethiopia and the Horn of Africa. Ottawa,

Ont. , IDRC ,1979, 259 pp.

**Grant, F.S., and West, G.F., (1965):** Interpretation theory in Applied Geophysics. New York: Mc Graw-Hill.

**Gupta, V.K., Ramani, N., (1980):** Some aspects of Regional- Residual separation of gravity anomalies in a precambrian terrain Geophysics. Vol. 55, No. 9 P 1412-1426

**Hammer , S., 1939** Terrain corrections for gravimetric survey, Geophysics, Vol.4, No3, p184.

**Heiskanen, W.A. and Moritz, H., (1967):** Physical Geodesy, Freeman, San Francisco.

**Hochstein, M.D., Caldwell, G. and Kifle, K. 1983.** Minimum age of the Aluto Geothermal System. Internal Report , Geothermal Institute . University of Aukland.

**Jean-Jacques Tiercelin, Caroline Le Turdu & Francoise Gasse., (1997):** International Symposium "Flood Basalts, Rifting and Paleoclimates in the Ethiopian Rift and Afar Depression" Addis Ababa, Ethiopia February 3 to 14,1997

**Kazmin, V. and Berhe, S., (1978):** Geology and development of the Nazareth area. Ethiopian Institute of Geological Survey.

**Keller G. V., Frischknecht F. C., (1966):** Electrical Methods in Geophysical prospecting.

**Keller G. V., (1970):** Induction method in prospecting for hot water , Geothermics, Special issue, 2, 318-332.

**Koefoed, O., (1970):** A fast method of determining the layer distribution from the kernel function in geoelectrical sounding Geophy. Prospecting . 18: 564-570

**Koefoed, O., (1979):** Geosounding Principles., I Resistivity sounding measurements.

Methods in geochemistry and Geophysics. Elsevier, Amsterdam.

**Krohn , D.H., (1976):** Gravity terrain Correction using multiquadratic equation .  
Geophysics 41, 266-75.

**Lloyd, E.F., (1977):** Geologiucal factors influencing geothermal exploration in the  
Langano Region, Ethiopia Unpubl. MS., 73 pp.

**Lowrie , W., (1997):** Fundamentals of Geophysics., Cambridge University Press,  
Cambridge.

**Macleod, I. N., (1986):** 2-D Potential Field processing short course notes. Sept. @45-25,  
1986, Paterson, Grant and Wetson Ltd., Toronto, Canada.

**Meyer, F. D., (1974):** Filter techiques in gravity interpretaion: Adv. In Geophysics., V. 31.  
P. 606-617

**Mohr, P.A., (1960):** Report on a geological excursion through southern Ethiopia: Bull.  
Geophys. obs. Addis Ababa, no. 3, p. 9-20.

**Mohr, P.A., (1962a):** The Geology of Ethiopia . University Collage Press., Ethiopia.

**Mohr, P.A, (1983):** Volcanotectonic aspect of the Ethiopian rift evolution Bull. Centre  
Recheres Elf Aquititain Expl. Prod., 7, 175-189

**Mohr, P.A., (1971):** The Geology of Ethiopia. Addis Ababa, Ethiopia. Addis Ababa  
university Press.

**Mohr, P.A., (1971b):** Outline tectonics of Ethiopia. UNESCO. Tectonics of Africa. P.  
447-458.

**Mohr , P.A., Mitchell. J.G., & Raynolds, R.G.H., (1980):** Quaternary Volcanism and Faulting at O'a Caldera, Central Ethiopian Rift. Bull. Volcanol. , 43-1, 173-189.

**Mohr, P.A.,(1967):**Th Ethiopian Rift System: Geophy. Observatory of Addis Ababa Bul., 5, 33-62

**Mohr, P., (1983):** Ethiopian flood basalt province, Nature, 303, 577-583.

**Morelli,C., Ganta, C., Honkasalo, J., McConnell, R.H., Tanney, I.G.,Sgabo,B., Uotila, U. and Whalen C.T., (1971):** The International Standardization Gravity Net 1972, IAG, 39 terrue Gray Lussac, 75005, Paris.

**Morley, C. K. (1999):** Tectonic Evolution of the East African Rift System and its modifying influence of magmatism: A review. Acta vol. II(1) 1-19

**Mortiz, H., (1971):** Geodetic References System 1967. Pub. No.3, Bulletin Geodesique, Paris.

**Nettleton. L.L. (1976):** Gravity and Magnetics in Oil prospecting. New York. Mc Graw-Hill.

**Orellena, E. and Mooney. H. M., (1966):** Master Tables and Curves for Vertical electrical Sounding Over Layered structures. Intercleniia, Madrid, 34Pp.

**Parasinis,D.S., (1971):**Physical property guid for rocks and minerals ALMU. Mics. Chapman and Hall, London, England.

**Parasnis,D.S., (1989):** Principles of applied Geophysics. Chapman and Hall, London, England.

**Purcell, P.G., (19-). The Bouguer gravity map of Ethiopia.**

**Roger, S., Dautria, J.M., Coulon, C., Pik, R., Yirgu, G., Michard, A., Legros, P., Ayalew, D., (1999):** An Insight on the nature, composition and evolution of the lithospheric mantle beneath the north-western Ethiopian plateau: The ultrabasic Xenolith from the Tana Lake Province. *Acta Vulcanologica*. volII(I)-,161-168

**Searle, R., & Gouin, P. (1972).** A gravity survey of the central part of the Ethiopian Rift Valley. *Tectonophysics*, 15, 41- 52.

**Searle, R.C and Gouin, P., (1972):** A Gravity Survey of the Central Part of the Ethiopian Rift Valley. *Tectonophysics*. 15:41-52.

**Searle, R.C., (1970):** Evidence of Gravity Anomalies for the Thinning of the Lithosphere Beneath the Rift Valley in Kenya. *Geophys. Journal Roy. Astron. Society*. 21: 13-31.

**Slichter, L.B., (1933):** The interpretation of resistivity prospecting method for horizontal structure. *Physics*, 4: 307-322

**Smith, R.A. (1959):** some depth formula for local gravity and magnetic anomalies. *Geophysics. Prosp.* 7, 55-63.

**Spector, A., and Grant, F.S., (1970):** Statistical model for interpreting aeromagnetic data: *Geophysics*. V.35 Pp 293-302

**Street, F.A., (1979):** Late Quaternary lakes in the Ziway -Shala Basin , Southern Ethiopia . Ph. D, Cambridge.

**Swain, C.J., (1992):** The Kenya Rift axial gravity high: A re-interpretation. In “ The Afro-Arabian Rift System” Althair, R.( Ed.). *Tectonophysics*, 204, 59-70

**Tatsch, J.H., (1976):** Geothermal Deposits: Origin, Evolution and Present Characteristics. Tatsch Assoc., Sundbury, Massachusetts.

**Taylor J.R. (1982):** An Introduction to Error Analysis. Oxford University Press.

Colorado U.S.A.

**Teklemariam, M., (1996):** Water-Rock interaction Processes in the Ahuto- Langano Geothermal Field, Ethiopia. Ph.D. thesis, Department of Earth Science , University of Pisa.

**Telford, W.M., Sheriff, R.E., and Geldart, L.P., (1990):** Applied Geophysics, 2<sup>nd</sup> . Cambridge: Cambridge University Press.

**Tenalem Ayenew . (1998).** The Hydrogeological system of the lake district basin, Ethiopia. P.h.d. thesis, ITC, Enschede, The Netherlands. 259pp.

**Tesfaye K., Chorowicz,J., Collet,B., and Bonavia,F.F. (1997).** Volcanic vents rooted on extension fractures and their geodynamic implications in the Ethiopian Rift. J.Volcanolo.Geotherm.Res.79,205-222.

**Tsuboi, C., (1983):** Gravity. George allen and Unwin (publishers) Ltd. U.K.

**UNDP, (1973).** Investigation of Geothermal Resources for Power Development : Geology, Geochemistry and Hydrology of the Hot Springs of the East African Rift System Within Ethiopia .( Tech. Rpt. DP/SF/UN/116 No. 275 pp. ) UNDP, New York.

**Ward S. H., Fraser D. C., (1967):** Conduction of electricity in rocks. Min. Geophys., 1, 219. Geophysical reconnaissance at Kawereay, New Zealand. N. Z J. Geol. Geophys., 1, 219

**Wohletz, K., Heiken,G., (1992):** Volcanology and Geothermal Energy University of California Press. Oxford . England.

**WoldeGabriel , G., Aronson, J.L. & Walter, R.C., (1990):** Geology ,Geochronology, and rift basin development in the central sector of the Main Ethiopian Rift. Geological Society of American Bulletin , 102, 439- 458.

**WoldeGabriel , G., Walter , R.C., Aronson , J. L., Hart, W. K., (1992):** Geochronology and distribution of silicic volcanic rocks of Plio-Pleistocene age from the central sector of the Main Ethiopian Rift. *Quaternary International* , 13/14, 69-76.

**WoldeGabriel , G., Walter , R.C., Aronson , J. L., Hart, W. K., Mertzmann, S. A. (1999):** Temporal relations and geochemical features of felsic volcanism in the central sector of the MER. *Acta. II* 53-67

**Wyllie M. R. J., (1963):** The fundamentals of well log interpretation. Academic press.

**Woolard. G.P., (1979):**The new gravity system changes in international gravity base values and anomaly values *Geophy.* 44, 1352-66

**Yemane, T.G., WoldeGebriel, G., Tesfaye, S., Berhe, S.M., Durary,S., Ebinger,C., Kelley,S.,(1999):** Temporal and Geochemical characteristics of Tertiary volcanic rocks and tectonic history in the southern MER and the adjacent volcanic field. *Acta. Vul.* vol II(1) 99-119

**Zadro, M., (1984):** Spectral Properties of the Newtonian Potential field and their Application in the Interpretation of the Gravity Anomalies. *Geophy. J. R. astr. soc.* 79, 489-493.

**Zohdy A.A.R., Anderson, L.A and Muffler, L.J.P., (1973):** Resistivity, Self potential and induced polarization on Vapour dominated Geothermal systems. *Geophysics*, 38, 1130-1144.